Study of extreme ultraviolet laser ablation for fusion applications

Eduardo Solis Meza

Doctor of Philosophy

The University of York
Physics
May 2022

Abstract

Extreme ultraviolet (EUV) compact laser sources have become more available in university size laboratories. This type of laser offers unique characteristics in ablation of materials and interesting types of laser-plasma interactions that are not present in optical lasers interactions with matter. Recently these type of compact EUV laser sources have been widely used in the semiconductors industry due to their diffraction limits into a nanometre range which allow higher transistor densities in integrated circuits. This thesis discusses different aspects of EUV light. A capillary discharge EUV source with a Ne-like argon gain medium contained in an aluminium oxide capillary tube was used for different experiments. The comparison of the ablation process with EUV and optical light was discussed. Aspects such as the ablation topography and the ablation profile depth as a function of fluence were studied using materials with different ablation lengths, such as: gold, aluminium, silicon and copper. The applications in novel analysis methods using these short wavelength sources have become relevant as the size of these have been reduced considerably. The use of an EUV laser source in a time-of-flight mass (TOF MS) spectrometer as ionisation sources is also studied and discussed. This EUV TOF MS device developed in The Colorado State University was used to ablate different materials and measure the ionisation states achieved with this laser source. A plasma expansion model was proposed to understand the plasma expansion of the plume created after the ablation and to calculate the temperatures reached in the materials after the laser interaction. Simulations of the absorption and refraction processes during the interaction of a laser beam with a plasma are presented to consider the possibility of the development of diagnostics tools for high density plasmas which require lasers with frequencies above the plasma cutoff frequency. A discussion of the advantages and disadvantages of EUV laser sources in comparison to traditional optical laser widely used in diagnostics techniques is also presented in this work.

Contents

List of Tables

List of Figures

Acknowledgments

I consider myself a man of few words. This journey in my life has been exhausting, but I enjoyed it a lot. Of course, a lot of relevant events in the world have changed it as we knew it. Heraclitus, is quoted as saying "change is the only constant in life" and this has been true for me since I moved to the UK. The order of appearance in the following paragraphs is not related with the level of gratitude I have for all of you.

I would like to start with my supervisor Erik Wagenaars. He is one of the pillars in this thesis. *¡Gracias totales!* (Thank you so much!) for your support, patience and time. Without all your help this would not been possible.

Thank you to everyone in the YPI. Special thanks to Professor Greg Tallents, for sharing his valuable knowledge. Also to Dr. Kari Niemi and Richard Armitage for all their support in the laboratory. Also, thank you to all the staff in the YPI, your patience and kindness will be always in a special place. To all my friends in the YPI, I will not mention all of you, but if you are reading this, be sure that you are included in these acknowledgments. My sincere gratitude to Dr. Sarah A. Wilson, you are also one of the pillars in this thesis, all your help in the lab was invaluable.

Massive thank you to everyone at Colorado State University. Especially to Lydia Rush and Professor Carmen Menoni. You made my stay very enjoyable.

I need to thank all my friends from Mexico at York. Your presence in all our parties, pub crawls or meetings made my stay in York, even more pleasant. An important mention to the best housemates in the world: Victor, Mauricio and Cynthia. You were and still are new members of my core family.

Thank you to Ixchel. From my heart, thank you for all your love and support. You are the main source of happiness in my life.

Finally, Dad, Mum and the best Sister in the world. Thanks to my dad for all his support through this long journey. Life is always a mystery, even if mum is not physically here, all your teachings and unending love are present everyday of my life. To my big sister, an infinite thank you, without all your patience and love I would never become a scientist. I will always remember those days when you helped me to understand fractions, even if you had a rough day at work.

I express my gratitude to the Mexican National Council for Science and Technology (CONACYT) and the Mexican Secretariat of Energy (SENER) for financing this work

through the *CONACYT-SECRETARÍA DE ENERGÍA-SUSTENTABILIDAD ENERGÉTICA 2017 SÉPTIMO PERIODO* scholarship.

This is probably my last assignment as student. Thank you everyone!

Declaration

This thesis has not previously been accepted for any degree and is not being concurrently submitted in candidature for any degree other than Doctor of Philosophy of the University of York. This thesis is the result of my own investigations, except where otherwise stated. All other sources are acknowledged by explicit references.

Within this work some ablation experiments were performed by Dr. Sarah A. Wilson and were presented in her PhD thesis, part of her results were included in this thesis to compare the ablation effects at different laser wavelengths with input during measurements and further analysis being performed by myself.

In addition, Chapter 5, presents work, performed of my own merit, alongside work from Lydia Rush, Dr. Carmen Menoni of the Colorado State University, Dr. Erik Wagenaars and Prof. Greg Tallents of The University of York. This collaborative work has been accepted for publication within the SPIE Conference Proceedings. Where results taken from my input on said publication are presented within this work.

To my beloved mother

"There are no goodbyes, wherever you are, you will always be in my heart." – Mahatma Gandhi

Chapter 1

Introduction

1.1 Motivation

Extreme ultraviolet (EUV) radiation corresponds to wavelengths from 5 nm to 50 nm. This kind of radiation is useful to a broad range of applications. For instance, for probing of high density plasmas and producing modern computer chip. In addition, EUV sources have been developed to the point where is possible to have sources in a university scale laboratory. This allows the development of plasma probing techniques such as interferometry or shadowgraphy with EUV backlight sources.

EUV radiation is nowadays one of the most important light sources in modern electronic technologies. This kind of radiation has developed the industry of integrated circuits to the point where is possible to achieve a density up to 291 million transistors/mm^2 [7]. EUV lithography has become the state-of-the-art technology in the fabrication of a huge variety of components in modern electronic devices. Nevertheless, there is still an important research interest in the fundamental interactions of EUV radiation with different materials. Depending on the material properties, the ablation process can differ substantially for conductors, insulators and semiconductors. For this reason, access to small scale EUV laser sources is fundamental to the development of research in laser-plasma experiments at these wavelengths. Dominant processes during laser ablation with EUV radiation differ considerably in comparison to visible radiation, with EUV light direct photoionisation is the dominant process during ablation and the effect on different type of materials is still an active research field.

Another interesting field is the applications of EUV sources for multidisciplinary science. Due to the short wavelength it is possible to achieve tight ablation spots, this enables the analysis of biological samples below the micro-scale in analytical techniques such as mass spectrometry where an ionisation source is required in the analysis process. The small ablation spot size and the ionisation capabilities of this type of radiation look promising in this area and other such as chemistry, geological and forensic sciences.

Of specific interest in this work will be the understanding of the interaction of EUV

radiation with matter. Firstly, the comparison of the interaction of visible and EUV radiation during ablation of solid materials with the same laser fluence. This will help to understand the most important differences after the laser interaction and how the surface topography is affected at different wavelengths.Secondly, the understanding of plasma expansion is also a relevant topic to understand the plasma plume behaviour after the laser interaction. Plasma expansion was studied both experimentally, results from a mass spectrometer, and through modelling. Again, the focus was on comparing behaviour of plume created with EUV and visible lasers.

1.2 Thesis summary

This thesis is composed of the following chapters:

Chapter 2 introduces the basic concepts for extreme ultraviolet radiation and the production mechanism for the laser source of interest. This chapter includes the necessary underlying physics to understand the ablation processes studied, the plasma expansion models used, the equilibrium processes for the required calculations and the basic mechanism of plasma-radiation interactions.

Chapter 3 gives an appropriate introduction to all the analysis methods to understand the experiments in this thesis. From the experimental set-ups used for the experiments and their analysis to the conceptual tools for the simulation required.

Chapter 4 presents the experiments performed to compare how EUV radiation differs from visible radiation during the process of ablation of different materials. It also includes the analysis of the ablated samples and a discussion of the ablation mechanisms and how they differ at different wavelengths.

Chapter 5 presents the results of time-of-flight mass spectrometry with an EUV laser as ionisation source. In this chapter is discussed the possibility to use this device as a diagnostic technique to measure the temperature of the plasma plume created after the laser interaction. Different models are included to understand the plasma expansion after the laser interaction and try to simulate the number of measured ions with these models.

Chapter 6 gives the results of the interaction process of simulated plasma plumes and their interaction with visible and EUV radiation trying to simulate the process of probing a plasma using electromagnetic radiation.

Chapter 7 summarises all the work presented and concludes with the most important results from each chapter.

Chapter 2

Scientific Background

Nuclear fusion is promising to contribute to a long-term solution to the world's fossil fuel shortage. There are two important approaches to reach sustainable nuclear fusion, magnetic confinement fusion (MCF) [8] and inertial confinement fusion (ICF) [9]. MCF is the oldest approach for a fusion power source; it has been researched since the early 1940's. A simplified description of MCF is the confinement of hot dense plasma within a vessel, using powerful magnetic fields. This plasma is made of different hydrogen isotopes, the temperature condition inside the vessel forces them to fuse and release energy. Different devices have been developed to achieve this objective, so far Tokamaks are the flagships of this approach [10]. Alternatively, ICF uses powerful lasers to compress a fuel pellet made of deuterium and Tritium (DT capsule), trying to fuse D and T together, releasing energy. There is a huge amount of underlying research in this area, with one of the identified issues ICF pellets that often fail to implode pellets, because of Rayleigh-Taylor instabilities [11]. Deeper understanding of this type of instabilities is required to achieve ICF in a reliable way.

Since 2011, the National Ignition Facility at Lawrence Livermore National Facility and more recently the Laser Mégajoule facility in Bordeaux, France have been trying to understand the processes during ignition [12]. There are two ignition scheme: direct and indirect drive [13]. In direct drive, lasers symmetrically irradiate a spherical pellet made of DT. Through ablation of the outer shell an implosion via a series of shock waves is initiated. In this case, the efficiency of compression is dependent on the region where the laser energy is deposited on the ablation surface. The other scheme is called Indirect Drive, here the fuel pellet is in the middle of a cavity known as "hohlraum" (German for hollow space), and the cavity walls are irradiated by lasers to produce soft X-rays, which ablate the shell more uniformly to produce the implosion via a series of shocks. The laser interaction with the walls to produce these soft X-rays, and the interaction of them with the pellet are important research subjects, especially to understand the compression stage to initiate ignition.

One of the main issues in studying ICF-relevant plasmas is that these are high density, high temperature plasmas. This means that many (visible) laser diagnostics do not work because of the low penetrability solids and dense plasmas due to their long wavelengths.

The probe laser beam penetrates the plasma only to the point where the electron density reaches the critical density $n_c \approx 10^{21}\lambda^{-2}\,\mathrm{cm}^{-3}$, at which point reflection occurs [14]. It is clear that making the wavelength of the probing light shorter, enables the diagnosis of more dense plasmas. In particular wavelengths in the EUV and soft X-rays range would be suitable for this. Unfortunately, laser sources in this wavelength range are not readily available. One technique that is well established for probing dense plasmas is using a soft X-rays laser. Normally, such a laser is made using a technique known as free electron lasers (FEL) or via laser-produced plasma which consists of focusing a high power laser beam onto a high-Z foil, generating soft X-ray radiation in the plane of the foil. Both techniques require large facilities to produce the desired wavelengths, which means that access to these sources is limited. FLASH at DESY in Germany is an example of the required facilities to produce X-rays using a FEL source [15]. Producing intrinsic short wavelength lasers avoid the need for frequency multiplication, which is commonly used to achieve shorter laser wavelengths, by producing integer multiplies of the frequency of the laser light. This process is undesirable, because it reduces the output efficiency and it is limited in wavelength.

Development of tabletop EUV lasers can help to increase the understanding of ICF-relevant laser produced plasmas (LPP). Especially the evolution of plasma expansion in the interaction of the laser, and the target and later the laser and the plasma. From NIF experiments, it is clear that there are many different uncertainties. Especially during the implosion stage or in the laser-wall interaction, as well as the understanding of the energy transport processes, which are all important to achieve a better design for ICF targets.

Other interest in EUV lasers is for plasma interferometry. Plasmas close to solid density are opaque at visible wavelength commonly used in conventional lasers. EUV laser sources open the possibility to extended laser interferometry to large-scale plasmas of near solid density plasmas.

Since 1999, compact EUV laser sources have been developed at Colorado State University, This research has enabled the construction of this type of laser within a tabletop size [16], making them the most compact way of generating EUV light. This opens the possibility of portable soft X-rays tools that will allow a detailed electron density mapping and its temporal evolution in a variety of dense plasmas. This setup uses an Ar plasma medium with electron-electron collisions acting as the pumping mechanism for lasing. Lasing of the plasma medium is achieved with a capillary discharge tube: this process will be explained in detail later.

2.1 Extreme Ultraviolet Light

Since the early days of laser development back in the 1960s extension of lasing into the X-ray regime was desired, but this represented an extraordinary challenge in several aspects. Some of the difficulties related with X-ray laser are an unfavourable gain scaling with wavelength, the inefficiency in cavity reflectors and the pumping power required. Visible and infrared

lasers operate in a Fabry – Perot style of reflection cavity. The lasing medium is pumped to a population inversion, amplification is provided by stimulated emission. A high degree of coherence and collimation is achieved with efficient cavities. However, near to the X-ray region the reflectivity of cavity mirrors is poor. Other techniques of coherent X-ray light attempt to overcome this problem. For instance, X-ray free electron laser sources, laser produced plasmas or capillary discharge lasers.

2.1.1 X-ray free electron lasers

Based on the premise of energy radiation from an accelerated charged particle, X-Ray free electrons lasers (XFEL) sources are a unique way to generate short wavelength X-rays with high pulse energies and short durations. This technique consists in the extraction of electromagnetic energy from the kinetic energy of a high-energy electron beam traveling along an array of periodic lattices of alternating magnetic dipole fields, known as an "undulator". These magnets force the electron beam to undulate transversely. This repetitive bending causes the electrons to emit electromagnetic radiation. The emitted radiation has a fundamental wavelength λ_l as described in equation 2.1, known as the simplified undulator equation. λ_u, defined in equation 2.2, is the undular period, γ is the Lorentz factor with E_0 the electron net mass energy. Equation 2.3 combines equations 2.1 and 2.2 and relates the energy of the electron beam to the X-ray wavelength. The first experiment to produce X-ray radiation with a undulator was in 1950s at Stanford but it generated incoherent radiation with a visible wavelength and a peak power of 10 W.

$$\lambda_l = \frac{\lambda_u}{2\gamma^2} \tag{2.1}$$

$$\gamma = E/E_0 \tag{2.2}$$

$$E = \sqrt{\frac{\lambda_u}{2\lambda_l}} E_0 \tag{2.3}$$

X-ray wavelength range starts from 0.01 to 10 nm. We can calculate the electron beam energy required to produced 1 nm X-rays. The electron rest mass energy is 0.511 MeV and assuming an undulation period of 10 cm,

$$E = 5000\sqrt{2}E_0 \approx 3.61GeV \tag{2.4}$$

This is the amount of energy required in the electron beam to produce X-rays. Even though these kinds of energies can be achieved, large-scale accelerators are needed. This example gives us a picture of the difficulties faced in the production of X-ray laser sources.

This free electron lasing process is based on the self-amplified spontaneous emission process (SASE). In this process a "narrow" electron beam passes through a sinusoidal varying

electric field or undulator. This narrow beam needs to accomplish specific characteristics to produce the SASE process, it needs to be high-energy, high-charge, short-pulse, low-energy-spread and low-emittance[17]. The underlying process of SASE consist in the generation of electromagnetic (EM) radiation by the beam of electron passing through the undulator producing the acceleration of them and by the interaction of the EM field produced and the electrons[18]. The EM radiation emits at the resonant wavelength λ_u,

$$\lambda_r = \Big(\frac{\lambda_u}{2\gamma^2}\Big)\Big(1 + K/2\Big) \tag{2.5}$$

where λ_u is the undulator period, γmc is the electron beam energy and K is the dimensionless undulator strength parameter $K = eB_0\lambda_u/2\pi mc$, an B_0 is the maximum on axis magnetic field strength of the undulator. A resonant effect occurs between the EM radiation and the electron beam such that there is a distance λ_r relative to the electrons after one undulator period. Thus, this interaction cab be sustained, and a net transfer of energy occurs from the electron beam and the radiation emitted. At a sufficient travelled distance by the electrons through the undulator, the EM radiation generated, and the electrons start to induce a periodic modulation of the beam along the longitudinal density of the beam at the radiation wavelength λ_r, this process is called microbunching. The microbunching leads to a higher radiation intensity and this also produce a stronger density modulation. The results is an exponential growth in the radiation intensity and the density modulation of the electron beam. During the phase of exponential growth of the radiation intensity the electrons lose Kinect energy due to the density modulation produce by the EM field. Then the phase of the electron motion relative to the radiation field change continuously until the phase is such that the electrons start to gain energy again from the EM field. This point is known as saturation and the increase in radiation intensity stops.

The first lasing and amplification FEL system was made in the early 1970s in a small-gain infrared FEL oscillator system at Stanford. In the late 1970s, the theorical description of what is known as the high-gain regime of FEL operation was developed. In the high-gain regime, the radiation power increases exponentially as the electron beam and radiation propagates along the undulator, in this scenario a small source could be amplified by many orders of magnitude before the process saturates. The FEL is a single-pass amplifier and can generate power peaks up to 10^{10} W. Modern XFEL sources are based on this type of interaction, electron beam sources and accelerators have advanced over the past decades as well, allowing better XFEL sources. Nowadays, there are several operational XFEL sources: the LCLS at SLAC in the US, FERMI at Elettra in Italy, PAL-XFEL in South Korea, SwissFEL in Switzerland and FLASH and the new European XFEL in Germany [19].

2.1.2 Ne-like argon lasers

Capillary discharge lasers are an alternative method of producing EUV radiation. Lasing in this scheme is produced by an eightfold ionised Argon (Ar^{8+}) plasma contained in a ceramic

capillary tube. This section is a brief discussion of the physics basis of this method and a review of the current development in this field especially in the tabletop size EUV laser developed in Colorado State University.

2.1.2.1 Soft X-ray amplification in plasmas

This section discusses the relation between the increase of intensity in an elongated plasma due to amplification of spontaneous emission along the axis. From this, the laser's gain coefficient can be determined. In addition, there are some useful expressions in this section for relating the gain coefficient to atomic processes. These relationships can be used to predict and scale the power output in lasers with further analysis and modelling.

The small-signal gain coefficient g is given by the product of the stimulated cross section σ and the population inversion density ΔN (see equations 2.6 and 2.7):

$$\Delta N = \left(N_2 - N_1 \frac{g_2}{g_1} \right) \tag{2.6}$$

Where N_1 is the population density of the lower quantum state associated with the photon energies and and N_2 is the population density of the appropriate upper quantum state. And g_1 and g_2 are the degeneracies of the lower and upper quantum states.

$$g = \sigma \Delta N \cong \frac{A_{21}\lambda^2}{8\pi\Delta\nu}\left(N_2 - N_1 \frac{g_2}{g_1} \right) \tag{2.7}$$

Where the Einstein coefficient A_{21} for spontaneous emission scales as λ^{-2}. Considering the case of naturally broadened transitions with $\Delta\nu \propto A_{21}$, this becomes,

$$g \propto \Delta N \lambda^2 \cong N_2 \lambda^2 \tag{2.8}$$

The pump power density P required to keep a certain upper laser level population density N_2 grows as,

$$P = N_2 A_{21} \frac{hc}{\lambda} \propto N_2 \lambda^{-3} \tag{2.9}$$

And the power density required to obtain a particular gain coefficient in a naturally broadened transition is,

$$P \propto g \lambda^{-5} \tag{2.10}$$

Equation 2.10 highlights one of the difficulties associated with developing short-wavelength lasers. In a laser medium, it is required to operate in a gain saturation regime in order to have an efficient energy extraction. In contrast to optical lasers, it is not possible to use an optical cavity in soft X-ray lasers, because the gain medium is too short lived. This type of lasers use a single pass amplification of spontaneous emission though the gain medium.

The Linford formula describes the intensity of the laser line, which increases as a function of plasma length, as follows [16],

$$I = \left(\frac{E}{g}\right)\left(e^{gl} - 1\right)^{3/2}\left(gle^{gl}\right)^{-1/2} \tag{2.11}$$

In this equation, g is the small-gain coefficient, l is the length of the gain medium and E is the constant proportional to the emissivity. First experiments with this discharge-based laser showed lasing in the $2p^5 3p^1S_0$ to $2p^5 3s^1P_1$ (J=0-1) line of Ne-like argon in a plasma column generated in a capillary discharge. These experiments were performed using 3 mm diameter capillaries and the gain in the plasma was determined by measuring the integrated line intensity as a function of plasma column length. Figure 2.1 shows this exponential increase in energy as function of length until a plasma column length of 15 cm where saturation is achieved.

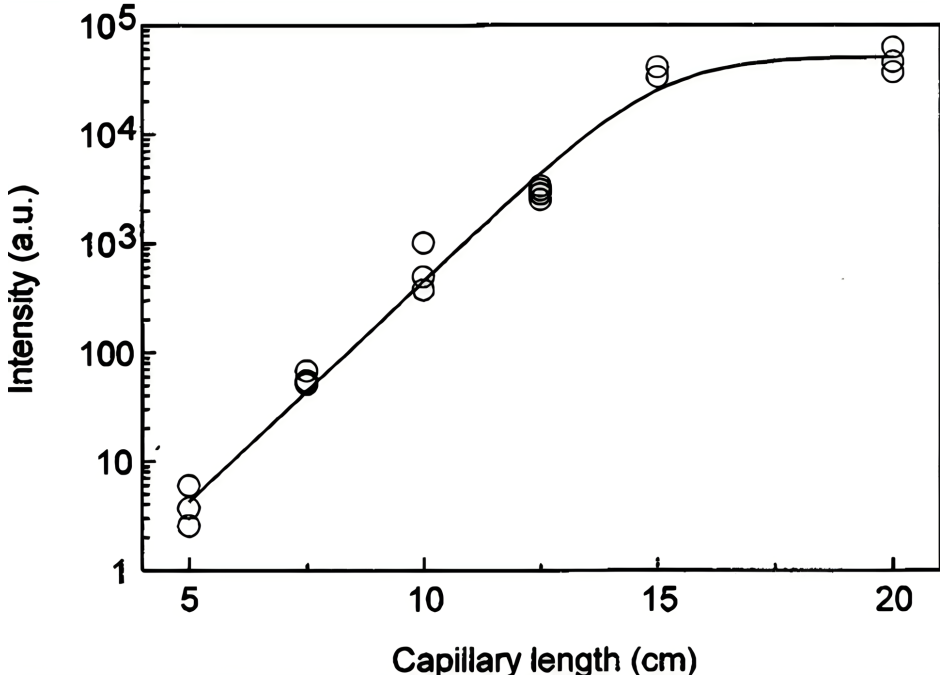

Figure 2.1: Laser output energies for varying plasma column length. Taken from Rocca et al. [1].

Other experiments made by J. Rocca et al. [16] showed that intensity of the same line increased for longer capillaries. Figure 2 shows that in a 3 cm long capillary this transition is overshadowed by surrounding lines like Mg-like Ar, Al-like Ar and 3d-3p Ne-like . In a 6 cm capillary, the intensity of these two lines increases significantly in comparison with the other lines mentioned before. A 12 cm capillary shows a clearly dominant J=0-1 transition line at 46.9 nm and all the surrounding lines become insignificant.

These experiments showed that in a single pass amplifier the gain coefficient depends on

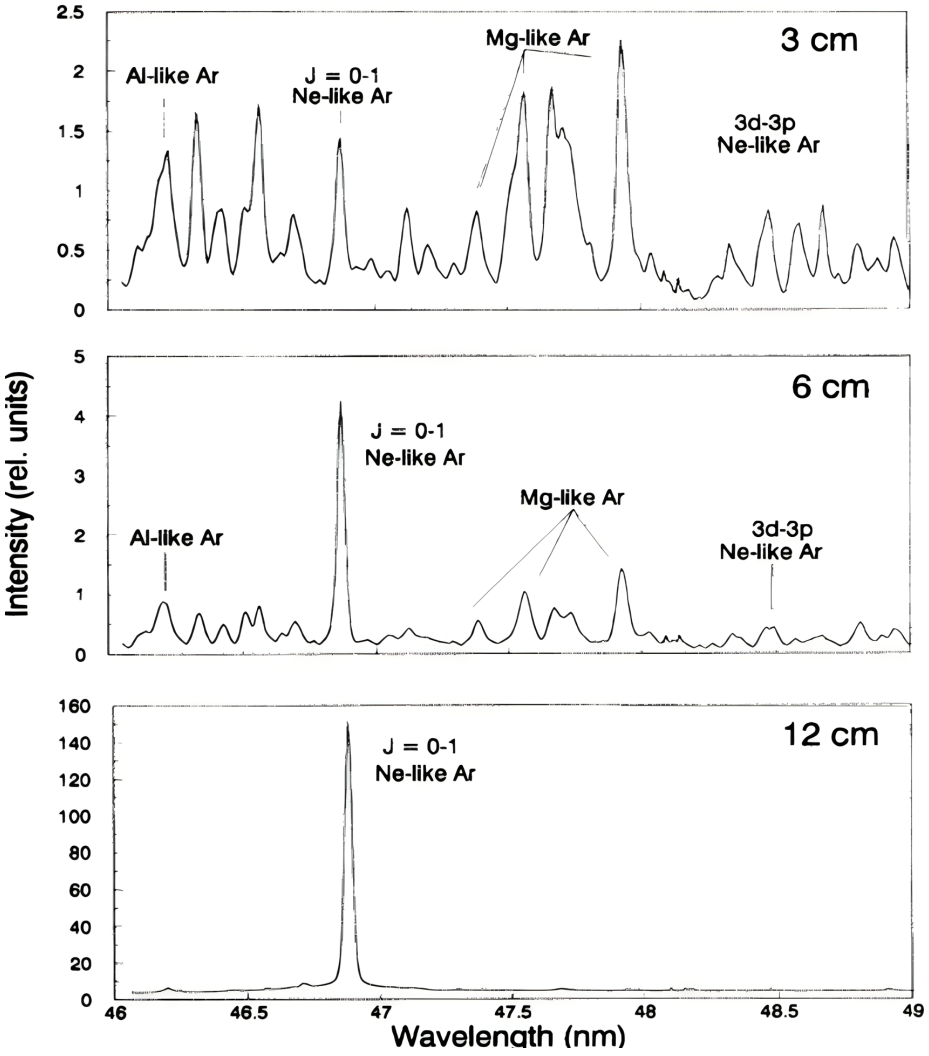

Figure 2.2: Spectra from Ar plasma columns length 3cm, 6cm and 12cm. Taken from Rocca et al. [1].

the length of the plasma, for Ne-like Ar gain saturation is typically reached when gl $\approx$ 14 – 20 which correspond to l $\approx$ 15 cm for a gain coefficient g $\approx$ 0.95 - 1.33 cm^{-1}. This length is few orders of magnitude larger than for typical optical gas laser cavities.

2.1.2.2 Capillary discharge lasers

One of the ways to make a Ne-like Ar gain medium is using a ceramic tube with few millimetres diameter filled with a gas at low pressure and ionised by a current pulse. This short time process ensures that the initial ionisation occur close to the capillary wall. The large magnetic field generated by the current then compresses the plasma through the $\mathbf{J} \times \mathbf{B}$ force to drive a strong shock towards the capillary axis. This heats and ionises the Ar plasma to reach the desired Ne-like Ar state.

The Ne-like sequence had been very successfully utilised in laser-produced plasmas to generate soft X-ray lasing in an electron-collisional excitation pumping scheme using elements with Z as low as titanium. Electron-collisional pumping or excitation is the easiest X-ray laser pumping concept to understand. This method is described by the following equation described by R. Elton [20],

$$\mathrm{X}_0^{\mathrm{i}+} + \mathrm{e} \longrightarrow \mathrm{X}_\mathrm{u}^{\mathrm{i}+} \tag{2.12}$$

Where X_0^{i+} is an i-times ionised atom of an element X in a ground state 0 to the pumped upper state u in the same atom. The lasing occurs when the excitation decays to an intermediate level l to finally replenish the initial state population.

Ar^{8+} is part of this Ne-like sequence and it is widely used in this lasing scheme. To achieve gain in argon, a plasma temperature of approximately 80 eV and densities between 10^{18} and 10^{19} cm^{-3} are required. Fast capillary discharge can generate a hot highly ionised plasma column with large optical length in order to achieve a significant amplification. The recombination scheme in addition requires rapid cooling of the plasma and also a small plasma diameter to avoid quenching of the population inversion by trapping of resonant radiation [21].

In a capillary discharge laser, the plasma column must be relatively stable and homogenous during the amplification stage. However, several effects might cause instabilities or inhomogeneity in the Z-pinch process [22]. For instance, the initial electrical breakdown through the argon column. The main high current may result in a channel-like breakdown along the capillary walls. A technique to overcome this instability is using a low intensity current (prepulse) to preionise the gas slowly. This prepulse current creates sufficient amount of ionisation in the gas, then the main current pulse can flow homogenously through the preionised gas.

Rocca et al.[23] [24] conducted some of the first experiments in capillary discharge lasers. Using a high-voltage fast pulse generator which produced a current pulse of 13 ns rise time and a full width at half maximum (FWHM) of 28 ns. This experiment helped to understand

the underlying physics of the whole process. The fast current pulse rapidly detaches the plasma column from the capillary walls and collapse of the plasma. The rapid expansion phase can be of interest for the population inversions by collisional recombination. The short-lived small diameter hot capillary plasma inside the capillary has characteristics that approach those necessary for amplification of low-Z ions of the Ne-like sequence, as mentioned before.

Capillary discharge laser is the main source of EUV radiation used in this thesis. A detailed description of the setup is described in chapter 4.

2.2 Laser ablation mechanisms

Laser-induced ablation involves different processes that cause the ejection of atoms, ions, molecules and even clusters from a material surface. In the early 1970s ruby and Nd:YAG lasers were the most common visible and near-infrared laser sources [25]. From these early works, it has been understood that the interaction of laser light with a material causes permanent changes to the material properties, achievable almost exclusively through this means. Laser irradiation has been shown to cause changes in the local chemistry, crystal structure and morphology of materials [26] [27] [28].

A general overview of laser radiation interacting with matter could be defined as the ensemble of processes resulting from the conversion of an initial electronic or vibrational excitation induced by radiation energy transfer into kinetic energy of atom species, producing the ejection of atoms, ions or molecules from a material surface. These processes are often categorised into two types of interactions, laser-induced **desorption** and **ablation** depending on the modification degree produced on the material. Laser-induced desorption is defined as particle ejection without any observable mesoscopic modification of surface composition or structure; as explained by Haglund [29], this includes a particle yield that is a linear function of the density of electrons; and without any significant gas dynamic effects in the stream of particles leaving the surface. In contrast, laser ablation is a process where the material is removed from the surface in rates of typically 1/10 were conductedayer per pulse [30], causing surface modification both structural and composition level; in this case the particle ejection yield is a supra-linear function of the density of excited electrons. Furthermore, this process creates an ablation plume, adding to the process the interaction of plasma-surface, gas dynamics and also laser-induced chemical reactions.

An effective parameter to quantify the energy density of the laser interaction is the fluence of the laser. This describes the energy of the laser delivered per unit area, it is normally described in terms of joules per square centimetre,

$$Fluence = F = \frac{\text{Laser pulse energy } [J]}{\text{Effective focal spot area } [cm^2]} \tag{2.13}$$

The ablation threshold is the energy fluence required to evaporate in vacuum some part of

the irradiated target. Pulsed laser irradiation of solid targets has been an area of increasing interest since 1980 and the type of interactions and ablation mechanisms are closely related with the fluence threshold F_{thr}. Different models for ablation fluence threshold have different considerations for the wavelength range of the irradiated samples. Some models like the thermal model consider the energy required to reach this threshold is equal to the energy density contributions from the heating energy E_H, fusion energy E_F and evaporation energy E_S of the irradiated mass delimited by a laser spot size S,

$$F_{thr} = \frac{E_H + E_F + E_S}{S} = \frac{V\rho}{S}\frac{\left(C_s\Delta T + \lambda_f + \lambda_e\right)}{1-R} \tag{2.14}$$

where V is the ablated volume, ρ the material density, C_s is the specific heat, ΔT is the temperature difference, λ_f is the fusion latent heat, λ_e the evaporation latent heat and R is the material reflectivity. This thermal model as described only includes the contribution of the energy deposited by the pulsed laser and basically only takes into account the energy required to achieve the transition from solid material to gas. This model has been widely used when the laser wavelength is in the optical range and the energy fluence is relatively low.

Another interesting model to describe the ablation threshold fluence is the photochemical model. This establishes that the ablation mechanism is related with the absorbed photon density in the irradiated material. If this photon density exceeds the atomic density and if the photon energy is greater than the atomic binding energy then this is the minimum energy fluence required to reach the ablation threshold. In other words, the total amount of energy absorbed per volume should accomplish the following condition,

$$\frac{E}{V} = h\nu n_{phot} \geq h\nu n_{at} \tag{2.15}$$

where h is the Planck constant, ν is the photon frequency, n_{phot} and n_{at} are the photon and atomic density respectively.

Finally the ablation threshold in this model is,

$$F_{thr} = \left(\frac{E}{V}\right)_{min} = h\nu n_{at} \tag{2.16}$$

One of the main differences between visible and EUV laser radiation interaction with matter is in the energy of photons. The amount of energy carried by photons in the visible spectra are in the range of energy of valence band and thermal effects as mentioned. The energy in the EUV range is enough to ionise inner shells of the atoms. This deeper energy penetration triggers Auger processes, causing immediately impact ionisation. Finally, targets irradiated by EUV radiation are heated via direct photoionisation opposed to inverse bremsstrahlung using lasers in the optical range. These changes cause plasma plumes with lower temperature and higher density, this makes the modelling for the ablation threshold

at short wavelengths a new area for theoretical work. In this work, we present experimental results for these thresholds. Another important topic of interest is the ablation fluence threshold at different pulse lengths. According to Mikami *et al.* [31] the ablation mechanisms are substantially different in the EUV range depending in the duration of the laser pulses. The experiments performed at both wavelengths; EUV and optical are relatively long pulses with a few nanoseconds length. This might differ with previous work based on short and ultrashort duration laser pulses, especially in the EUV range.

2.2.1 Attenuation length

The development of compact and high repetition rate EUV lasers, offers a new approach to understand the matter-radiation interaction mechanisms and complements previous work done with EUV/SXR synchrotron radiation. These compact sources are able to produce nanosecond pulses of monochromatic radiation with energy of several tens of mJ, opening the access to a new regime. Optical lasers and their interactions with matter are deeply studied for several decades. For this reason, in this work, a series of experiments using a 532 nm laser were conducted as a direct comparison. Keeping parameters for the ablation process such as fluence and intensity the same, highlighting the main differences between both lasers.

2.2.2 Visible laser interaction with matter

One of the major advantages of laser as tools for material processing is the ability to precisely control where in the material and at what rate energy is deposited. Using the correct selection of laser parameters it is possible to achieve the desired material modification.

Light propagation in a material surface can be confined to a desired region by controlling the laser's spatial profile. Some of the methods for control include mirrors, telescopes or converging optics, amplitude homogenizers, refractive elements and diffractive optical elements [32]. More advanced optical devices for beam shaping such as spatial light modulators, deformable mirrors and tunable lenses allowing real time modification of the beam's intensity profile on the surface.

Laser ablation involves a series of complex processes, schematically represented in figure 2.3. First, the incident laser rapidly heats a significant volume of target material. This surface material will go through different phase transitions and will be affected by strong stress waves. A time after the interaction of the laser, material will start to boil off and expand into the gas phase [2]. Ejection of material starts on a picosecond timescale. The plume of ejected material will be irradiated with the last part of the incident laser unless the laser pulse is very short. The interaction of this radiation with the plume will heat the plume and attenuate the laser incident on the target. Eventually plasma formation and subsequent optical emission will result. Even after the laser pulse is finished the plume will continue to expand away from the target surface [2].

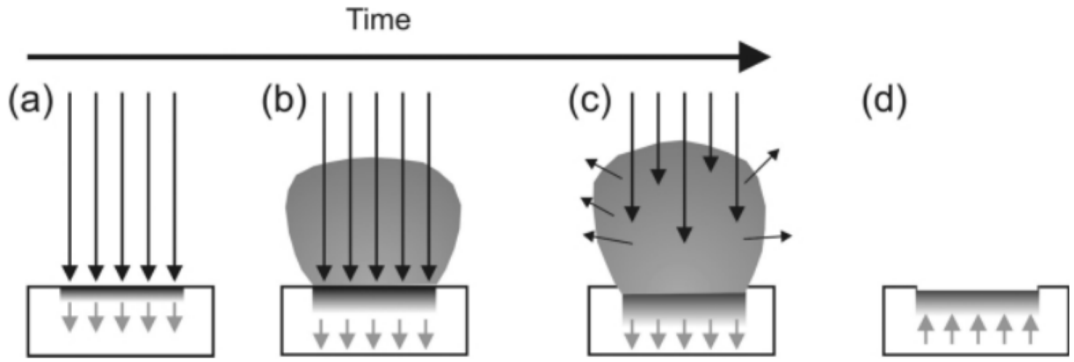

Figure 2.3: Schematic representation of the laser ablation process. (a) Initial laser irradiation perpendicular to the target surface, melting and evaporation begin. (b) Melt front starts to propagate into the solid target, vaporisation continues and laser-plume interactions become important. (c) Laser-plume interactions become the dominant process and also plasma formation. (d) Melted material re-solidificates. Taken from Ashfold et al. [2].

The light that goes inside the material decays in intensity with depth. A rate of decay inside a material is quantified by the absorption coefficient of the material, α. In general, α is function of wavelength and temperature. This decay in intensity I is described for a constant α as a function of depth z according to the Beer-Lambert law,

$$I(z) = I_0 e^{-\alpha z} \tag{2.17}$$

I_0 is the intensity just inside the surface after considering reflection loss.

The absorption depth was initially developed for a plane wave, however the energy absorption is approximately confined within the absorption depth still holds for more general waves. In the particular case of spherical and cylindrical waves, at distances far from their source, they can still be consider as plane wave fronts and Lambert law is valid. Wavelengths with short absorption depth allow local modification of surface properties without altering the bulk material. One important parameter in laser ablation is the optical penetration or absorption depth, $\sigma = 1/\alpha$, which is the depth at which the intensity of the transmitted light drops to 1/e of its initial value at the interface.

Some of the mechanisms involved in the laser-target interaction are sputtering processes and include thermal, electronic and macroscopic sputtering. This will mainly depend on the target material, the laser wavelength range and the pulse duration. Generally, photons will couple into electronic or vibrational states in the material depending on the incident photon energy. For instance, in insulators and semiconductors, the absorption process is mainly through resonant excitations. This results in transition of electrons from the valence band to the conduction band or within bands. In metals, absorption is widely dominated by the free electrons through inverse bremsstrahlung. The time required for the excited electronic states to transfer energy and reach thermal equilibrium depends on the specific material.

In metals, this time is in the range of 10^{-12} to 10^{-10} s. This means we explain the phase process transformation (thermal evaporation) in a classical way for nanosecond lasers [33].

The plasma frequency is an important parameter to relate the electron density of a plasma, n_e to its optical properties and it is described as follows,

$$w_p = \sqrt{\frac{n_e e^2}{m_e \epsilon_0}} \tag{2.18}$$

Reflectivity and absorbance for light frequencies below the plasma frequency are high because electrons screen the electric field of the light. However, above the plasma frequency, reflectivity and absorbance drop off drastically because of the electrons cannot respond fast enough to screen it. In other words, light with a frequency higher than the plasma frequency can pass through the plasma. For example a slab of Al has a density ρ of 2.70 g cm^{-3}, the density of electrons approximately $6 \times 10^{28}\,\text{cm}^{-3}$. This corresponds to an equivalent critical wavelength around 130 nm for this density. In the case of a 532 nm laser, one of the most widely used lasers, this means that the laser will be absorbed very efficiently. The critical density for this laser is about $4 \times 10^{33}\,\text{cm}^{-3}$. When the plasma plume is created, a gradient of density arises. Next to the surface there is a high density plasma close to solid density and this density decreases to a typical plasma density of around $10^{24}\,\text{m}^{-3}$. The laser will not be able to reach the solid surface anymore, most of the light will be absorbed by the plasma at critical density. This means that a significant part of the laser pulse does not reach the target surface, but is entirely absorbed in the plasma plume.

Most of the commercial lasers in the visible wavelength range produce Gaussian beams of circular section. A important parameter for laser ablation is the laser beam radius at the focal waist given by $w_0 = (2\lambda/\pi)f^{\#}$, the f-number, $f^{\#}$. Thus, in practice, the achievable focal radius, $w_0 \sim \lambda$. The divergence of the beam is directly proportional to the wavelength as well as, $\theta = \lambda/\pi w_0$. This means that for EUV lasers a smaller spot size and smaller beam divergence can be achieved than with visible lasers.

In laser ablation, there are key parameters, which are laser wavelength dependant. These parameters are important in the characterization of materials, especially for technological applications. For instance, the ablation threshold, the ablation rate and transition from the thermal ablation to the phase explosion have a strong dependence with wavelength. As showed by Koren [34] et al. short wavelength lasers are required for higher quality technological processes such as film deposition. Currently, ablation using visible lasers is still a focus of interest. For instance, the study of ablation of graphite with lasers at different wavelengths. One of the most interesting work was done by Hoffman et al. [35] using a Nd:YAG laser at different wavelengths to understand the formation of a variety of carbon allotropes such as diamond-like carbon films, fullerene, carbon nanotubes and graphene. As well, the study of the transition from thermal ablation to the phase explosion in carbon and the demonstration that the absorption coefficient of carbon decreases for longer wavelengths.

2.2.3 Soft X-ray interaction with matter

The laser-plasma interaction for a soft X-ray laser (SXR) is fundamentally different from optical lasers. As explained before there is a direct relation between all the ablation parameters and the irradiated light wavelength. In the SXR ray region, the critical density is typically greater than solid and the laser photon energy E_p becomes sufficient to directly photoionise elemental components unlike traditional lasers. The most important quality in this kind of lasers is that when the critical density is higher than solid, the laser still penetrates the expanding plasma plume. The continuous radiation on the material surface continues through out the duration of the laser pulse. Over this wavelength range, also a tighter focus is possible thanks to the reduction in diffraction limit. The tighter focus is a potentially desirable property for a number of applications, such as mesoscale machining, mass spectrometry and the coating of refractory material onto substrates. All these features make EUV and X-ray laser sources very attractive in the development of industrial applications.

Laser science development over years led to improvements in industry, material science, medicine and electronics. Especially, in micro- and nano- machining techniques encouraged by a progress in microelectronics and a continuous upgrade in lithography for computer processors and integrated circuits (IC). Miniaturisation of these components required an improvement and the shortening of the laser wavelength used for the lithography process, in order to increase the density of transistors in silicon wafers that make up processors and ICs.

In 2005, Juha et al. showed one of the first works on ablation using a coherent tabletop size EUV sources. At the end of this work, it is reported that in contrast with long wavelength lasers, the energy of a single photon is sufficient to make a significant damage in polymers. Also, it is concluded that ablation in polymers for this type of lasers does not follow the long-wavelength laser model for ablation rate $d = 1/\alpha ln(\phi/\phi_{th})$ and a new model describing the ablation rate of polymer ablation by EUV lasers is presented. In addition, this work confirms experimentally the improved quality of the ablated hole when the wavelength is reduced from the UV range to SXR. There is also no observable thermal damage at the shortest wavelengths. This is caused by a strong localisation of the absorbed energy.

Experimental and computational works on ablation using EUV laser have given important results [36], demonstrating that 85 % of the ablation process in parylene-N occurs at the first half of the 1.2 ns laser used for their experiments and lateral heat transport increases at later time increasing the surface feature size further. In 2016, Aslanyan et al. [37] performed a similar work demonstrating the reliability of ablation of thin targets using a SXR laser.

Besides the applications mentioned, these light sources can also be used to understand fundamental process directly related with ICF. An extensive benchmarking of the electron transport models is necessary for the design of ICF targets. Soft X-ray lasers have been utilised to measure the transmission through sample targets with an iron layer buried in plastic to understand the heat penetration into the target and measure the heat flow into

the target [38]. Some features such as brightness and monochromaticity make these lasers ideal for laser plasma experiments, especially, the underpinning processes of the Rayleigh-Taylor instabilities.

Despite of all work done about laser-matter interaction in different materials, there is still a need to develop a deeper understanding of shorter wavelength lasers and their interaction with matter. For example, the development and characterization of better and more compact sub-UV wavelength laser sources. There is also a need for further work in the improvement in measurements of laser transmission in gas targets for different thickness and the characterization of nozzle geometries for these type of targets. Nowadays, EUV lithography has became the standard process in IC and processor technology. Laser-produced plasmas (LPP) are the most popular approach as sources for EUV radiation production, while discharge-produced plasmas (DPP) are still developed to achieve a reliable and high repetition rate EUV source in some laboratories around the world. These LPP and DPP still require to be optimised to fulfil the the requirements for a high-volume manufacturing (HVM) process such as, source performance, debris mitigation, and optical components efficiency for collection and guiding of this radiation [39]. In 2012, Moors *et al.* [40] wrote an extensive review of the EUV radiation sources requirements for HVM manufacturing of IC and microprocessors. According to this analysis, to achieve this, it is required to expose about 100 silicon wafers per hour with an energy density per shot around 15 to 20 mJcm^{-2}, i.e. requiring an average power of 200 W. Recently, different companies such as ASML and Gigaphoton have developed machines able to produced 250 W sources at 13.5 nm based on LPP of Sn targets ablated with CO_2 lasers [41].

2.2.4 Nonlinear X-Ray optics

At high radiation intensities for X-ray lasers, nonlinear laser-matter interactions can become important. It is possible for light to interact with light via a medium through nonlinear interactions i.e. photons can interact with other photons and change their energy and momentum. This nonlinearity is different from the optical regime where conventional nonlinearities occur. The photons' energy in the optical regime only have enough energy to interact with valence electrons, X-ray radiation have enough energy to interact with valence and core electrons. However, nonlinear interactions in the X-ray regime are still been investigated due to their extremely small cross sections. we have observed the mixing of optical light with X-rays, nonlinear Compton scattering in the X-ray range, X-ray second harmonic generation and two-photon X-ray absorption.

These nonlinear interactions have been reported mostly in high intensity laser sources above $\sim 1 \times 10^{15}\,\mathrm{W\,cm}$ [42] and ultra-fast X-ray laser sources in the attosecond [43]. Nonlinear optical absorption and changes in the refractive index seem the two main nonlinearity processes during short-wavelength laser and matter interaction.

Linear optical absorption is described in section 2.2.2 an describes the radiation absorp-

tion by a medium in terms of an optical absorption coefficient $\alpha(\lambda)$ that depends on the wavelength of the interacting laser radiation and it is described by Lambert-Beer absorption law 2.17,

$$I(z) = I_0 e^{-\alpha z} \tag{2.19}$$

The transmittance is given by,

$$\ln\left(\frac{I(z)}{I(0)}\right) = -\alpha z \tag{2.20}$$

Nonlinear absorption phenomena occur usually when a high intensity laser beam interacts with matter and the variation of intensity $I(z)$ with distance travelled in the medium is described by [44],

$$\ln\left(\frac{I(z)}{I(0)}\right) = -\alpha z - \beta z I \tag{2.21}$$

This new coefficient β is the nonlinear absorption coefficient and the magnitude of β in comparison to α will determine if the nonlinear absorption phenomena are considerably during the laser-matter interaction. In most materials this coefficient is insignificant at low laser intensities. Due to the limited access to X-ray and EUV laser sources, the effects of laser and material parameters on nonlinear contributions are still an active research field [45] [46].

2.3 Plasma expansion

In the previous section, some of the physics of laser-solid interaction and plasma formation and heating has been discussed. This section focuses on longer time scales, after the laser pulse has finished and the hot, dense plasma expands into its surroundings, e.g. a vacuum or background gas. In literature analytic models describing the plasma expansion as an adiabatic expansion of a hot gas into a vacuum have proven popular and remarkably accurate. The calculation or assumption of the density and temperature profiles of the plasma at the end of the laser pulse can vary, but have a considerable impact on the properties of the expanding plasma. The most popular ones are based on an isothermal plasma assumption [47] or an isoentropic plasma [48]. In the Singh [47] model, the temperature in the plasma is assumed to be uniform (isothermal assumption) 2.5, leading to a (half)-Gaussian profile for the density, while in the Anisimov model [48], the entropy in the initial plasma is assumed to be uniform (isoentropic assumption) and the temperature at the expanding plasma edge is set to zero. This leads to elliptical profiles for both temperature/pressure and density as shown in figure 2.4. These initial plasmas then undergo an adiabatic expansion with the models describing temperature and density profiles as function of time.

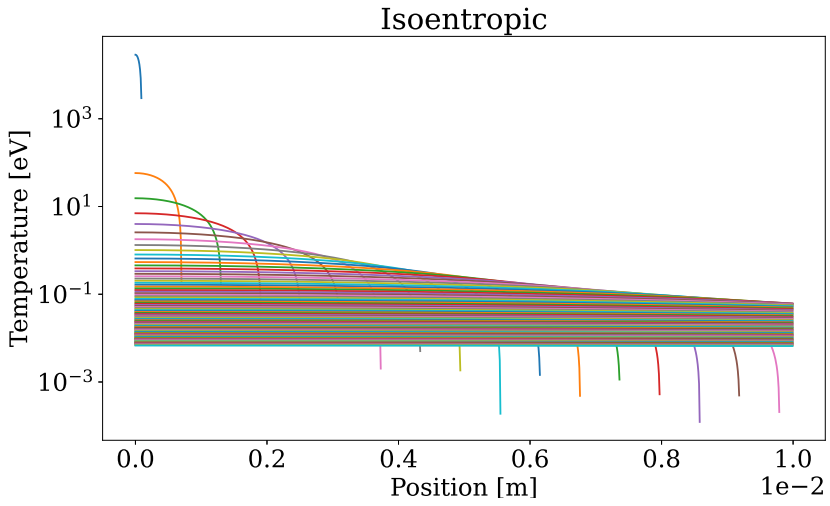

Figure 2.4: Example of the plasma temperature profile geometry isoentropic model.

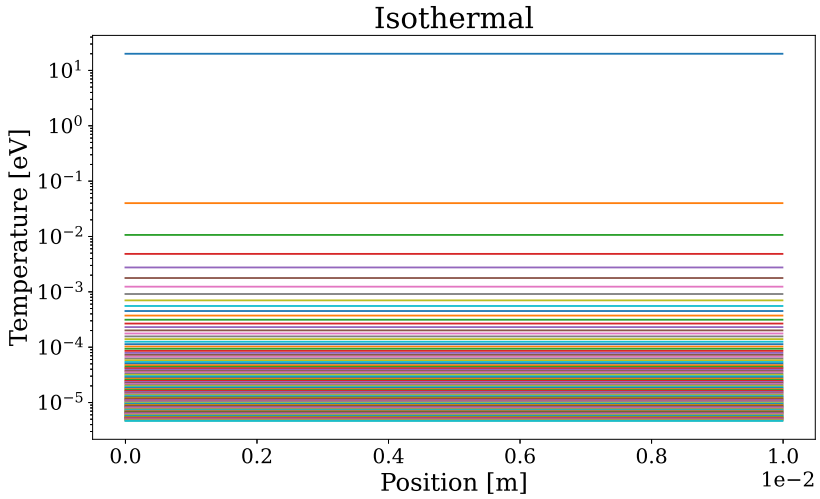

Figure 2.5: Example of the plasma temperature profile geometry isothermal model.

This adiabatic model studies the three-dimensional expansion in vacuum of a dense core laser-produced plasma. The expansion is described with a self-similar model, where the x-axis is normal to the target surface and the origin of coordinates is at the target surface. In a self-similar model, an element of fluid x_i remain fixed in proportion to the characteristic dimension X_i, independently of time as,

$$\frac{x_i}{X_i} = \zeta_i \tag{2.22}$$

The linear velocity for this self-similar model is expressed as,

$$v_i = \frac{\partial x_i}{\partial t}\Big|_{\zeta_i} = \zeta_i \frac{dX_i}{dt} \tag{2.23}$$

This self-similar model is widely using in gas dynamics due to its mathematical simplicity.

The evolution is described using gas dynamics equations for uniform deformed gas. At the end, the gas dynamic equation can be reduced to a set of equations of motion of a point, assuming that the temperature at the expanding plasma edge is zero and the initial entropy distribution is uniform over the cloud.

In Anisimov's model, they consider a laser beam of few nanosecond(∼10 ns) interacts with a target and evaporates the interacting surface, this creates a vapour cloud that expands into vacuum. It is assumed that the initial cloud/plasma formation time is much shorter than its expansion. This process can be described using the gas dynamics equations,

$$\frac{\partial n}{\partial t} + \nabla \cdot (n\vec{v}) = 0 \tag{2.24}$$

$$\frac{\partial \vec{v}}{\partial t} + (\vec{v}\nabla)\vec{v} + \frac{1}{n}\nabla p = 0 \tag{2.25}$$

$$\frac{\partial S}{\partial t} + (\vec{v}\nabla)S = 0 \tag{2.26}$$

where n, p, $\vec{v}$, and S are the density, pressure, velocity and entropy, respectively. Also the vapour is considered as an ideal gas with a constant adiabatic index $\gamma = c_p/c_v$.

Based on the self-similar model, the density and pressure profiles can be expressed at time t after the laser end of the laser interaction. These profiles can be expressed for the isothermal[47] and the isoentropic[48] assumptions.

As previously mentioned there is a model for the plasma expansion when the temperature of the plasma changes spatially. This model was developed by Singha and Narayan [47] and analyse the adiabatic expansion of a laser-produced plasma in vacuum after the laser pulse interaction. In this model, after the laser pulse no particle is evaporated nor injected into the inner edge plasma, i.e. the mass is constant after the laser pulse ablation. The equation for pressure and density have an elliptical profile and are described as follows,

$$n(x,y,z,t) = \frac{M_p}{I_1(\gamma)XYZ}\Big[1 - \frac{x^2}{X^2} - \frac{y^2}{Y^2} - \frac{z^2}{Z^2}\Big]^{1/\gamma-1} \tag{2.27}$$

$$p(x,y,z,t) = \frac{E_p}{I_2(\gamma)XYZ}\Big[\frac{X_0Y_0Z_0}{XYZ}\Big]^{\gamma-1}\Big[1 - \frac{x^2}{X^2} - \frac{y^2}{Y^2} - \frac{z^2}{Z^2}\Big]^{\gamma/\gamma-1} \tag{2.28}$$

M_p in equation 2.27 is the mass and E in equation 2.28 is the initial energy of the vapour cloud. $X(t) = X$, $Y(t) = Y$ and $Z(t) = Z$ represent the plume dimensions at time t and X_0, Y_0 and Z_0 are the plume dimension at $t = 0$

$$I_1 = \frac{\pi^{3/2}}{2}\frac{\Gamma(\alpha+1)}{\Gamma(\alpha+\frac{5}{2})} \tag{2.29}$$

$$I_2 = \frac{\pi^{3/2}}{2(\gamma-1)}\frac{\Gamma(\alpha+2)}{\Gamma(\alpha+\frac{7}{2})} \tag{2.30}$$

α is equal to $1/\gamma - 1$ and $\Gamma(x)$ is the Gamma-function.

For the case of an isothermal expansion described by Anisimov *et al.*[48], the density and pressure are Gaussian profiles, described as follows,

$$n(x,y,z,t) = \frac{M_p}{2^{\frac{1}{2}}\pi^{\frac{3}{2}}XYZ}\exp\Big[-\frac{x^2}{2X^2}-\frac{y^2}{2Y^2}-\frac{z^2}{2Z^2}\Big] \tag{2.31}$$

$$p(x,y,z,t) = \frac{M_p kT}{2^{\frac{1}{2}}\pi^{\frac{3}{2}}XYZ}\exp\Big[-\frac{x^2}{2X^2}-\frac{y^2}{2Y^2}-\frac{z^2}{2Z^2}\Big] \tag{2.32}$$

In both cases the vaporised material in the expanding plume can be described using the equation of ideal gases with an adiabatic index γ. Using the previous equations for the different profiles, it can be proved[48][47] that with the self-similar velocity profiles in the set of equations of gas dynamics 2.24, 2.25 and 2.26, gives the ordinary differential equations describing the adiabatic expansion of the plume as,

$$X\frac{d^2X}{dt^2} = Y\frac{d^2Y}{dt^2} = Z\frac{d^2Z}{dt^2} = \omega\frac{E}{M}\Big(\frac{X_0Y_0Z_0}{XYZ}\Big)^{\gamma-1} \tag{2.33}$$

where ω equals $(\gamma-1)$ or $(5\gamma-3)$for the isothermal or isoentropic model, respectively.

The feasibility of both models depends on several parameters that influence the plasma expansion dynamics such as the laser spot size, laser wavelength and laser fluence. In chapter 5 are presented experimental results to evaluate which of these models provides similar results to the experimental evidence.

Density profiles at a few different times for both models are presented in figures 2.6 and 2.7 for the isoentropic and isothermal models respectively. The profiles presented are time steps of the evolution of the plasma and they show the self similar principle. All these profiles have the same shape as they expand over time, they get bigger but keeping the same profile. Results clear from these figures that the density profiles have different shape for both models as they expand over time, but both models hold the self-similar principle.

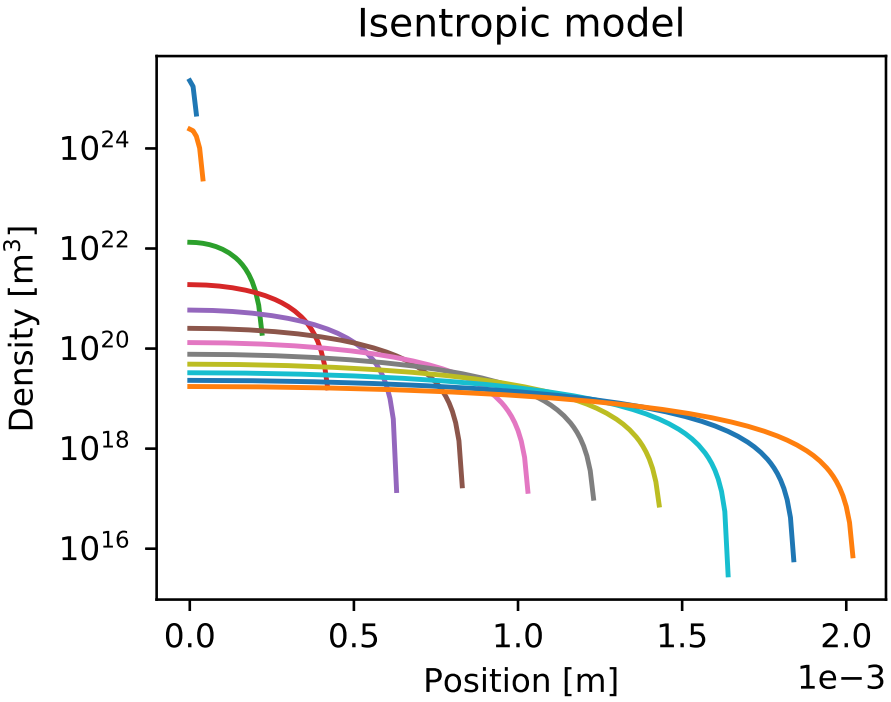

Figure 2.6: Example of the plasma density expansion in the isoentropic model.

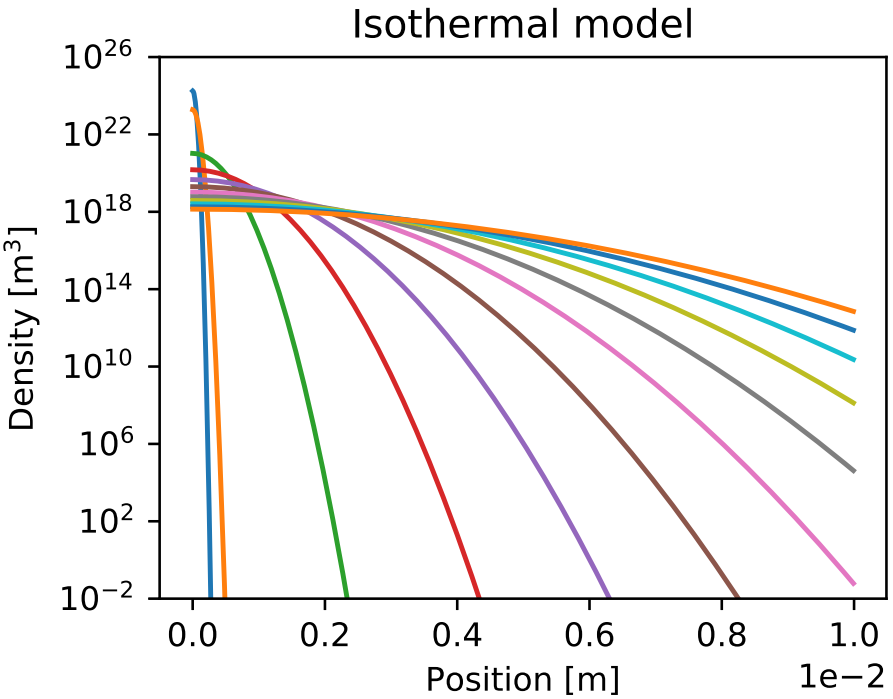

Figure 2.7: Example of the plasma density expansion in the isothermal model.

These adiabatic expansion models will be used in chapter 5 to analyse the plasma plume expansion of an EUV laser ablation in a mass spectrometery experiment.

2.4 Equilibrium processes

Plasmas can have a large variety of properties that characterise it. Some of these properties are the degree of ionisation, pressure and temperature. Depending on these properties, the plasmas can be modelled following different approaches and equations. In sections 2.4.1, 2.4.2 and 2.4.3 are explained the relevant models for the following chapters.

2.4.1 Coronal equilibrium

A gas in thermodynamic equilibrium can be described using Planck's formula for the distribution of photons, the velocity distribution of particles using a Maxwellian distribution, the energy levels of the particles follow Boltzmann's law and the ratio of the different ionisation species obey the Saha equation. In this type of gas, ions and atoms are excited and de-excited by particle collisions and photon interaction.

When a gas or plasma has a very low density, Saha equation is often not satisfied, and any excitation of the ground state will result in a photon escaping from the plasma. In this type of plasmas the main two interaction processes are collisional excitation by electrons the ground states and recombination through photons. These collisional excitations result in radiative cooling, and the plasma is assumed to be in a collisional ionisation equilibrium (CIE) or from its similarity to the solar corona it is named coronal equilibrium. It is assumed that the plasma in CIE is in a steady state, and that the collisional ionisation, charge exchange, radiative recombination, and dielectronic recombination are the only processes affecting the ionisation balance.

At low densities, every collisional ionisation is followed by radiative recombination and it can be expressed as described by Tallents [49] in equation 2.34. Where $n_{Z_{i+1}}$ and n_{Z_i} are the upper and lower ionisation stage respectively, K_{1C} is the collisional rate coefficient, A_{C1} is the rate coefficient for radiative recombination. m_0 is the electron mass, C_{ion} is a constant with value between 2.6 and $4.6{\times}10^{18}$ $\mathrm{m}^2(\mathrm{eV})^2$, g_{Z_i} is the degeneracy of the ground state of principal quantum number n of the Z_i charged ion and R_d us the Rydberg constant. This means that the ionisation rates depend exclusively of the plasma temperature and not on the plasma density.

$$\frac{n_{Z_{i+1}}}{n_{Z_i}} = \frac{K_{1C}}{A_{C1}} = \frac{\sqrt{3}}{2\pi} m_0 C_{ion} g z_i \Big(\frac{4\pi\epsilon_0}{e^2}\Big)^3 \frac{3c^3}{4} \frac{\hbar n^3}{2R_d Z_i^4} \Theta_c(T) \tag{2.34}$$

The temperature dependant part is expressed as

$$\Theta_C(T) = \frac{1}{\tilde{G}_{fb}} \frac{k_B T}{E_{ion}} \exp\Big(-\frac{E_{ion}}{k_T T}\Big) \tag{2.35}$$

with $\tilde{G}_{fb} \approx 1$ is the frequency averaged Gaunt factor and k_B the Boltzmann constant. This means that by measuring the densities of different ionisation stages, the plasma temperature can be determined. This is investigated further in chapter 5.

As mentioned, coronal model works when a plasma has a low electron density. For hygrogen-like ions, a condition to determine if the corona model is valid can be approximated if the following inequality is satisfied in terms of electron density and temperature,

$$n_e[cm^{-3}] \leq 5.6 \times 10^8 (z+1) T_e[eV]^{1/2} \exp\Big[\frac{1.162 \times 10^3 (z+1)^2}{T_e}\Big] \tag{2.36}$$

z is the ions charge.

2.4.2 Thermodynamic equilibrium

A plasma in thermodynamic equilibrium exists when the rate of every atomic process in the plasma occur in an exact balance rate of its inverse process. In this case of complete equilibrium, the physical state of the plasma can be completely described by a finite number of thermodynamic variables such as; density and temperature. In this kind of equilibrium the atomic level population distributions are determined using the Boltzmann statistics and the Saha ionisation distributions as a function of the temperature T of the plasma.

According to Boltzmann distribution a level population i in atoms of ionisation state z can be written as,

$$n_{iz} = \frac{N_z}{u_z(T)} g_{iz} \exp\big[-\frac{E_{iz}}{kT}\big] \tag{2.37}$$

N_z is the number of ions z, g_{iz} is the statistical weight which takes into account all the possible degenerate sublevels assigned in that level, E_{iz} is the excitation energy relative to the ground state energy and U_z is the partition function of ion z.

In the case of relative numbers of atoms of two adjacent ion states are determined by the Saha equation, as follows

$$n_{0z} = \frac{n_{0z+1} n_e}{2} \frac{g_{0z}}{g_0 z + 1} \Big[\frac{h^2}{2\pi m_e kT}\Big]^{3/2} \exp\Big[-\frac{E_{Iz}}{kT}\Big] \tag{2.38}$$

where this adjacent states are z and $z+1$ and E_{lz} is the ionisation potential of ion $z+1$ from ion z.

For a plasma in thermodynamic equilibrium, the radiation field is expected to be isotropic and homogeneous and the intensity at a temperature T of the radiation is given by the Planck function:

$$B_\nu(T) = \frac{2h\nu^3}{c^2} \frac{1}{\exp[h\nu/kT] - 1} \tag{2.39}$$

where ν is the radiation frequency, h is the Planck's constant and k is the Boltzmann's constant.

In a real experiment, the conditions to achieve a complete thermodynamic equilibrium in a laboratory plasma is very uncommon. In general, balanced collisional processes can be observed commonly but radiation processes are not balanced due to radiation process such as Bremsstrahlung, line radiation or Compton scattering

2.4.3 Local thermodynamic equilibrium

Plasmas in local thermodynamic equilibrium are similar to thermodynamic equilibrium plasmas, where the population distribution is determined by the law of statistical equilibrium but the radiation processes are not in equilibrium. The population distribution of LTE plasmas can be also be described by the Boltzmann and Saha equations and free electrons have a Maxwellian energy distribution as in the TE case.

The main difference between these models is the radiation field, it cannot be described as a Planck function and it depends on the population distributions and the atomic transition probabilities and not exclusively on the local plasma conditions.

This is a common type of plasma found in laboratory plasmas, where they have relatively high density, low temperature and collisional processes are far more important than radiative processes. These kind of radiative processes do not affect the population distributions. The collisional processes depend on local plasma conditions, while radiative processes are essentially non-local in the sense that they depend on population distributions at other spatial points.

A minimum electron density is required to validate the LTE state of a plasma between two levels in hydrogenic ions and can be roughly estimated as follows [49],

$$n_e[cm^{-3}] > 1.7 \times 10^{14} T_e[eV]^{1/2} \Delta E[eV]^3 \tag{2.40}$$

where n_e is the electron density, T_e is the electron temperature and ΔE is the energy gap between two quantum states in the electrons.

2.5 Refractive plasma diagnostics

Plasma properties can be measured using different techniques, depending on the information required [50]. The most common measured parameters are density and temperature of the species in the plasma of interest. There are different categories of plasma diagnostics, but in general they can be classified as either direct, e.g. using material probes inserted in the plasma, or indirect, often using electromagnetic waves to avoid perturbations of the plasma.

In many cases, the use of probe diagnostics is problematic because they interfere and interact with the plasma itself, making these kinds of diagnostics unsuitable for such plasmas. Often, alternative, non-perturbative methods using EM waves are used. For such techniques, a high accuracy and precision can be obtained and as long as the intensity of the EM wave is small enough, they cause a negligible perturbation of the plasma. These methods often

provide detailed information about the internal plasma properties and also good temporal resolution to have enough information to understand the plasma dynamics.

Some of the most common experimental techniques to measure the refractive properties of plasmas is shadowgraphy. The principles underlying this technique are basically the same in all the different variations of it. In the following sections are described the interactions of EM waves and plasmas and also the technical aspects of shadowgraphy.

2.5.1 Electromagnetic waves propagation in plasmas

Before describing the propagation of electromagnetic radiation in plasma, we need to describe the underlying principles of EM wave propagation in general media. Maxwell's equations are always the starting point in these kind of phenomena. Based on these equations, we can describe the radiation, scattering and refractive index changes during the interaction of EM waves and free or bound electrons, single atoms or more complex charge distributions.

Maxwell's equation written in MKS units are,

$$\nabla \cdot \mathbf{D} = \rho \tag{2.41}$$

$$\nabla \times \mathbf{E} = -\frac{\partial \mathbf{B}}{\partial t} \tag{2.42}$$

$$\nabla \cdot \mathbf{B} = 0 \tag{2.43}$$

$$\nabla \times \mathbf{H} = \frac{\partial \mathbf{D}}{\partial t} + \mathbf{J} \tag{2.44}$$

where $\mathbf{H}$, $\mathbf{D}$, $\mathbf{J}$ and ρ are the magnetic field vector, the electric displacement, the current density and the charge density respectively. In equation 2.42 and 2.43, $\mathbf{E}$ and $\mathbf{B}$ are the electric field and magnetic induction respectively. $\mathbf{D}$ and $\mathbf{B}$ are defined as,

$$\mathbf{D} = \epsilon_0 \mathbf{E} \tag{2.45}$$

$$\mathbf{B} = \mu_0 \mathbf{H} \tag{2.46}$$

ϵ_0 and μ_0 are the permitivity of free space and tge magnetic permeability respectively.

This description covers all type of electromagnetig phenomena from long wavelenghts to X-rays and beyond. The vector wave equation can by obtained applying the curl operator $(\nabla\times)$ to equation 2.42 and using the vector identity $\nabla \times \nabla \times \mathbf{A} = \nabla(\nabla \cdot \mathbf{A}) - \nabla^2 \mathbf{A}$ to obtain the following equation,

$$\nabla \times (\nabla \times \mathbf{E}) = \nabla \times \big(-\frac{\partial \mathbf{B}}{\partial t} \big) \tag{2.47}$$

substituting equation 2.42 in the parentheses gives,

$$\nabla(\nabla \cdot \mathbf{E}) - \nabla^2\mathbf{E} = -\mu_0 \frac{\partial}{\partial t}\big(\nabla \times \mathbf{H}\big) \tag{2.48}$$

Then equation 2.41 is substituted in the first parentheses,

$$\nabla(\frac{\rho}{\epsilon_0}) - \nabla^2\mathbf{E} = -\mu_0 \frac{\partial}{\partial t}\big(\nabla \times \mathbf{H}\big) \tag{2.49}$$

Equation 2.44 is subsitituted in the right side of the equation,

$$\nabla(\frac{\rho}{\epsilon_0}) - \nabla^2\mathbf{E} = -\mu_0 \frac{\partial}{\partial t}\big(\frac{\partial \mathbf{D}}{\partial t} + \mathbf{J}\big) \tag{2.50}$$

Equation is rearranged using 2.45,

$$\nabla(\frac{\rho}{\epsilon_0 n}) - \nabla^2\mathbf{E} = -\mu_0\epsilon_0 \frac{\partial}{\partial t}\big(\frac{\partial \mathbf{E}}{\partial t} + \frac{\mathbf{J}}{\epsilon_0}\big) \tag{2.51}$$

Finally we obtain the following equation,

$$\epsilon_0\mu_0 \frac{\partial^2\mathbf{E}}{\partial t^2} - \nabla^2\mathbf{E} = -\mu_0 \frac{\partial \mathbf{J}}{\partial t} - \frac{1}{\epsilon_0}\nabla\rho \tag{2.52}$$

Rearranging this equation, we can obtain the most common form of the vector wave equation

$$\left(\frac{\partial^2}{\partial t^2} - c^2\nabla^2\right)\mathbf{E}\Big(\mathbf{r}, t\Big) = -\frac{1}{\epsilon_0}\left[\frac{\partial \mathbf{J}(\mathbf{r}, t)}{\partial t} + c^2\nabla\rho(\mathbf{r}, t)\right] \tag{2.53}$$

where c is the phase velocity of the waves in vacuum and defined as,

$$c \equiv \frac{1}{\sqrt{\epsilon_0\mu_0}} \tag{2.54}$$

Equation 2.53 describes most of the interactions of matter and EM. For our shadowgraphy diagnostic, scattering, absorption and refraction are the most important interactions to take into account.

2.5.2 Shadowgraphy

Shadowgraphy is a simple non-invasive method to measure the lateral index of refraction in an object. In the shadowgraph method a beam of light travels through the object of interest and the transmitted beam samples the object and develops an intensity pattern. The spatial distribution of the intensity reveals the pattern of refractive index of the object. Shadowgraphy can be explained using geometrical optics, as rays deviate slightly in travelling through materials, bending towards regions of higher refractive index and away from regions of lower index. This means that the intensity profile of the beam changes as it traverses through the object under study[51]. There is also a focussing effect as light is bend towards

areas of high refractive index, as indicated in figure 2.8. The final intensity of the beam travelling can be recorded in a 2D image.

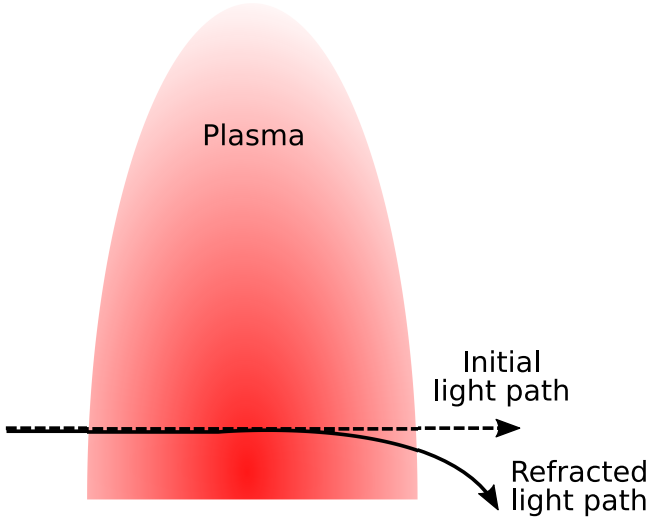

Figure 2.8: Light beam refracted after interacting with plasma

Geometrical optics can describe this phenomenon, where a collimated beam of intensity I_0 propagates in a medium parallel to the longitudinal direction t. A beam travelling through a medium with a density gradient will be deflected due to the change of the refractive index of the medium and it will result in a transverse intensity pattern I(r,s) in the detector plane at a distance L from the object of interest.

In the case of a plasma slab illuminated with an approximately plane parallel beam and a thickness smaller than the distance to the imaging lens, the total phase change difference ϕ along the beam path,

$$\phi = \int (\omega/c) n \; dl \tag{2.55}$$

Changes uniformly across the beam and the wavefront emerging from the plasma slab will have and angle θ to the incident front,

$$\theta = \frac{d\theta}{ds}\frac{\lambda}{2\pi} = \frac{d}{ds}\int n \; dl \tag{2.56}$$

Where λ is the wavelength, n is the refractive index at any point of the slab and dl is an infinitesimal line of the plasma slab. To illustrate this process, figure 2.9 shows the light bending represented by the red arrows travelling in a plasma slab and the emerging rays deviated an angle *theta* to the initial plane wave.

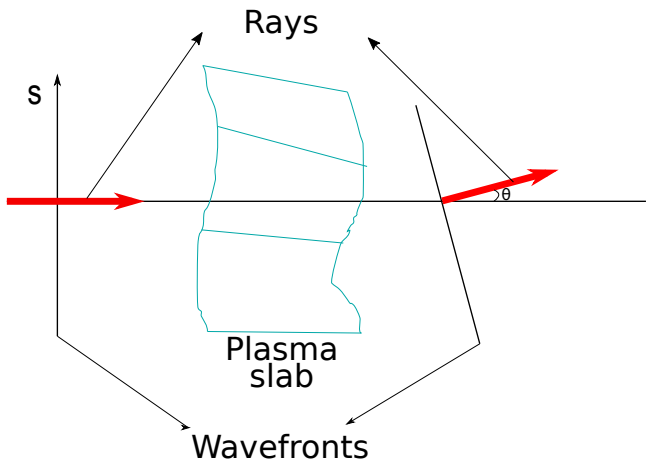

Figure 2.9: Schematic representation of a beam travelling through a plasma slab showing the final angular change of the beam.

The variation of the beam intensity occurs due to the angle variation *theta* in all the plasma. This produces an effective change in the electromagnetic energy that would be deposited in the same point s and it is moved to the point $s' = s + L\theta(s)$ with θ given by equation 2.56. The same phenomenon occurs in the orthogonal direction of propagation of the beam r. The final position of an incident ray at position (r, s) will be (r', s'),

$$(r', s') = \left(r' = r + L\frac{d}{dr}\int n\ dl, s' = s + L\frac{d}{ds}\int n\ dl\right) \tag{2.57}$$

The final intensity I_f of the beam after travelling through the plasma slab with an initial intensity I_0 will be given by,

$$I_f dr' ds' = I_0 dr ds \tag{2.58}$$

Assuming negligible diffraction effects, small deflections and a thin media (ΔZ) in comparison to the distance from the object to the detector $\Delta Z \ll L$, the variation of the optical path of the sample to the shadowgraph are related as follows [3],

$$\left(\frac{\partial^2}{\partial r^2} + \frac{\partial^2}{\partial s^2}\right)\int_0^{\Delta Z} n(r, s, t)\mathrm{d}Z = -\frac{1}{L}\frac{I(r, s) - I_0}{I_0} \tag{2.59}$$

$n(r, s, t)$ is the refractive index spatial distribution. Equation 2.59 is another form of the Poisson equation and relates the optical path of the beam with the normalised intensity variation of the shadowgram with respect to the initial intensity of the beam. In the case of a radially symmetric samples the refractive index distribution $n(r)$ which is proportional to the plasma density profile [3].

The main limiting factor in the accuracy of shadowgraphy is the diffraction effect in the free-space propagation. This issue can be reduced by either taking an appropriate distance

L from the object to the detector plane or using a shorter wavelength for the beam.

An schematic view of an experimental shadowgraphy array is present in figure 2.10. A typical set up uses a laser as a light source. The light traverses the plasma and is then detected by a detector, ideally a 2D detector to obtain spatial information. The laser beam is guided onto the plasma sample, filtered and focused before it is recorded in a CCD detector.

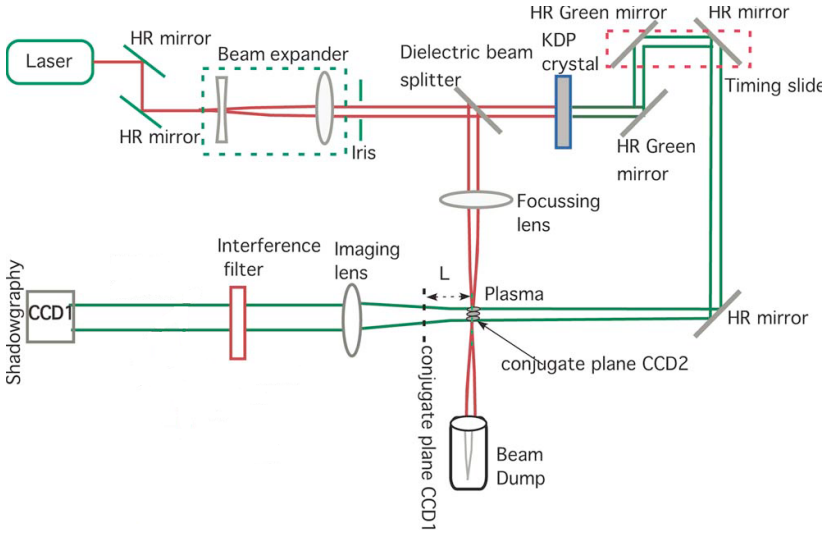

Figure 2.10: Schematic view of a typical shadowgraphy array. The laser beam is split into two beams, the red beam is used to create plasma and the other arm of the beam is used to backlight the plasma. Image modified from Gopal *et al.*[3]

A shadowgram of a chain of expanding plasma bubbles excited by a focused laser pulse in air is presented in figure 2.11, this type of figure can be analysed to extract further information about the plasma conditions such as the plasma density. In chapter 6 is presented an extended analysis of the type of interactions that occur between the plasma and the probing laser beam before the shadowgram is recorded in a detector.

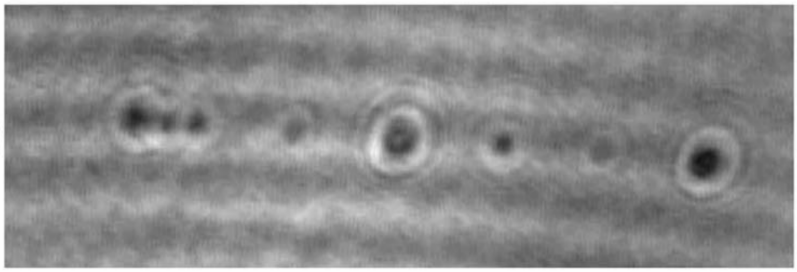

Figure 2.11: Shadowgram of a chain of expanding plasma bubbles excited by a focused laser pulse in air. Image modified from Gopal *et al.*[3]

2.6 Inverse Bremsstrahlung Absorption

During the interaction of laser-plasma interactions, there is an important process that occurs: inverse bremsstrahlung absorption. This is important mechanism for coupling laser energy to the plasma. As the name suggests, inverse bremsstrahlung (IB) is the inverse of bremsstrahlung radiation. Bremsstrahlung is the radiation that is produced when an electron is accelerated by an electric field. Inverse bremsstrahlung is the process by which an electron absorbs energy from an electromagnetic wave and accelerates. In an equilibrium radiation field, the rates of bremsstrahlung and IB are in detailed balance. An expression for the absorption coefficient for IB can be obtained using the power emitted by bremsstrahlung named as ϵ_{ff}. The expression for absorption coefficient K_{ff} due to inverse bremsstrahlung is obtained by,

$$K_{ff} < I_p(\omega) >= \epsilon_{ff}(\omega) \tag{2.60}$$

where $< I_p(\omega) > \mathrm{d}\omega$ is the black-body radiation instensity between frequency ω and $\omega + \mathrm{d}\omega$,

$$< I_p >= \frac{\hbar\omega^3}{\pi^2 c^2} \frac{1}{\exp\left(\frac{\hbar\omega}{k_B T})\right) - 1} \tag{2.61}$$

and $\epsilon_{ff}(\omega)$ is

$$\epsilon_{ff}(\omega) = \int_{(2\hbar/m_0)^{1/2}}^{\infty} \frac{dE(\omega)}{dt} f_\nu(\nu) d\nu \tag{2.62}$$

The total power emitted for a range of frequencies between ω and $\omega + d\omega$ per unit time, per unit volume is defined as,

$$\epsilon_{ff}(\omega)\mathrm{d}\omega = 16\sqrt{\pi}\Big(\frac{e^2}{4\pi\epsilon_0}\Big)^3 \frac{4}{3c^3}\frac{Z_i^2}{m_0^2} n_e n_{z_i} \Big(\frac{m_0}{2k_B T}\Big)^{1/2} I_{ff}\mathrm{d}\omega \tag{2.63}$$

where I_{ff} is,

$$I_{ff} = \int_{\sqrt{\hbar\omega/k_B T}}^{\infty} x \exp(-x^2) dx \tag{2.64}$$

This gives the following equation,

$$\epsilon_{ff}(\omega)\mathrm{d}\omega = 8\sqrt{\pi}\Big(\frac{e^2}{4\pi\epsilon_0}\Big)^3 \frac{4}{3c^3}\frac{Z_i^2}{m_0^2} n_e n_{z_i} \Big(\frac{m_0}{2k_B T}\Big)^{1/2} \exp\Big(-\frac{\hbar\omega}{k_B T}\Big)\mathrm{d}\omega \tag{2.65}$$

Finally the expression for the absorption coefficient is,

$$K_{ff} = 8\sqrt{\pi}\Big(\frac{e^2}{4\pi\epsilon_0}\Big)^3 \frac{4}{3c^3}\frac{Z_i^2}{m_0^2} n_e n_{z_i} \Big(\frac{m_0}{2k_B T}\Big)^{1/2} \frac{\pi^2 c^2}{\hbar\omega^3} \Big(1 - \exp\big(-\frac{\hbar\omega}{k_B T}\big)\Big) \tag{2.66}$$

Equation 2.66 shows that the absorption of radiation due to free-free inverse bremsstrahlung scales as $n_e n_{Z_i} \omega^{-3} T^{-1/2}$. It is important to consider the impact of IB when investigating the propagation of EM waves through a plasma. Depending on the conditions and the experimental details, IB absorption can be used as a direct plasma diagnostic or is an effect that needs to be taken into account when using diagnostics such as e.g. shadowgraphy as discussed further in section 2.5.2. Inverse bremsstrahlung is an important absorption process in laser-plasma interactions, but it is not the only one and it is only efficient if enough collisions take place. For laser with high intensities or high photons energy, IB becomes less and less effective. However, even for high-intensity lasers with high-energy photons, inverse bremsstrahlung is an important mechanism to provide energy to the plasma as showed by K. Lan **et al.** [52].

2.7 Critical density

During the interaction of an electromagnetic wave and an uniform plasma, there is a maximum plasma density to which a light wave can penetrate [53]. This density is called critical density n_c and it is defined as,

$$n_c = \frac{m_e \epsilon_0 \omega^2}{e^2} \tag{2.67}$$

where m_e is the electron mass, ϵ_0 the vacuum permittivity, e the electron charge and ω the angular frequency of laser radiation. From equation 2.67 it is clear that the critical density scales quadratically as the angular frequency grows. Figure 2.12 shows the critical density for a range of angular frequencies from radio frequencies to EUV radiation. When the electron density of a plasma is $n_e < 0.5 n_c$, this is called underdense plasma and it will be almost transparent to a laser propagating through it. The other case when the electron density is bigger than the critical density, the plasma will be opaque for the laser pulse and it is called overdense plasma. In the intermediate range where the electron density is between $0.5 n_c$ to n_c the laser-plasma interactions are affected for the underdense and overdense parts of the plasma and influence the global interaction.

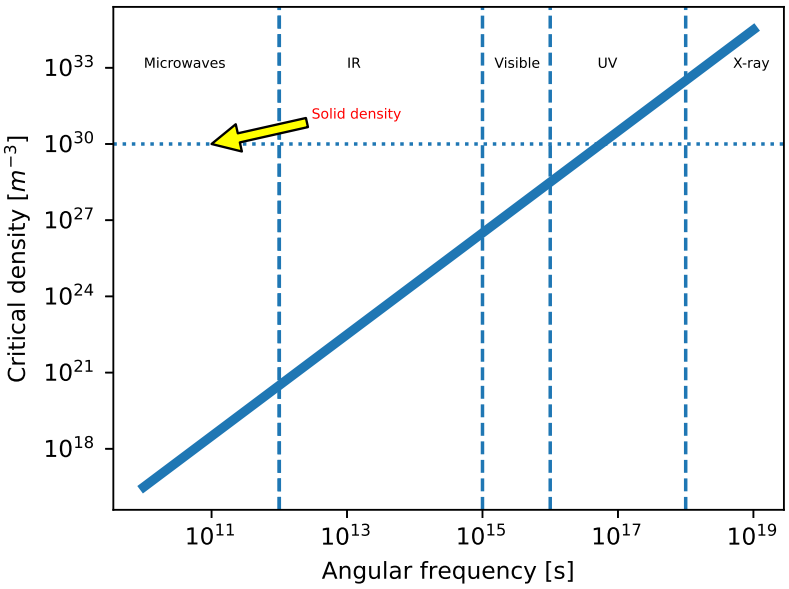

Figure 2.12: Critical density for a range of angular frequencies from radio frequencies to EUV radiation.

The effects of refraction and absorption for simulated underdense and overdense plasmas are studied in chapter 6 for two different laser wavelengths.

Chapter 3

Methodology

In section 3.1 the EUV laser is discussed, then AFM for analyis of the ablated craters is described in section 3.2 and the interference microscopy principles are described in section 3.3. An introduction to mass spectrometry is presented in 3.4. Sections 3.5 and 3.6 describe the models that are used: POLLUX and FLYCHK.

3.1 Capillary Discharge Laser

The type of laser used for the experiments with an EUV source were performed using a capillary discharge laser. For the experiments in chapter 4 and 5 were used two slightly different types of capillary discharge lasers, but the underlying principles are the same in both cases.

The lasing process occurs in an argon medium optimised at 300 mTorr inside of an aluminium oxide capillary tube of 21 cm during a pulsed plasma discharge. A diagram of this process is shown in figure 3.1. The main stages during the lasing process inside the capillary are described in this figure, first the preionisation of the argon gas, then the current accumulated flows through the Ar column and pinch the column, finally the laser pulse is produced. A Rogowski coil is located around the capillary housing, this is the main diagnostics of the capillary discharge. This triggers the following events in each particular set-up of the experiments. The laser is placed on an optical table and it has two main components: the capacitor bank and the capillary housing. The capacitor bank accumulates enough charge to quickly deliver it into the capillary tube. In the capillary housing, the capillary tube is inserted from the capacitor bank end into a hot brass electrode, while the other end stems out and it is connected in a ground electrode with a hole in the middle. Through this hole the argon flow is injected, the pumping system is also connected here and the light is extracted. Transformer oil is continuously pumped all over the capacitor bank and in a gap between the capillary housing and the capillary tube.

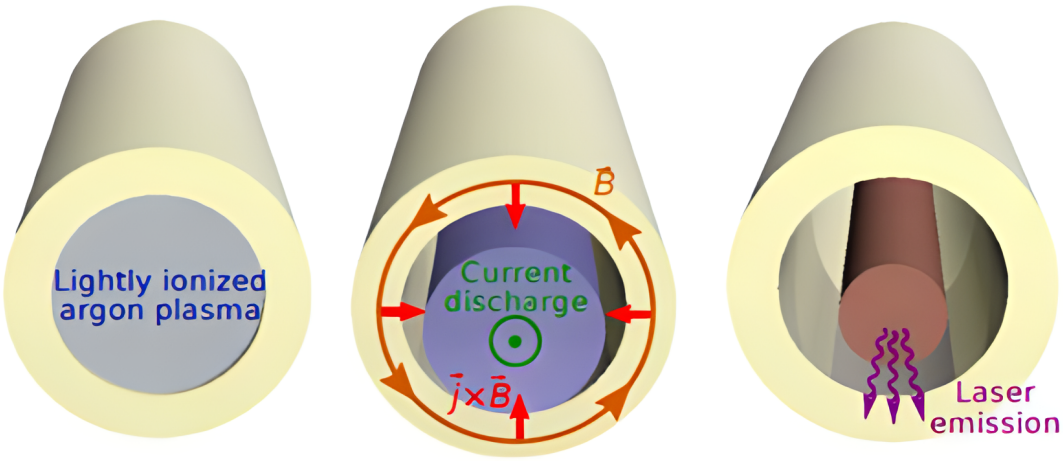

Figure 3.1: Schematic representation of the capillary discharge lasing process [4].

The whole laser system has a differential pumping vacuum system divided by apertures. In the case of the experiments described in chapter 5, there is an argon attenuation cell of 10 cm length located in front of the capillary tube. This argon cell attenuates the laser through argon photoionisation and the attenuation factor is controlled by changing the argon pressure in the cell.

The samples are placed inside the interaction chamber. In both experiments there were at least these diagnostics tools, a high vacuum gauge, venting and safety valves and between the laser exit and the interaction chamber, there is an aluminium inline photodetector which provides a relative measure of the beam intensity.

Specific arrangements and more detailed descriptions of the laser setups are described in chapters 4 and 5

3.2 Atomic force microscopy

Atomic force microscopy is a microscopy technique developed in 1985 by Binning *et al.* [54]. This technique is rather different from other more intuitive microscopy techniques relying on focusing light or electrons onto a sample and measuring the scattered light using either the naked eye or electronic sensors. In an Atomic Force Microscope (AFM) an element interacts directly with the sample to create a height map of the analysed sample's surface. This characteristic makes AFM different compared to 2-dimensional images obtained from optical and electron microscopes. There, to get information about the third dimension, you need to rotate the samples at known angles to infer an estimation of the height from 2D projections. In an AFM, information about the height (3rd dimension) is measured directly. An AFM obtains the height data by scanning across the surface, which means that the

data collected cannot be interpreted in real time, but needs some data analysis before it can be visualised. However, with available computational methods, it has become very easy and quick to analyse and visualise the data to obtain features such as depth, height, length volume and width of the sample.

AFM in comparison to traditional optical techniques can be more than 1000 times higher resolution. Typically, commercial AFM devices can have a vertical resolution of fractions of Angstrom and a horizontal resolution of 1 nm [55]. In AFM, a micro- or nanoscale cantilever with a sharp tip at the end interacts with the sample to measure the surface at the nanoscale level. This method presents different advantages and disadvantages depending on the operation mode. As mentioned, the high resolution of this method is the main advantage. Some of the most important disadvantages are related with the interaction process between the tip and the sample, for instance, lateral forces can distort the image, normal forces can be also strong enough to distort the image. These reduce the spatial resolution and may damage soft samples. Furthermore, another important disadvantage is the slow scanning time of a sample. Further detail of these interactions are discussed in the following sections.

3.2.1 AFM principles

The atomic force microscope relies on a simple principle, it measures the force between a tip and the sample surface interacting as they approach at small distances. This measured force results from the interaction through different mechanisms between the surface and the tip, for instance: van der Waals, electromagnetic or friction forces to name the most common ones. The magnitude and direction of this interaction is related directly to the sample-tip distance and this is the foundation of the technique. There are three scenarios for sample-tip interaction, depending on their distance. If the sample-tip distance is long, the interaction is negligible. At some closer distance the force will be attractive and the magnitude will increase. If the distance decreases more, a repulsive force is exerted, these are the three possible scenarios in the sample-tip interaction. This force-distance dependence is recorded and analysed to create a map of interactions that could be used to generate topographic images.

In order to measure these interactions different approaches can be taken. In modern AFM devices the sharp tip that interacts with the sample's surface is located at the end of flat spring named the cantilever. The force between the tip and the sample can be measured directly using the cantilever deflection which is proportional to the force exerted. One method of operation is called static mode, where the cantilever is a spring with a known spring's constant k. Using Hooke's law $F = -kz$, where F is the force exerted to the spring, k is the cantilever spring's constant and z is the distance the cantilever is bent relative to its equilibrium point. The most common technique to measure the cantilever's bending is usually using a laser beam reflected from the back of the cantilever and measured with a photodiode array, as shown in figure 3.2

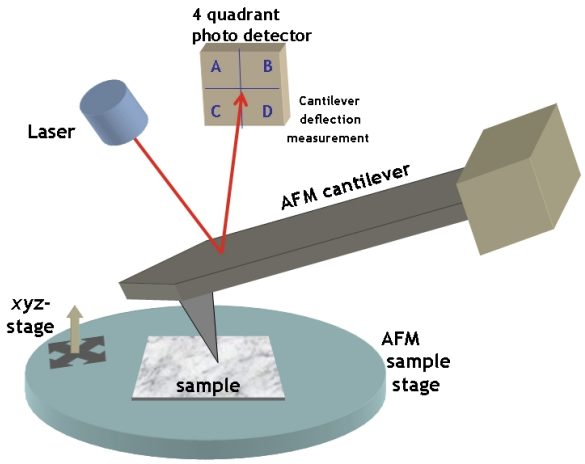

Figure 3.2: Schematic set-up of the main components in an atomic force microscope. This illustration was made for the Opensource Handbook of Nanoscience and Nanotechnology by yashvant is licensed under CC BY 2.5

All the samples measured in chapter 4 were measured in oscillating mode. In this mode, the distance between the sample and the tip is larger and there is not direct contact. Instead the cantilever is made to oscillate and the frequency is changed to match the resonance frequency of the system. Then, as the tip is moved across the surface, the attractive and repulsive forces will change if the tip-surface distance changes. This results in a change in the cantilever resonance frequency. By changing the oscillation frequency, the new resonance frequency is found and the change in frequency can be related to a change in tip-sample distance, which is what is measured. As a result of this, the resonance frequency and the cantilever oscillation amplitude change. This method is especially useful for soft materials such as biological samples, where direct interaction between the tip and the sample can cause damage.

3.2.2 Harmonic Oscillator

Oscillations have a key role in the basic principles of atomic force microscopy, whether in static or dynamic mode. Harmonic oscillations are the foundations of the cantilever motion, there are different descriptions for the cantilever depending on the operation mode and the accuracy required. The free harmonic oscillator is the simplest way to describe the motion of a mass on a spring as it is the case in the cantilever idealisation in static mode. A more realistic modelling of this motion is described as a harmonic oscillator with damping, which is the case due to in most of the AFM devices work in normal air conditions or with samples submerged in liquids. In the case of static mode operation, this harmonic motion describes the cantilever oscillations. For dynamic mode, a constant external excitations is used and this can be modelled as a driven harmonic oscillator for the simplest approach and as a driven harmonic oscillator with damping for a more realistic mode.

The simplest way to picture a free harmonic oscillator is as a mass attached on a spring. If the spring hangs in vertical position, the point where the mass rest in equilibrium is the point zero. Any displacement z to this point is related with the force exerted through Hooke's law as,

$$F = -kz \tag{3.1}$$

Where k is the spring constant. Conventionally, when the spring is elongated, the position value z is negative and the direction of force is positive. The minus sign in equation 3.1 appears because of the displacement has a direction in the opposite direction of the force. The equation of motion for the mass m is derived from Newton's second law, as follows

$$m\frac{d^2z}{dt^2} = m\ddot{z} = F = -kz \tag{3.2}$$

The solution to this ordinary second order equation is widely known, and its general form is

$$z = A\,cos(\omega_0 t) + B\,sin(\omega_0 t) \tag{3.3}$$

where $w_0 = \sqrt{k/m}$ is known as the angular frequency and physically describes that heavier masses moves slower and if the spring constant is stronger, the mass will move quicker in the linear region. This ω_0 frequency is called the natural or resonance frequency of the oscillator and it does not depend how far the spring is elongated. Equation 3.3 has two constants A and B that can be determined for the particular conditions of the system and once they are known this equation is valid for any time t.

Free harmonic oscillation is a first approximation to describe the cantilever motion oscillating in a free environment, which is not the case when a sample is measured in static mode. To describe a more realistic interaction damping needs to be include in the equation of motion. The first additional force taken into account is friction, resulting as the viscous damping from the air or liquid medium in the cantilever surroundings. The friction force is proportional to the velocity $\dot{z}$ and is exerted in the direction opposite to the velocity as

$$\mathbf{F}_{fric} = -\beta\dot{z} \tag{3.4}$$

where the proportionality constant β is linked with physical parameters. Usually this constant is defined by $\beta = \frac{m\omega_0}{Q}$. Q is known as the quality factor and for $Q > 1/2$ the systems is considered as an underdamped system.The equation of motion becomes

$$m\ddot{z} = -kz - \frac{m\omega_0}{Q} \tag{3.5}$$

equivalent to,

$$\ddot{z} + \frac{\omega_0}{Q} + \omega^2 z = 0 \tag{3.6}$$

This equation has a known solution $z = A\exp(\lambda t)$, inserting this solution in equation 3.6 it becomes,

$$\left(\lambda^2 + \frac{\omega_0}{Q}\lambda + \omega^2\right) z = 0 \tag{3.7}$$

Thus, equation 3.7 has to be solved as a quadratic equation, giving two possible solutions.

$$\lambda = -\frac{\omega_0}{2Q} \pm \omega_0 \sqrt{\frac{1}{4Q^2} - 1} \tag{3.8}$$

In an AFM system, ideally the Q factor is larger than 1 and we can rewrite this equation using complex numbers as,

$$\lambda = -\frac{\omega_0}{2Q} \pm i\omega_0 \sqrt{1 - \frac{1}{4Q^2}} = -\frac{\omega_0}{2Q} \pm i\omega_{hom} \tag{3.9}$$

Equation 3.7 is a homogeneous equation with two solutions derived from eq. 3.9 and the proposed solution $z = A\exp(\lambda t)$. The general solution can be written as follows

$$z = e^{-\frac{\omega_0 t}{2Q}} \left(Be^{i\omega_{homt}} + Ce^{-i\omega_{homt}}\right) \tag{3.10}$$

where the constants B and C are determined based on the initial conditions of each specific problem. This solution describes a more realistic interaction between the sample and the cantilever tip. However, it is only valid in the case when the microscope is used in static mode. The most common operating mode is when the cantilever oscillates near at its resonance frequency as previously described.

3.2.3 Forces

During the interaction in dynamic mode, a cantilever tip and a sample are in presence of a considerable number of forces interacting constantly. There are short and long range interactions. These includes, van der Waals interactions, chemical bonding forces, Pauli repulsion, elastic and adhesion interactions with the tip, as well as electrostatic and capillary forces. Van der Waals forces are the most significant interaction in dynamic mode when the cantilever is not in contact with the sample.

3.2.4 Van der Waals interactions

All the sample-tip interactions during the sample scanning process in AFM, van der Waals forces are one of the most important long-range contributions. Van der Waals interations are produced by a localised charge fluctuations in neutral atoms or molecules without a permanent dipole moment. In general this kind of interaction can be described as a force of

quantum mechanical nature and its exact description requires a quantum electrodynamical description.

In the simplest case of two noble gas atoms, their dipole interaction can be approximated by this analytical potential,

$$U_W(r) = -\frac{C}{r^6} \tag{3.11}$$

This potential is extended to a long range and it expands isotropically. It also has an additive property and the contribution of the potential created by two groups of atoms is summed in a new potential. For instance, in the particular case of a sample and a cantilever tip, there is a total contribution to the Van der Waals potential that includes not only the atoms in the tip apex, but also the contribution of the forces of the atoms in a larger volume including the inner atoms in the sample and tip. The infinitesimal contribution to the total Van der Waals force is described by equation 3.12, this considers the interaction of an infinitesimal volume element in the sample and an infinitesimal volume in the cantilever tip.

$$\mathrm{d}U_W = -\frac{C\rho_{tip}\rho_{sample}}{|\mathbf{r}_{\mathrm{tip}} - \mathbf{r}_{\mathrm{sample}}|^6}\mathrm{d}V_{tip}\mathrm{d}V_{sample} \tag{3.12}$$

where ρ_{tip} and ρ_{sample} are the atomic densities of the tip and the sample, respectively. C is the coefficient associated with the atom-atom potential. The force exerted by this potential is

$$F_W = -\frac{\partial U_W}{\partial d} \tag{3.13}$$

Van der Waals forces are the strongest force for distances larger than 1 nm. There are some kind of forces at shorter distances related to the chemical bond forces. There are also in some cases metallic bonds and interactions that require a quantum mechanical study such as Pauli repulsion [56].

3.2.5 Electrostatic forces

Another strong long range force during the sample-tip interaction during sample analysis in AFM is the electrostatic force. These interaction occur when there are electric charges trapped on the sample surface or on the tip but also when the tip and the sample are conductive materials and they are at different potentials.

The tip-sample interaction can be modelled as capacitor with a variable distance $C(z)$, then the stored energy in this capacitor system changes if there is a voltage difference ΔV and it is given by

$$E_{el}\big(z, \Delta V\big) = -\frac{1}{2}C(z)\Delta V^2 \tag{3.14}$$

Then the electrostatic force is

$$F_{el}(z, \Delta V) = -\frac{\partial E_{el}(z)}{\partial z} = \frac{1}{2}\frac{\partial C(z)}{\partial z}\Delta V^2 \tag{3.15}$$

This equation gives an approximation of the electrostatic force and the value $C(z)$ is the capacitance of the system for a plate area A a a distance dependence $1/z$. In a common commercial AFM device, the produced force by these kind of interactions could be as large as $F_{el} \approx 1nN$.

3.2.6 Short-range forces

As previously mentioned, long-distance forces represent the main interaction recorded during the analysis of samples. There are some other forces at short distance and direct contact forces. Pauli repulsion, this comes from Pauli's exclusion principle which states that two electrons cannot occupy the same state at the same time. During an AFM analysis, the atoms in the sample and in the tip enter an overlapping region and their electron levels start to be occupied mutually. This creates an effective repulsive interaction that is measured in the AFM micrograph.

Other types of short-distance interactions are the mechanical forces produced when the tip and the sample are in direct contact and produce an elastic force. Also, when the measurement is made directly in an open air atmosphere the relative humidity in the environment can produce some capillary forces. A thin film of water can exists in the sample and tip and when they are in close contact it can produce a meniscus creating an attractive force.

In this thesis, the static mode was used and the derivation from a change in resonance frequency to a 3D image was done using commercial software. The AFM used in this thesis was a Bruker Bioscope Resolve Atomic Force Microscope.

3.3 Interference microscopy

Interference microscopy is a non-contact technique which provides a full measurement of surfaces characteristics. In particular, white light interferometry is a powerful technique for optical measurements. Based on Yuri Denisyuk [57][58] work and developed by Emmeth Leith and Gary Swanson [59].

Interferometry is a technique based on the properties of light, particularly the phenomenon of interference patterns created when light is recombined after the amplitude division from a common light source. All these interferometry techniques are capable to measure the topology of a surface with nanometre accuracy over an extended field of view that extends from the micrometre scale to $\approx$ 1 m. Also, this allows the measurement of a huge variety of surface textures, starting from ultra-polished samples to woven textiles [60].

In this section a brief review of the most common interferometric techniques is presented. A description of the phase-shifting and coherence scanning methods are presented because

of their importance in the current full-field 3D interference microscopes.

3.3.1 Full-field Interference Microscopy

As previously mentioned, in comparison to tactile techniques optical imaging has important advantages for 3D areal surface topography; it provides a very sensitive measurement of the heights in sample surfaces and also the acquisition of parallel measurements of a vast amount of data points without scanning point by point across the surface. However, the major drawback of this technique is that a single height can be measured at a time and for a complete scan of an object, a large number of measurements and calculations are required. Another inconvenience of this technique is that materials need to reflect enough light to produce the interference pattern. The principles of this technique are based on the Michelson interferometry. In 1911, the fist idea of a device able to measure the roughness of a sample was proposed by George Sagnac: a non-contact interferometer based on amplitude division by a beam splitter, followed by the recombination of the two beams created. One of the beams interacts with the sample, the other beam is reflected in a reference mirror and these beams are recombined resulting in an interference pattern which gives the difference in the optical paths, one of which provides a reference wavefront and the other carries all the information of the height changes of the the sample. Figure 3.3 shows a general schematic view of the interaction.

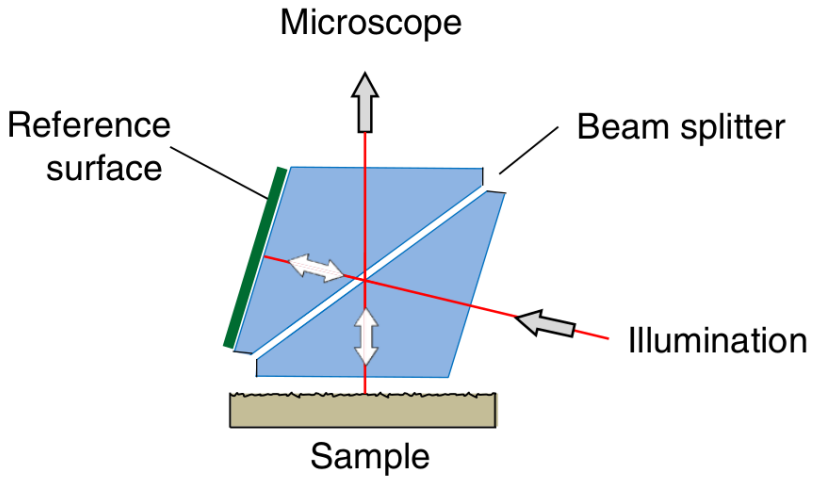

Figure 3.3: Beam paths in a basic white light interferometry device

The interference fringes acquired and illustrated in figure 3.4a are the backbone of this technique. The surface of an object is calculated based on complex processing on the interference fringes. Nevertheless, the surface form and texture of an object can be measured with a resolution as high as 1/10 of the source light wavelength. In modern devices, where the computing facilities do not represent an economical issue it is possible to reconstruct a complete 3D aerial view of the surface topography in real time.

An extraordinary evolution in this field was the development of the white light interferometry (WLI). This technique nowadays is one of the most widely used variations of interference microscopy used for the analysis of surfaces in industry. The interference pattern acquired in this configuration is sensitive to the overall optical path difference. The underlying principle consists of scanning through a range of height offsets and measuring the variation of the fringes generated as the optical path difference reaches zero for the samples in the field of view. This collection of different interference fringes at different heights creates a map of peak contrast and with the appropriate data processing a 3D image with all the surface topography. Figure 3.4 presents the measured interference fringes and the reconstructed surface morphology. WLI uses many wavelengths in comparison to laser interferometry which uses a monochromatic light source. This characteristic of WLI allows multiple data points from the same area on a sample, and for colour information from the samples.

This technique was used in this thesis for the analysis of the topography of different samples ablated with visible laser radiation. The ablation spot area for visible lasers is considerably bigger than EUV lasers. In general, AFM has a very limited scanning area in comparison to WLI, for this reason it was technically impossible to analyse the ablated material using an atomic force microscope and for that reason they were analysed with white light interferometry.

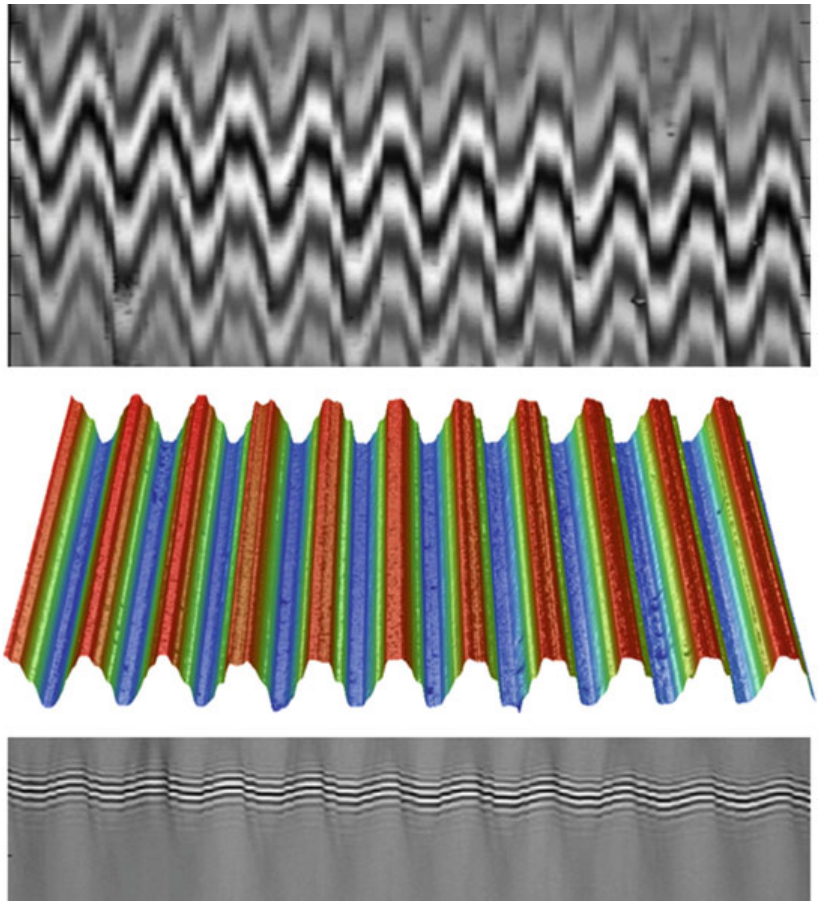

Figure 3.4: Object reconstruction using the fringe patter obtained in the top figure. The middle figure shows a computational reconstruction of the object based on the experimental fringes measured. Taken from Schmidt and Pakuła[5].

3.4 Mass spectrometry

Mass spectrometry is an analytical technique used in biology, chemistry, pharmacy among many related topics and research fields. The early works made by Thomson [61] and Aston [62] on the understanding of the characterisation of gas phases and the atomic characterisation of different elements respectively laid the foundations for modern spectrometry.

Nowadays, the most common mass spectrometers are time-of-flight, magnetic sector, linear quadrupole, linear quadrupole ion trap, quadrupole ion trap, cyclotron resonance and orbitrap. All these type of mass spectrometers rely on different approaches to discriminate different masses, either using magnetic or electric fields. For the experiments described in chapter 4 a time of flight mass spectrometer was used for the analysis of different materials. In order to understand the functioning and basic principles of TOF MS a brief introduction is given.

The first dated Time of flight mass spectrometer was designed and characterised by W.E.

Stephens in 1946 [63]. The underlying principle in TOF mass analysers is measure the time of flight for different m/z ions along a field-free drift in a known length. Figure 3.5 shows an schematic of a TOF MS and the process inside. In an ideal case, all the ions of different masses are introduced into the flying zone at the same time with the same energy or in practical terms at least within a sufficiently small time interval. This is a critical point of the TOF method, if the ions do not have the same energy, then this does not work. In practice this is achieved by accelerating them across a voltage and making sure that this acceleration energy is >> than the ion starting energy. Based on this, the lighter ions will get into the detection zone in a shorter time than the heavier ions. Independently of the ion production and handling, this method requires a pulsed ion source. TOF MS offers more advantages including the relative easy construction in addition to the in principle unlimited m/z detection range, the reliability in the detection of a complete mass spectra using a single ionisation/ablation event and its high acquisition rate, up to $>10^3$ Hz.

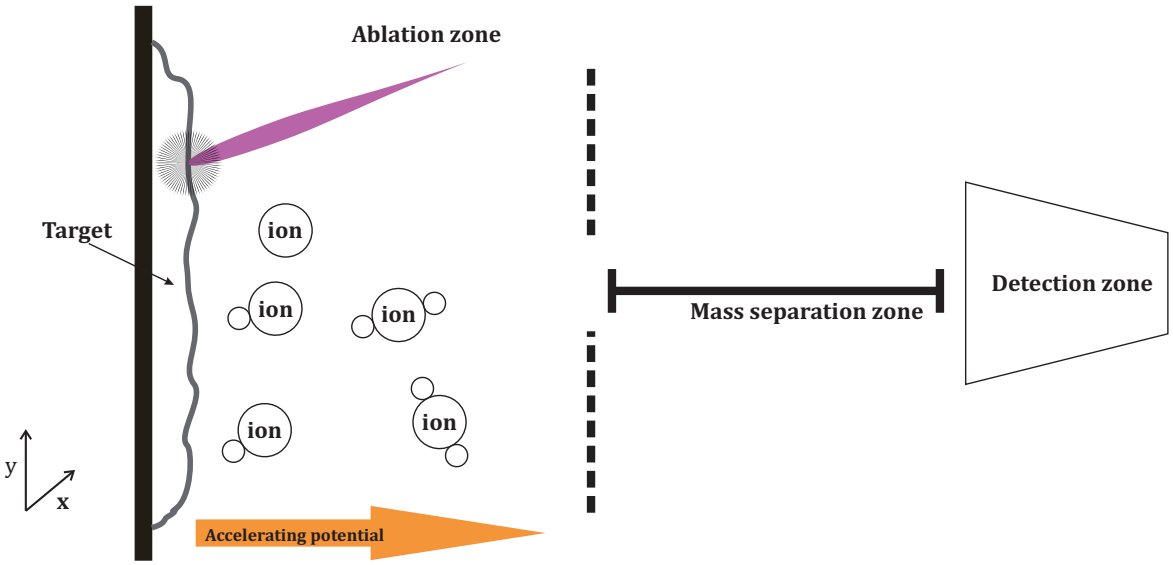

Figure 3.5: Schematic view of the ablation and acceleration processes of the target in the interaction chamber

As previously mentioned, we can precisely calculate the time for an unknown ion in travelling a distance s after being accelerated by a voltage U. An ion of electric charge q or ze and integer number z of electron charges e and a mass m_i. The energy E_{el} for this ion moving through the given voltage is

$$E_{el} = qU = ezU \tag{3.16}$$

This potential energy is converted into kinetic energy E_{kin} as follows

$$E_{el} = ezU = \frac{1}{2} m_i v^2 = E_{kin} \tag{3.17}$$

If the ion was initially at rest, or at least have an energy much smaller than ezU. Rearranging Eq.3.17 gives the velocity as follows,

$$v = \sqrt{\frac{2ezU}{m_i}} \tag{3.18}$$

For a given distance s, the time can be calculated simply as:

$$t = \frac{s}{v} \tag{3.19}$$

Substituting v from equation 3.18 the time becomes

$$t = \frac{s}{\sqrt{\frac{2ezU}{m_i}}} \tag{3.20}$$

Equation 3.20 yields the time needed for the ion to travel the distance s at constant velocity after the acceleration i.e. in a field-free path. Rearranging equation 3.20 we obtain the relationship between the experimental parameters s and U, the measured travelling time t and the mass ratio as follows

$$\frac{m_i}{z} = \frac{2eUt^2}{s^2} \tag{3.21}$$

A mass spectra is shown in figure 3.6, in this mass spectra the flight time was converted into m/z and the different ion peaks are clearly distinguishable.

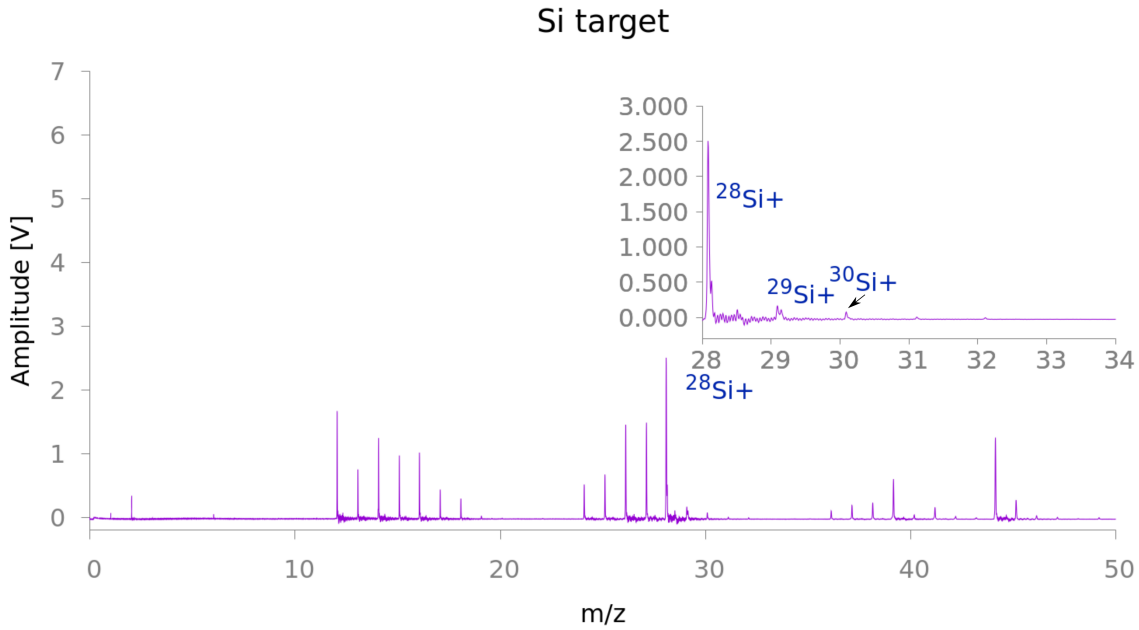

Figure 3.6: Mass spectrum of a silicon sample with the flight of time converted into m/z.

3.5 Pollux

Pollux is a 2D Eulerian radiative-hydrodynamic code [64] designed to model high intensity laser irradiation of solid targets and the interaction of this radiation with the highly ionised plasma created after the ablation of the target material. Hydrodynamic codes (hydrocodes) are computational tools for modelling continuous media and how they flow under different conditions. These type of codes can be adapted to treat different scenarios and can include material strength and rheological models to simulate the behaviour of different materials. In essence, a hydrocode considers the effect of all the external and internal forces interacting in a predefined mesh of cells, which represent the studied system. The vast majority of these codes solve the conservation equations of mass, momentum and energy using an explicit time stepping algorithm. Within these fixed time steps, it is assumed that all the forces are constant and they are used to adjust the properties within the mesh accordingly. Depending on the type of mesh hydrodynamic codes fall in two type of categories: Eulerian and Lagrangian. Eulerian codes have a fixed mesh and Lagrangian have a moving mesh.

This code solves numerically the equations for hydrodynamic flow in a flux-corrected model, following the implementation by Boris and Book [65] . This model is described with a set of three first-order quasi-linear partial differential equations. The detailed processes followed in Pollux are described in figure 3.7.

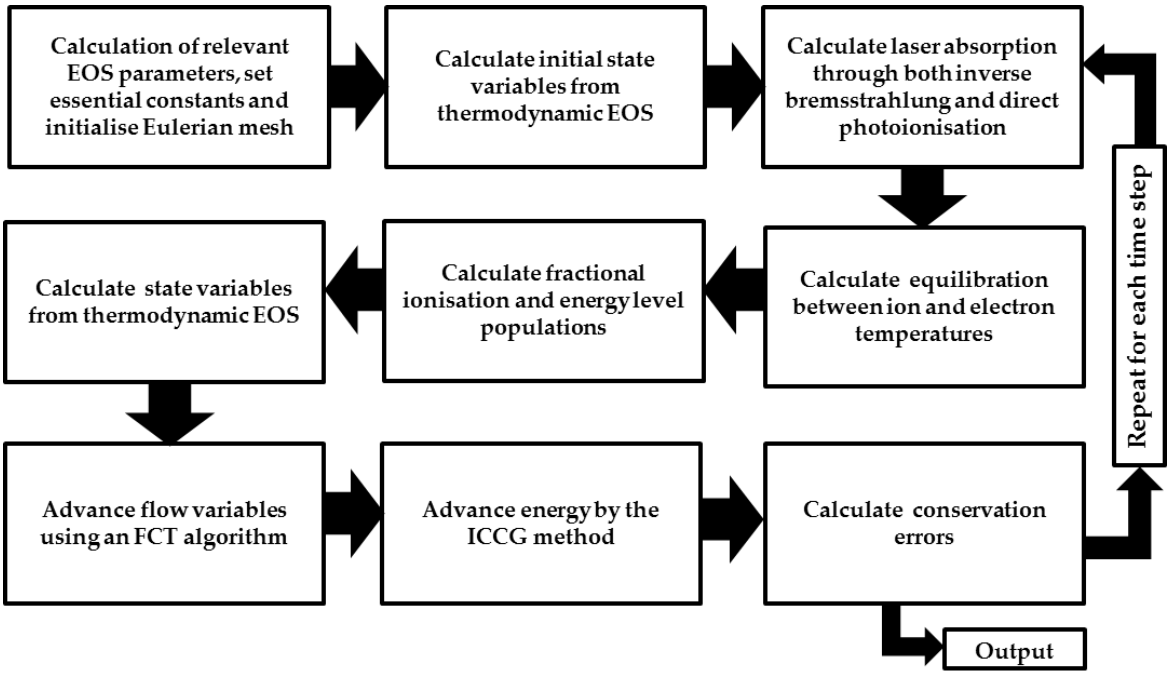

Figure 3.7: Algorithm for all the steps in Pollux for a simulation

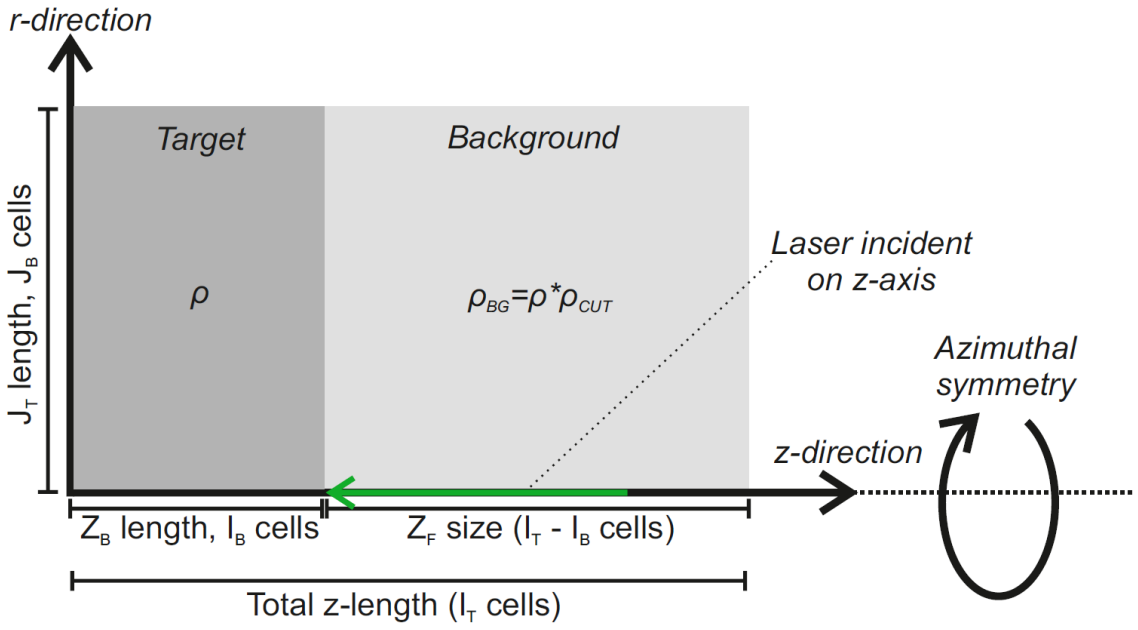

Figure 3.8: Schematic view of the geometry of the mesh within Pollux. Taken from D. Meehan doctoral thesis [6].

3.5.1 Quasi-Lagrangian

In hydrodynamic codes, generating a mesh to represent the material parameters and geometry is one of the most important tasks. Also, defining the boundary conditions is another critical step in the model development. The spatial degrees of freedom are especially important because they determine the number of cells created and the amount of computational power required to perform these simulations. Because of this, it is often required to do a simplification of the problem and reduce the dimensions of the experiment. For this reason Pollux is a 2D code that can represent 3D problems as long as they have an axial symmetry.

In Pollux, the mesh generation follows a hybrid approach. At first, the code uses a Lagrangian approach with a moving mesh conserving mass. This only lasts for the first iterations of the code to adjust the size of the cells close to the surface to reduce the computation time. After this, the approach becomes Eulerian and the mesh remains fixed and the computational power required reduces drastically compared to a moving mesh where the complexity of the geometry could consume a lot of memory.

Pollux creates a 2D mesh and azimuthal symmetry is assumed around the z-axis around the point of incidence of the laser and at a normal angle to the target. Figure 3.8 describes schematically the geometry of the mesh and the parameters that define it.

The mesh is defined by the physical size of the system including the size of the target and the background. The size and resolution of the mesh are defined in both the z and r directions. The resolution of the cells is defined by the number of cells chosen in each direction and the total dimensions of the system.

An important condition must be maintained at all times when solving partial differential equations numerically, the Courant-Friedrich-Lewy (CFL) condition [6]. This condition states that the matter in the cells cannot be discontinuous when it travels through cells. In other words, when a particle is moving in the system across a discrete grid, the time step duration computed must be small enough that the particle can not skip a cell.

The CFL condition for Pollux is:

$$C = \frac{u\Delta t}{\Delta x} \leq C_{max} \tag{3.22}$$

where C is the called Courant number and Δt and Δx are the time step and length interval. C_{max} values varies depending on the type of time integration used to solve the equation, but in general it is equal to 1 or less. From a physical point of view, this condition implicates that any particle travels more than one grid cell during a time step.

3.5.2 Equation of State

The equation of state in a hydrodynamic code is another fundamental part that relates the pressure to the density and internal energy. Pollux at the beginning of the calculations starts with the energy absorption deposited by the laser in the target material. The energy depostion is based on inverse bremsstrahlung absorption. In all the simulations in this chapter, the laser source utilised was a Nd:YAG at 532 nm laser and the inverse Bremsstrahlung is the main absorption process due to the wavelength of the laser. Multi-photon processes are not taken into account given the wavelengths and moderate intensities of the lasers under study.

As discussed, the IB process is the main mechanism of energy absorption and it produces the change in the phase of the irradiated target. To describe the phase changes an equation of state (EoS) is needed. Pollux uses the Chart-D EoS [66] model developed by Sandia National Labs. This model calculates different material properties from input data such as density, thermal conductivity coefficient, enthalpy of sublimation, bulk model that define the material and how it will respond when energy is deposited in it.

Once all the parameters in the equation of state are defined, it is posible to model any change of phase in the target as the energy is absorbed. During the interaction between laser radiation and matter, there is an increase in temperature and a change of pressure in the target and the proper change of phase in the regions of interactions are calculated by this EoS. A Thomas Fermi model is used for the calculation of the electron component of the EOS [67].

3.6 FLYCHK

FLYCHK is a code suite developed by Chung *et al.* [68] at the Lawrence Livermore National Laboratory to simulate plasma spectroscopy. These computational tools were developed

to understand different novel plasmas created using x-ray lasers, ultra-short pulse lasers, Z-pinch machines and high power lasers like the National Ignition Facility. This code is capable of studying new plasma generation schemes, warm dense matter, extremely hot and dense matter and highly transient states of matter.

In general, FLYCHK is capable of calculating the atomic level population distributions in a plasma. It was designed to work from low to high Z ions under most of the laboratory conditions. It includes coronal, local thermodynamic equilibrium, steady-state or time-dependent models and it can simulate plasmas containing single species or mixtures. FLYCHK employs a schematic atomic structure and processes for population distributions calculations. It includes a set of atomic structures with all the ionisation stages for atomic numbers up to Z=93. The population distributions are calculated by solving the rate equations considering collisional and radiative processes.

Chapter 4

A comparison of ablation mechanisms at different wavelengths

4.1 Laser ablation principles

This chapter presents the results of ablation experiments on different materials. The ablations were performed using two types of laser sources, an optical laser at 532 nm and an EUV laser at 46.9 nm. The results obtained helped to understand the main matter-interaction differences using these two types of wavelengths.

As explained before in section 2.2, for visible light ablation begins as bound electrons absorb the energy provided by the laser through multi-photon processes, these electrons acquire enough energy to detach from the atom and form a plasma. These free electrons start to dominate the absorption processes mainly through inverse bremsstrahlung and non-linear interactions when the density is close to its critical value [69]. If the laser pulse continues depositing energy into the plasma, it is absorbed by the free electrons and it is conducted through the plasma to the target surface leading to hydrodynamic flow and plasma ablation. The final results of ablation depend on different parameters such as the laser intensity, wavelength and the material characteristics.

EUV radiation interacting with matter differs substantially from the type of interaction and processes using optical, IR or UV lasers. In this particular regime, the critical electron density is greater than solid density and the photon energy is enough to photoionise the material, unlike IR or UV lasers where the predominant ionisation mechanism is inverse Bremsstrahlung. As discussed by Barkusky *et al.* [70], damage threshold research for optical elements in EUV or SXR laser setups is required to explore the limitations and advantages of these shorter wavelengths. The ablation mechanism is different in EUV because of the photoionisation. This has an effect on the plume formation and expansion, but in particular

it will influence the ablation and damage threshold of the material. This is especially relevant for the optics of EUV laser applications. In contrast to optical, IR or UV lasers where the underlying material interactions in optical components have been studied broadly; at short wavelengths more work is required since a different type of optical components such as multilayer and grazing-incidence mirrors are used.

This chapter presents investigations into how the ablation rate and maximum depth change as function of the number of laser pulses deposited in the targets. Materials with different attenuation lengths were chosen to investigate the ablation mechanisms. The results confirm that the crater shape and ablation rate are closely related with the wavelength of the laser pulse used. The ablation rate obtained with visible light are in accordance with previous experiments were the removal of material tends to an asymptotic limit as the laser energy deposited in the material increases [71]. Ablation with EUV radiation shows the same exponential decay in the average material removal as the number of shots increase.

4.2 EUV and optical ablation experiments

The experiments were performed in two different laboratories. The EUV ablation part was carried out in the facilities of the *Engineering Research Center for Extreme Ultraviolet (EUV) Science and Technology* at the Colorado State University (CSU) while the visible laser ablation experiment was performed in the facilities provided by *The York Plasma Institute Laboratories* at the University of York.

As mentioned in section 4.1, ablation of different materials, such as organic polymers and metals by optical radiation has been extensively studied [27] [72] . However, there are fewer studies about polymer and metal ablation induced by EUV radiation below 100 nm. In this and the following sections are presented the experimental set-up and a series of results comparing EUV and optical wavelength ablation experiments. Au, Cu and PMMA targets were irradiated with a intense focused laser beam at 46.9 nm and Cu, Al and Si using a 532 nm laser source. Cu is the only material ablated with both lasers, the other materials (apart from Cu) were chosen to provide a range of attenuation lengths.

The optical ablation experiments were performed using a commercial Continuum Minilite II laser described in table 4.1. A set of mirrors and a focusing lens with a focal length of 50 cm and an f-number $\sim$ 20 was used to focus the laser pulse onto the target inside of a vacuum chamber at $\sim 2 \times 10^{-2}$ mbar.

Table 4.1: Laser parameters for the 532 nm laser source

Laser parameters	
Visible	
Wavelength:	532 nm
Energy output:	up to 30 mJ
Pulse length:	3-5 ns
Repetition rate:	up to 15 Hz
Linewidth:	≤ 0.1 cm^{-1}

Table 4.2: Laser parameters for the EUV laser source

Laser parameters	
EUV	
Wavelength:	46.9 nm
Energy output:	up to 80 μJ
Pulse length:	$\sim$1.5ns
Repetition rate:	up to 10 Hz
Monochromaticity:	$\Delta\lambda/\lambda < 1\times10^{-4}$

The different samples were primarily chosen due to the different attenuation length range. In addition they have other differences such as density and latent heat. For the materials used in the optical ablation experiments the attenuation lengths were obtained from the *Handbook of Optical Constants of Solids* [73] and they are presented in table 4.4.

Table 4.3: Attenuation lengths of the different materials used in the 532 nm ablation experiments.

	Attenuation length $[m]$	Density $[g/cm^3]$	Latent heat $[kJ/kg]$
Al	4.10×10^{-7}	2.7	31704
Cu	5.20×10^{-7}	8.9	4730
Si	2.30×10^{-7}	1.18	12,800

The EUV experimental set-up consist of an arrangement of spherical mirrors located in an onward position with respect to the samples to focus the laser backwards onto the targets. The focusing process is substantially more complicated than conventional optical lasers and required additional efforts for an optimal positioning of the sample and a normal

incidence onto the mirrors. The detailed alignment process and the focal point calculations are described by S. Wilson [74]. A more detailed explanation about the experimental set-up is given in the following section.

The relevant parameters for the EUV source are described in table 4.2 and the attenuation length of the materials ablated in this wavelength are presented in table 4.3.

In both cases the number of shots were calculated to have a similar amount of total fluence in each material.

Table 4.4: Attenuation lengths of the different materials used in the EUV ablation experiments

	Attenuation length $[m]$	Density $[g/cm^3]$	Latent heat $[kJ/kg]$
Au	5.98×10^{-9}	19.25	1645
Cu	1.05×10^{-8}	8.9	4730
PMMA	2.40×10^{-8}	1.18	170

4.2.1 Experimental set-up

4.2.1.1 Optical ablation set-up

The target ablation was carried out using a Minilite Q-switched Nd:YAG laser by Continuum at 532 nm. The alignment process is substantially easier than it is using EUV light, due to the ability to track the beam along its way to the interaction chamber. For the alignment process, the laser is set to low-power mode and two mirrors were placed at 18 mm from the laser output in an open atmosphere before it is directed onto the sample inside the interaction chamber. A schematic diagram of the experimental arrangement is presented in figure 4.1. All the samples used were bought from Goodfellow and were cut into strips of 50 x 50 mm. These samples were cleaned using isopropyl alcohol and placed on a quartz holder.

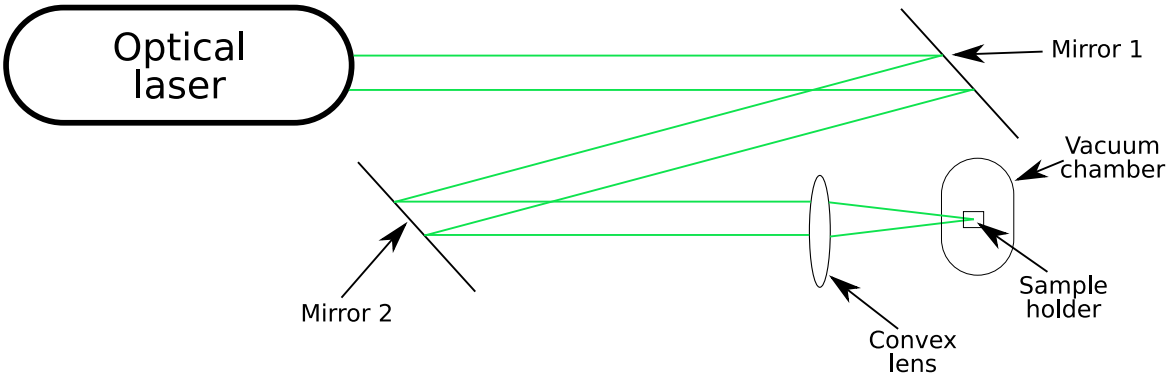

Figure 4.1: Schematic representation of the optical ablation experiment. Two mirror guided the laser beam into a convex lens to focus the laser beam onto the sample.

The samples were mounted on a quartz glass to fit in the sample holder and then introduced in the vacuum chamber at a pressure of $< 3 \times 10^{-2}$ mbar. Before and after the ablation shots the laser energy is measured using a GENTECH energy meter to ensure the stability of the laser pulses. The output beam can be attenuated directly at the output using the built-in attenuator in the front part of the laser if required. The laser output diameter provided by the manufacturer is 1 mm, the lens configuration provide an estimated spot size diameter at the target of 0.60 - 0.88 mm. The focusing lens has a focal length of 50 cm and an f-number ~ 20. The incidence was at an angle of 45°. Ideally the best incidence angle would be 0° but due to experimental limitations it was not possible. The entrance window is located in one arm of the vacuum chamber at 45°. Nevertheless, the most important interaction is the energy deposited on the target and the total fluence on target independently of the angle incidence.

The energy used for the experiment were intended to correspond with the same fluences used in the EUV experiments. The area of the ablation spots for the fluence calculations was measured using the same materials before the experiments and when all the materials were ablated, the areas of the ablation spots were measured again using an optical microscope and using the tool for area measuring in the data analysis software provided by ProfilmOnline. In this experiment, the laser energy was constantly monitored and the energy variation from pulse to pulse is normally distributed around the maximum energy with a variance of 3 % as showed in figure 4.2 . These energy measurements helped to keep a continuous monitoring of the laser fluence at each ablation spot. During the experiments the sample holder was rotated 30° once the number of shots were completed.

For this experiment, the analysis of the ablation spots consisted first of using an optical microscope to estimate the ablation area. Because of the different parameters of the MiniLite laser, the ablation spots exceed the maximum area of the Bruker Microscope used for the analysis of the samples ablated using EUV radiation. To determine the morphology and depth of the ablation spots, they were analysed using white light interferometry (WLI).

This technique is described in section 3.3 with depth profiles and the ablation morphology extracted for further calculations.

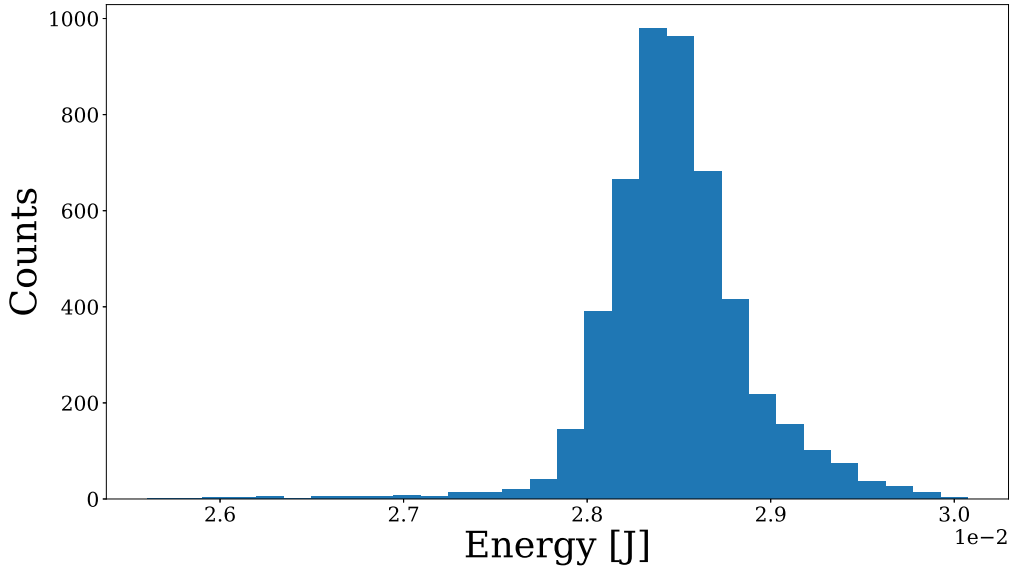

Figure 4.2: Histogram of the laser energy measurements at 532 nm and 30 mJ.

4.2.1.2 Extreme ultraviolet ablation set-up

The experimental arrangement consists of a set of on-axis spherical mirrors to focus the laser beam backwards onto the sample. Figure 4.3 shows a schematic representation of the mirrors and target setup. Two spherical mirrors are used in the experimental set-up following the recommendations expressed by Wilson [74], this configuration cancels out any spherical aberration produced by one mirror and theoretically this produces a diffraction limited beam. In preparation of the ablation of the targets, the laser beam needs to be focused in the optimal position. Given the characteristics of the EUV laser beam, it needs to be aligned and focused indirectly and is substantially more complex than its visible laser counterpart.

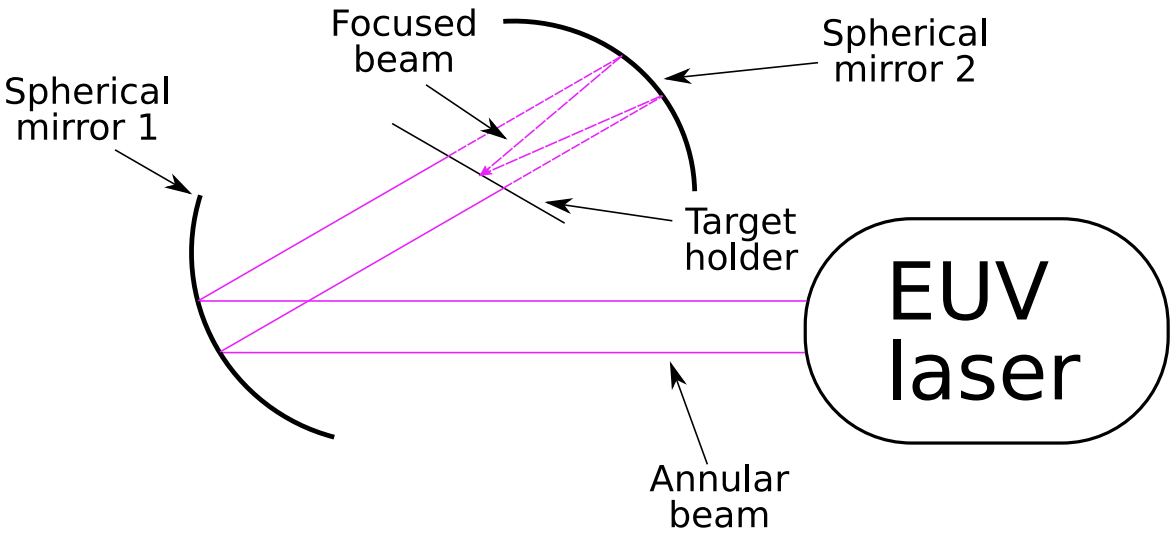

Figure 4.3: Schematic diagram of the experimental setup used in the EUV experiments. A pair of spherical mirros guided the laser beam onto the sample. All this setup is located under vacuum conditions.

The alignment of the laser before the ablation of the samples, consists in two complementary processes to find the best focus on the targets. First, imaging the shadow produced by two cross wires into an Andor iKon-L CCD camera. The cross wires are shaped as a '+' and '×' and located in the estimated beam path. The laser beam is fired onto the camera and when the shadows overlap with the centre of the annular beam on the CCD image, then the laser is aligned. As an alternative process, two glass slides coated with a thin layer of PMMA were placed in the beam path using an 'U' shaped holder. The first slide facing the laser is fired and removed and the laser is fired onto the second slide. After this process the slides are developed in a solution of isopropylacetone to reveal the beam position. The slides are placed again in the holder and the target, a strip of material about 2×5 mm is taped onto the back of the slide. A helium-neon laser is used to align the system through the centre of the target. These are the two procedures followed for the perpendicular alignment of the laser.

When the laser beam was perpendicularly aligned, a dummy target was placed close to an estimated focal point based on the previously alignment process. Then a z-scan (along the beam direction) position was performed to locate the point where the focal spot size is minimised. Once, this focal point was found, the target strip was ablated in a pattern of consecutive craters from 1, 5, 10, 20 and 50 shots. Finally, the target strip is removed from the ablation chamber and examined using an optical microscope to verified if the ablation experiment was successful. Figure 4.15 shows a representative ablated target indicating the multi-shots craters.

Once the best position is located, the samples of interest were introduced one by one after the ablation patterns were completed.

4.3 Ablation micrographs

After the ablation experiments, the craters created need to be analysed to quantify the depth and area ablated by the lasers.

The samples ablated with visible light were analysed using white light interferometry, as explained in section 3.3 this techniques is based on the principle of interferometry and the topography of the sample is reconstructed using interferograms. The samples ablated with EUV radiation were analysed using an atomic force microscope, specifically a Bruker Bioscope Resolve Atomic Force Microscope in the The York JEOL Nanocentre. In this case, the sample topography is measured through the interaction of an oscillating cantilever that moves around the surface of the sample, as explained in section 3.2.

Initially, given to the direct access to the AFM facilities both type of ablated surfaces were planned to be analysed in this microscope. However, the X-Y scan range is limited to 100 μm and the Z range to 15 μm. In the case of the EUV ablation spots, the scanning ranges were not a problem, but in the optical laser the ablation craters had a diameter of 0.5-0.8 mm which is out of the range of the AFM microscope. For this reason white light interferometry was used for the scanning of the samples.

In both cases the micrographs give comparable information about the surface morphology and the ablation depth. The same analysis methods were used for both techniques, 10 profiles were extracted and their mean value was used to determine the maximum ablation depth.

4.3.1 Optical micrographs

The samples used were ablated multiple times in the same spot to increase the total laser fluence. Similar to the EUV case, the pulse energy was constant and the number of shots were calculated to obtain similar fluence values to the EUV experiments. Figures 4.4, 4.5 and 4.6 show the characteristics of the ablation topography at maximum fluence for the different sample materials. The calculations of the ablation threshold and depth as a function of fluence are extracted analysing different depth profiles.

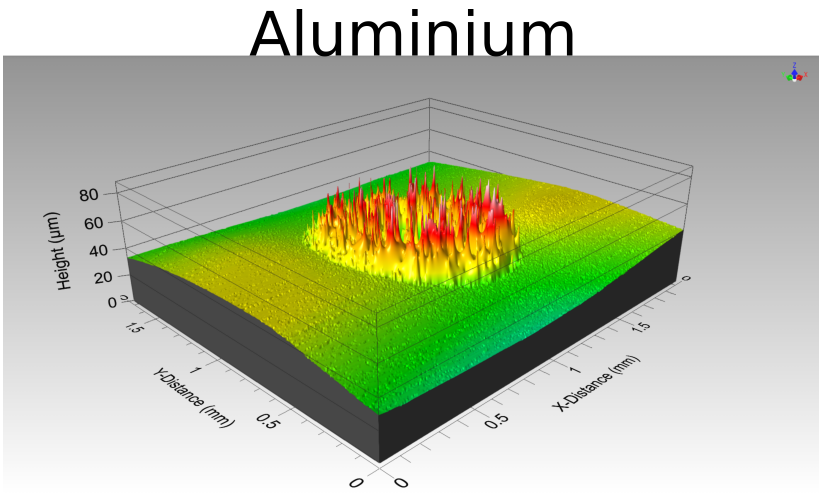

Figure 4.4: White light interferometry micrograph of an Al sample ablated with an accumulated energy density of E_{tot}=950 Jcm^{-2}

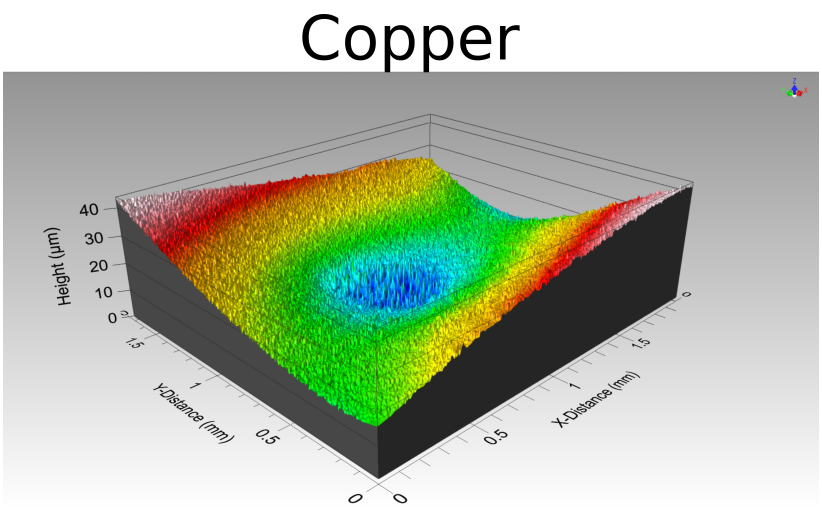

Figure 4.5: White light interferometry micrograph of copper sample ablated with an accumulated energy density of E_{tot}=570 Jcm^{-2}

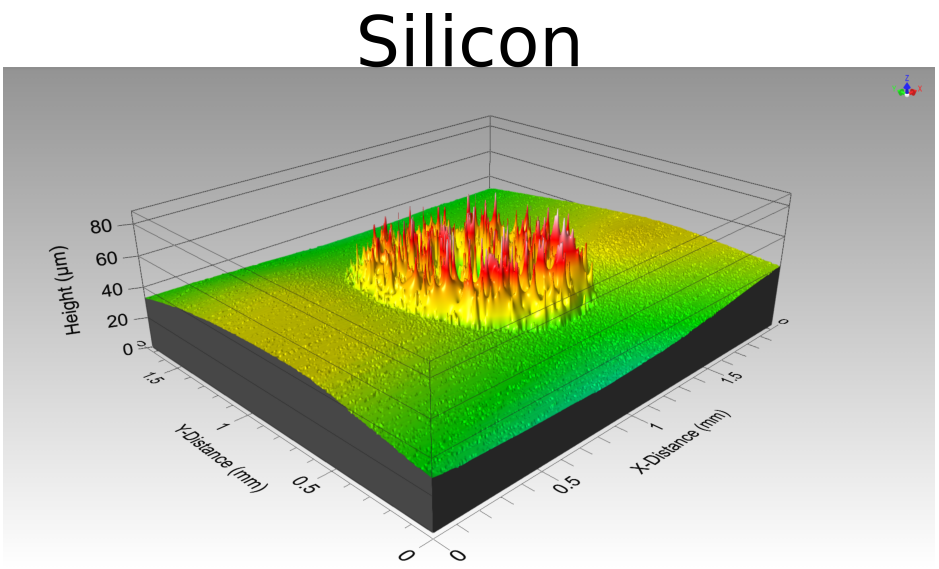

Figure 4.6: White light interferometry micrograph of a Si sample ablated with an accumulated energy density of E_{tot}=950 Jcm^{-2}

These micrographs show the information required for the analysis of the depth and spot size. All the samples showed an elongated shape very likely produced by the 45° angle of incidence of the laser beam. It is expected that the samples have an elliptical shape, with a crater longer by a factor of $\sqrt{2}$ in one direction due to this angle. Ten lineouts are extracted from the images and averaged to calculate the crater depth at different laser fluences.

4.3.2 EUV ablation micrographs

In this section are presented the laser-induced EUV ablation micrographs of metallic and organic materials analysed through atomic force microscopy.

The samples analysed were shot 1, 5, 10, 20 and 50 times at a constant fluence energy of 15 Jcm^{-2} per shot. In figures 4.7, 4.8 and 4.9 are presented the ablation craters for samples shot 10 times. The remaining samples have similar profiles.

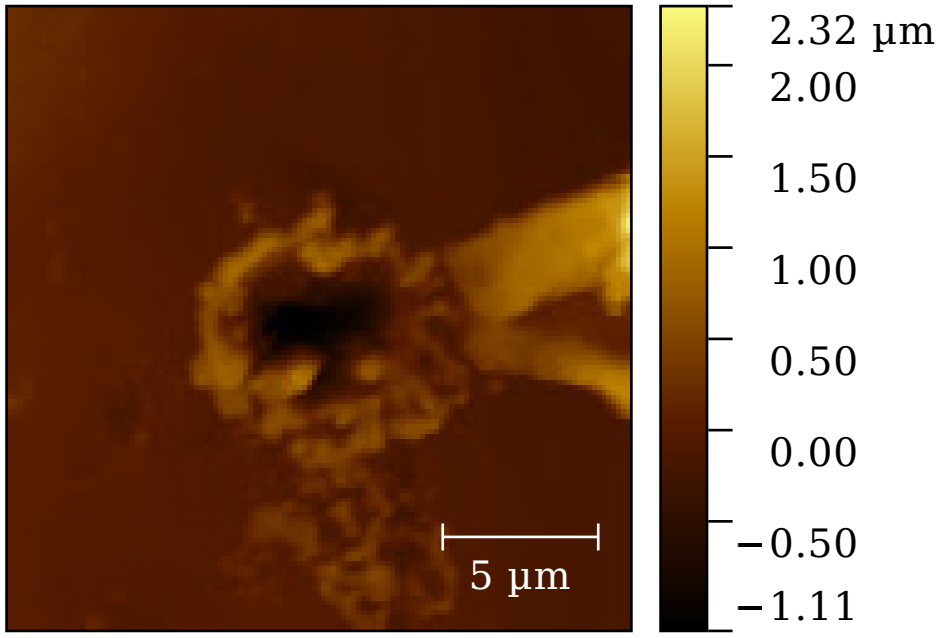

Figure 4.7: Au sample ablated with an EUV source with an accumulated energy density of E_{tot}=150 Jcm^{-2}

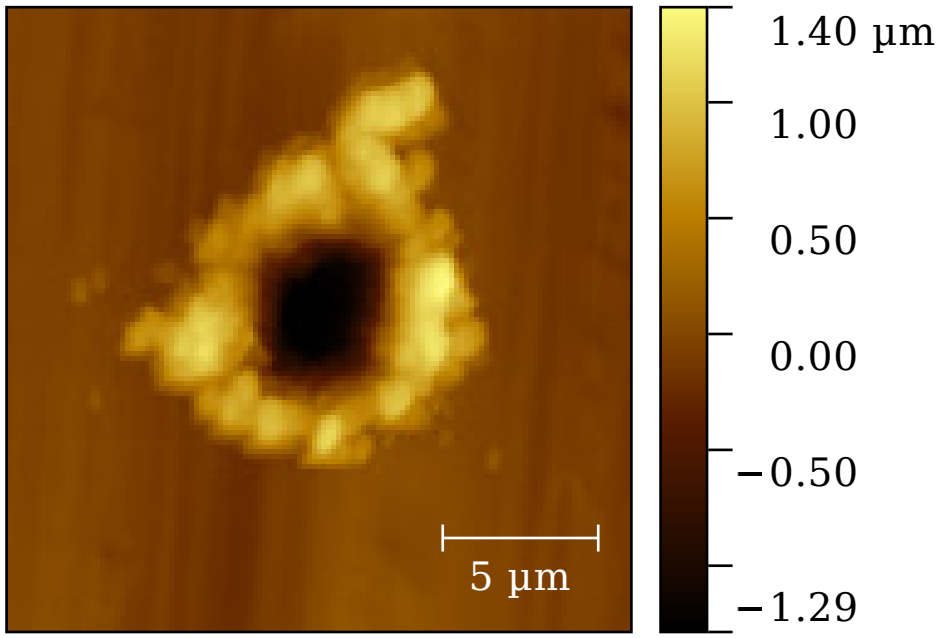

Figure 4.8: Cu sample ablated with an EUV source with an accumulated energy density of E_{tot}=150 Jcm^{-2}

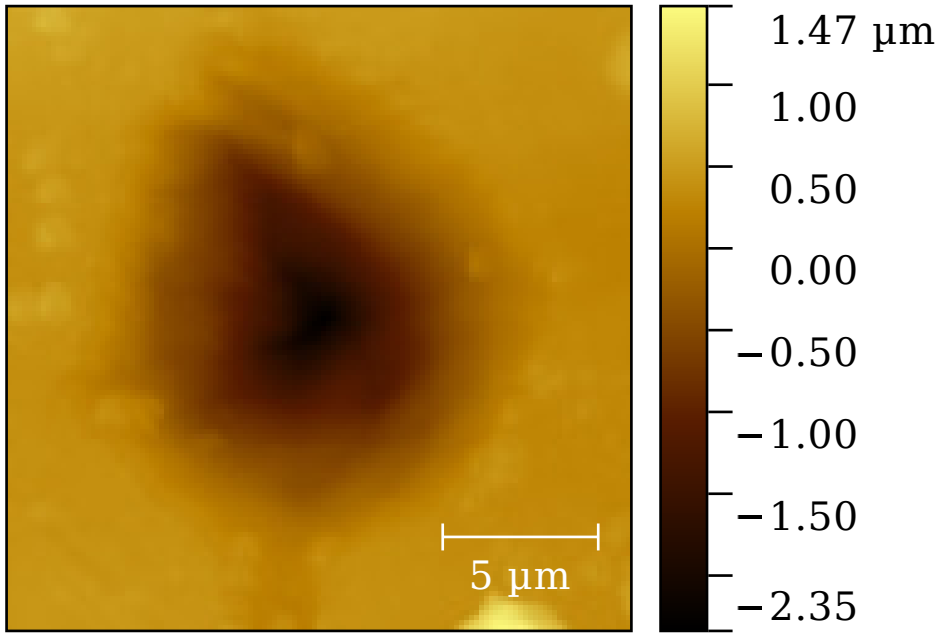

Figure 4.9: PMMA sample ablated with an EUV source with an accumulated energy density of E_{tot}=150 Jcm^{-2}

Taking into account the mirrors reflectivity of ∼8%, a ∼10% blocked part of the laser produced by the sample holder and other losses in the system, the total energy on the target is around 2-5% of the 70 μJ laser output. The micrographs analysed correspond to normal incidence conditions and the energy fluctuations were measured with an Ar in-line detector and they had an energy variation of ±20%.

The rims around the craters of Au and Cu targets indicate the ejection of molten material that resolidificates around them. This phenomenon was identified also during the ablation of solids using a free electron laser in the EUV reginme by Stojanovic *et al.* [75], it is known as "piston" effect and it is attributed to the pressure recoil of the ablating material. According to Stojanovic, the piston effect occurs when the lateral laser pressure exerted onto the material is significant in comparison to the normal pressure to the surface and it is typically observed for optical lasers in continuous wave and long pulse irradiation. In this case where the laser pulse duration is in the nanoseconds reginme seems to be long enough to occur this piston effect. The PMMA sample remained flat around the ablation spot, the ejection and material removal in this sample might occur through other mechanisms discussed later.

4.4 Crater shapes and ablation characteristics

The characterisation of the craters created with optical and EUV laser radiation followed the same procedure and are based on the ablation theory presented in section 2.2.2. This section

describes the analysis of the ablation micrographs and their comparison to the expected shapes according to theory.

Figure 4.10 shows an example of the lineout extraction process. The ablated holes were analysed measuring the height of the samples from the deepest point of the crater to the highest point in the surroundings of the hole. All the samples have a similar ablation pattern and the information of the crater shape and depth were obtained using either AFM or WLI techniques explained previously. Based on the micrographs from section 4.3.1 and 4.3.2 , the ablation depths and the ablation thresholds were determined using the logarithmic ablation law [69] derived from Beer-Lambert law [76]. Independently of the imaging technique used, the analysis is similar in each case. Based on the shape of the laser pulse and the posterior analysis, it is possible to extract more information of the shape of the sample and some characteristic parameters.

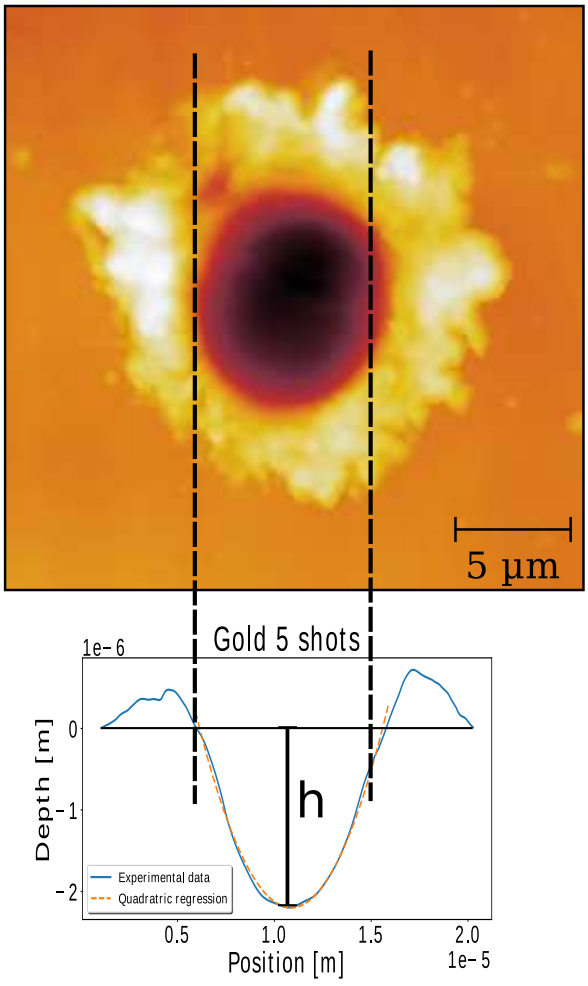

Figure 4.10: Example of the sample analysis and lineout extraction from the micrographs measured.

The ablation depth d, as previously mentioned is described by the logarithm ablation

law and depends on the material fluence ϕ and its fluence threshold ϕ_{th} as follows,

$$d = \frac{1}{\alpha} \ln\left(\frac{\phi}{\phi_{th}}\right) \tag{4.1}$$

As previously described in section 4.2.1.2, the EUV output beam has an annular shape and a set of spherical mirrors were used to shape the beam into a Gaussian focal spot. The intensity distribution for a Gaussian beam with a spatial and temporal profile is usually written as follows [77],

$$I(r,t) = I_0 \exp(\frac{-r^2}{\rho^2}) \exp(\frac{-t^2}{\tau^2}) \tag{4.2}$$

where I_0 is the peak intensity, ρ is the spatial radius, τ is the temporal radius, both at $(1/e)$ of the peak intensity and r and t are the radial coordinate and the time variable respectively. The spatial distribution of the fluence is then obtained integrating the intensity distribution over time. Given the following equation,

$$E(r) = \int_{-\infty}^{\infty} I(r,t)dt = E_0 \exp(\frac{-r^2}{\rho^2}) \tag{4.3}$$

where $E_0 = \sqrt{\pi}\tau I_0$ is the peak fluence at the centre of the beam. Then, combining equations 4.1 and 4.3,the ablation profile results in a parabolic shape and depends on the radial distribution of the fluence as,

$$d(r) = -\frac{1}{\alpha}\left(\frac{r^2}{\rho} + \ln(\phi_{th}) - \ln(E_0)\right) \tag{4.4}$$

4.4.1 Optical

The analysis of the WLI micrographs consists of the analysis of 5 lineouts around the centre of the craters. Figure 4.11 shows an example of the lineouts measured, these lineouts are measured one by one, because of the elliptical shape of the spots the lineouts were measured on the major axis as we are only interested in the ablation depth. The crater shape and the ablation depths were extracted and analysed using the Python script in appendix A.2. Representative micrographs for Al, copper and silicon are shown in figures 4.12, 4.13 and 4.14 for all the fluences analysed. The average value of these profiles determined the depth as function of fluence and also the spatial distribution of the ablation pulses. In this particular case, the manufacturer of the MiniLite II laser specifies a Gaussian distribution of the laser energy. Based on the analysis of the micrographs, the craters spatial distribution can be described using equation 4.4.

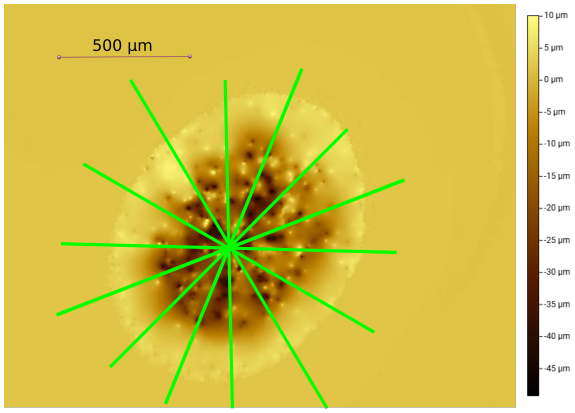

Figure 4.11: Example of the lineouts measured for the samples.

Based on the shape of the laser pulse and the ablation law, it is expected that the craters created had a parabolic shape. To verify if this was the case, the plots of the extracted lineouts were compared to the theoretical crater shape expected. The parameters used for the analytical expressions were obtained from the experimental data using a least square algorithm.

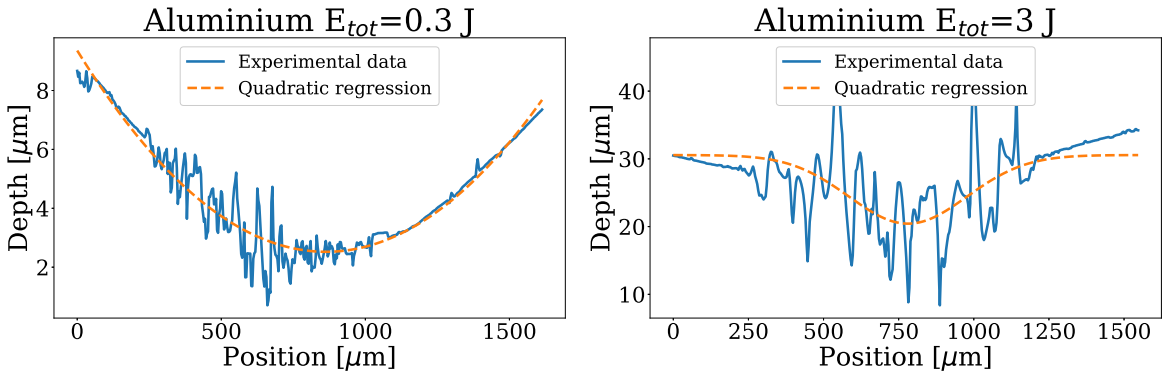

(a)

(b)

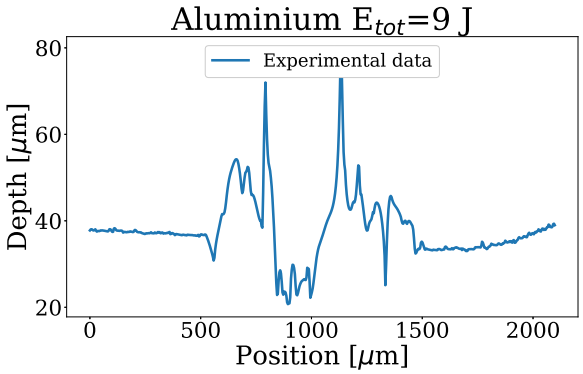

(c)

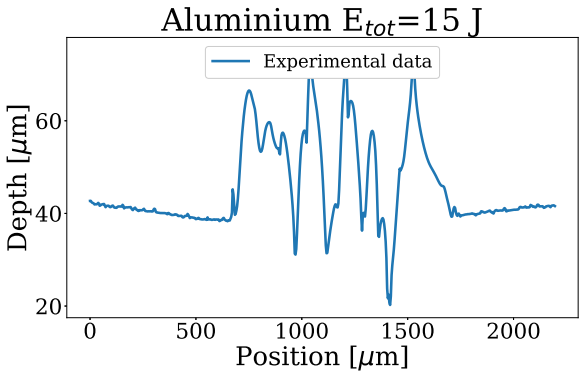

(d)

Figure 4.12: Single ablation profiles for 10, 100, 300, and 500 shots in an Al target using a 532 nm laser beam.

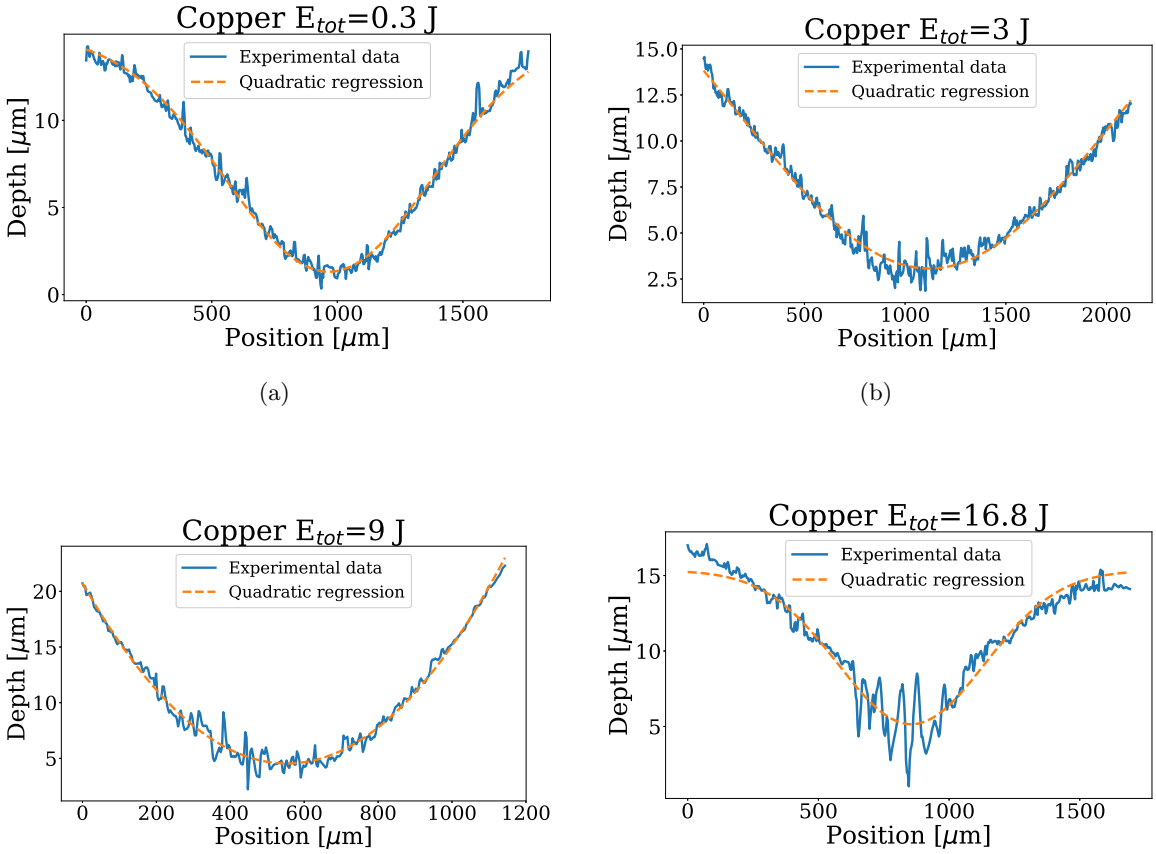

Figure 4.13: Single ablation profiles for 10, 50, 100 and 300 shots in a copper target using a 532 nm laser beam.

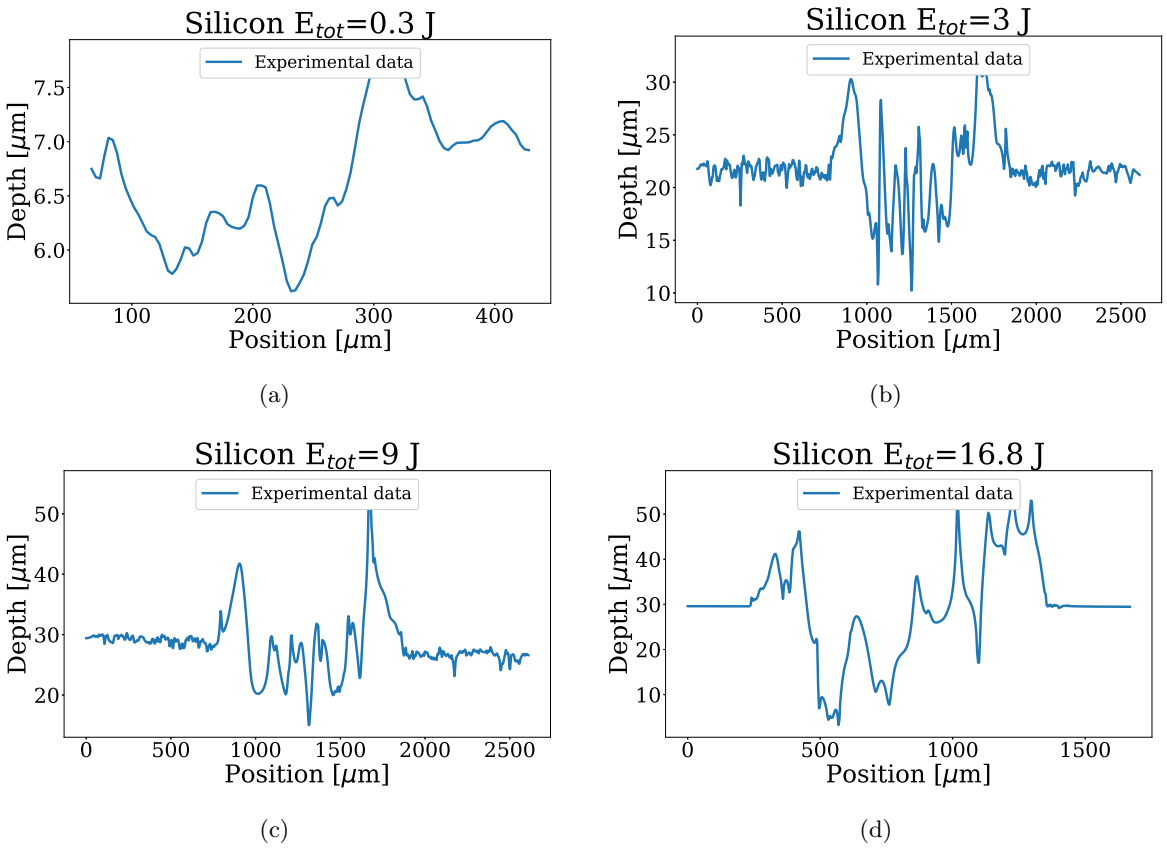

Figure 4.14: Single ablation profiles for 10, 110, 300 and 560 shots in a silicon target using a 532 nm laser beam.

The analysis of the samples and their respectively parabolic fitting was difficult in some samples. As mentioned previously in section 4.3.1, some targets presented peaks in the centre and some amorphous shape. This might be produced by melting and solidification processes during the ablation. In the case of Al samples, these peaks were found inside the crater and made impossible the calculation of the parameters to fit a quadratic function in figures 4.12c and 4.12d due to the profile shape. In the copper samples 4.13a - 4.13d the crater lineouts had a smoother ablation profile and the parabolic fits in all the samples are close to the experimental data. The Si samples shown a highly amorphous shape, while the parabolic trend is visible the fitting process was not possible in order to have sensible analytical expressions.

4.4.2 EUV

The samples ablated using EUV light were analysed using atomic force microscopy to obtain micrographs of the craters created. The samples were ablated following an increasing number of shots row in different sites within the sample surface as presented in figure 4.15. These increasing patterns were shot repetitively in different areas of the samples. Finally, after an

inspection using an optical microscope these craters did not show any significant differences and the final ablated patterns were chosen randomly.

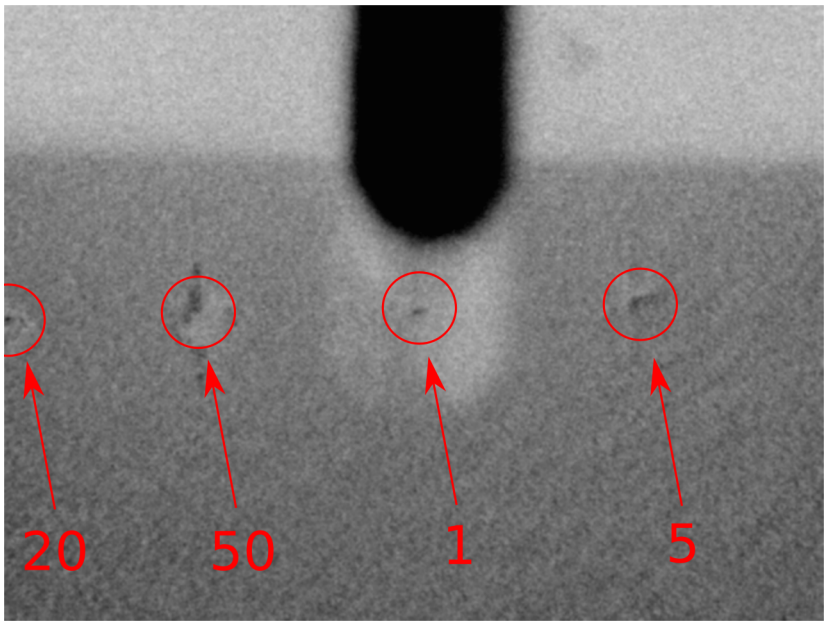

Figure 4.15: Optical microscope view of an ablated Al strip. This picture shows craters created using up to 50 shots. This picture has been processed increasing the contrast and the white balance for a clearer view

The crater shape and depth of all the AFM micrographs were analysed using Gwyddion [78]; an open source program for data visualisation and analysis of scanning probe microscopy (SPM) data files. The ablation profiles obtained for Au, Cu and PMMA are shown in figures 4.17 - 4.19. These profiles are the average of 10 lineouts taken for each sample, this lines were measured using the lineout tool keeping the same length and trying to pass through the centre of the craters. The dataset extracted from these lineouts are processed to calculate the average value of the craters using the Python script shown in the appendix. Figure 4.16 shows the lineouts taken of one of the measured ablation spots.

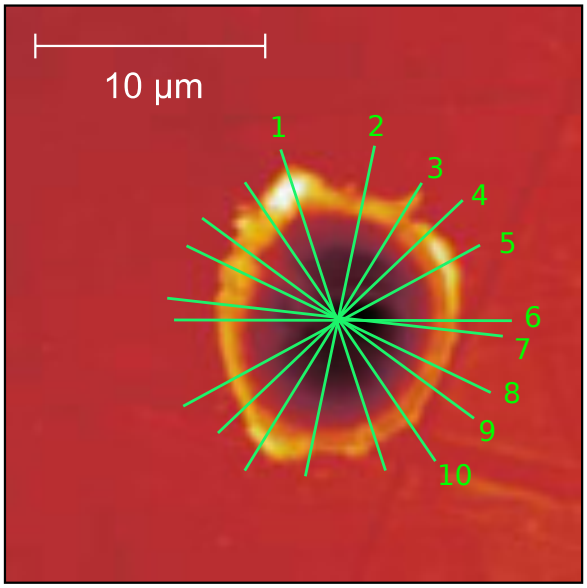

Figure 4.16: Lineouts taken for the measurement of the ablation profiles with Gwyddion in a gold sample.

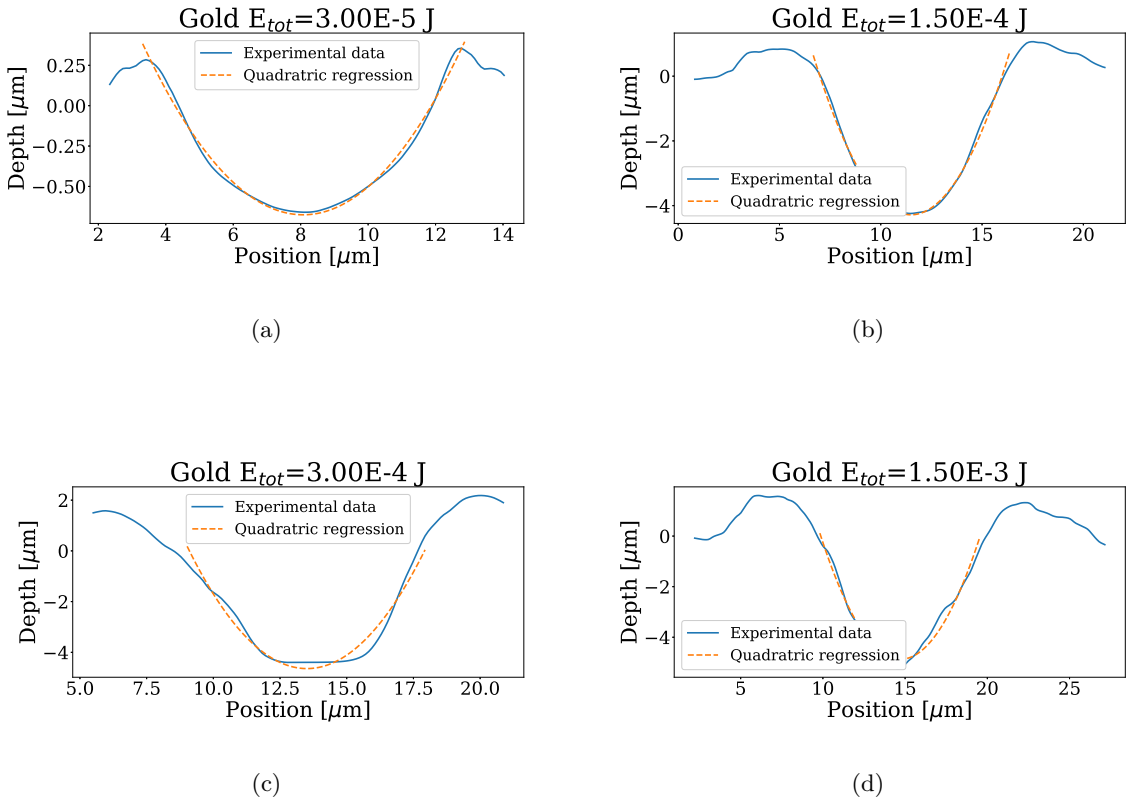

Figure 4.17: Ablation profiles for 1, 10, 20 and 50 shots in a gold target using a 46.9 nm laser beam.

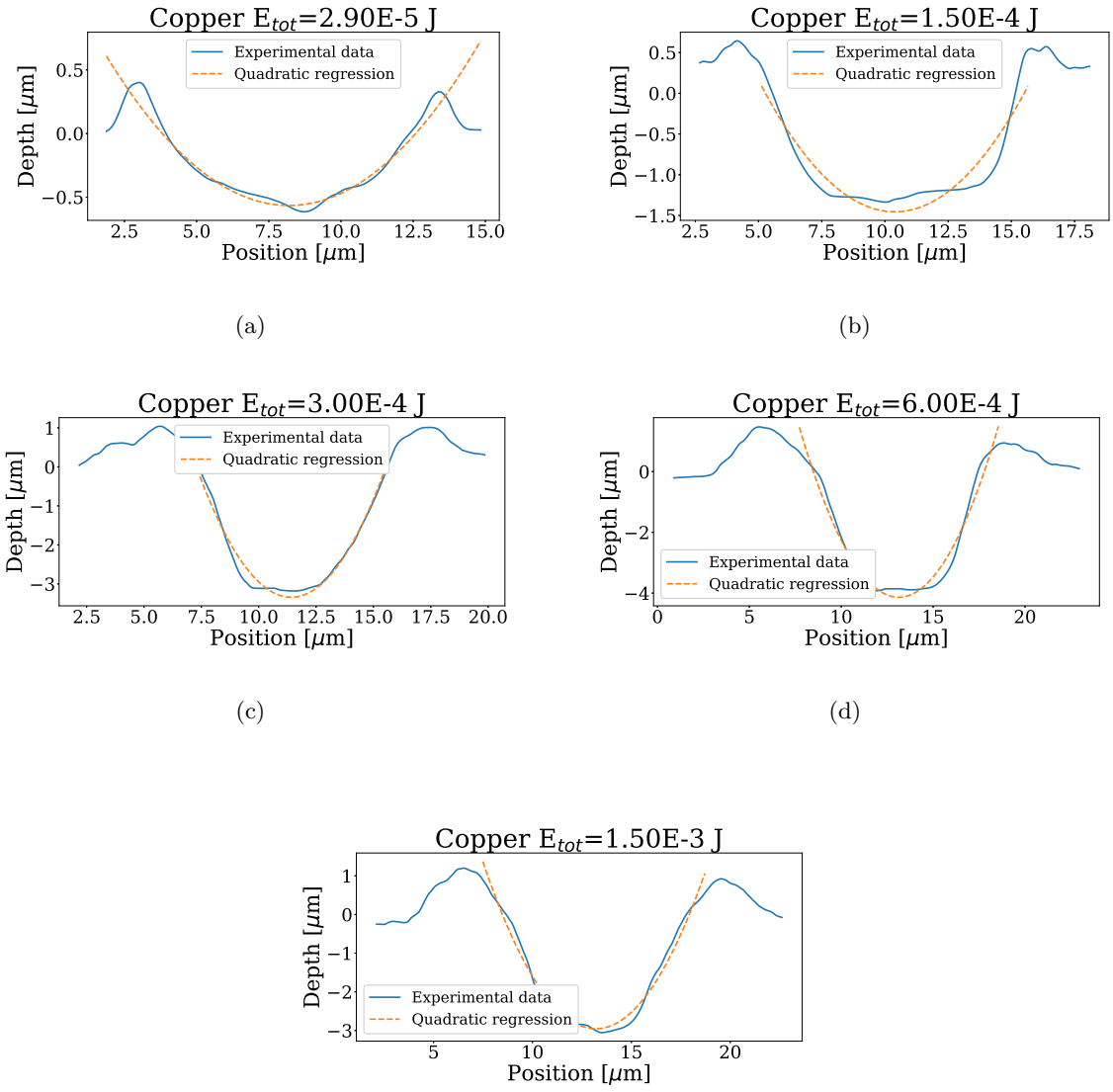

Figure 4.18: Ablation profiles for 1, 5, 10, 20 and 50 shots in a copper target using a 46.9 nm laser beam.

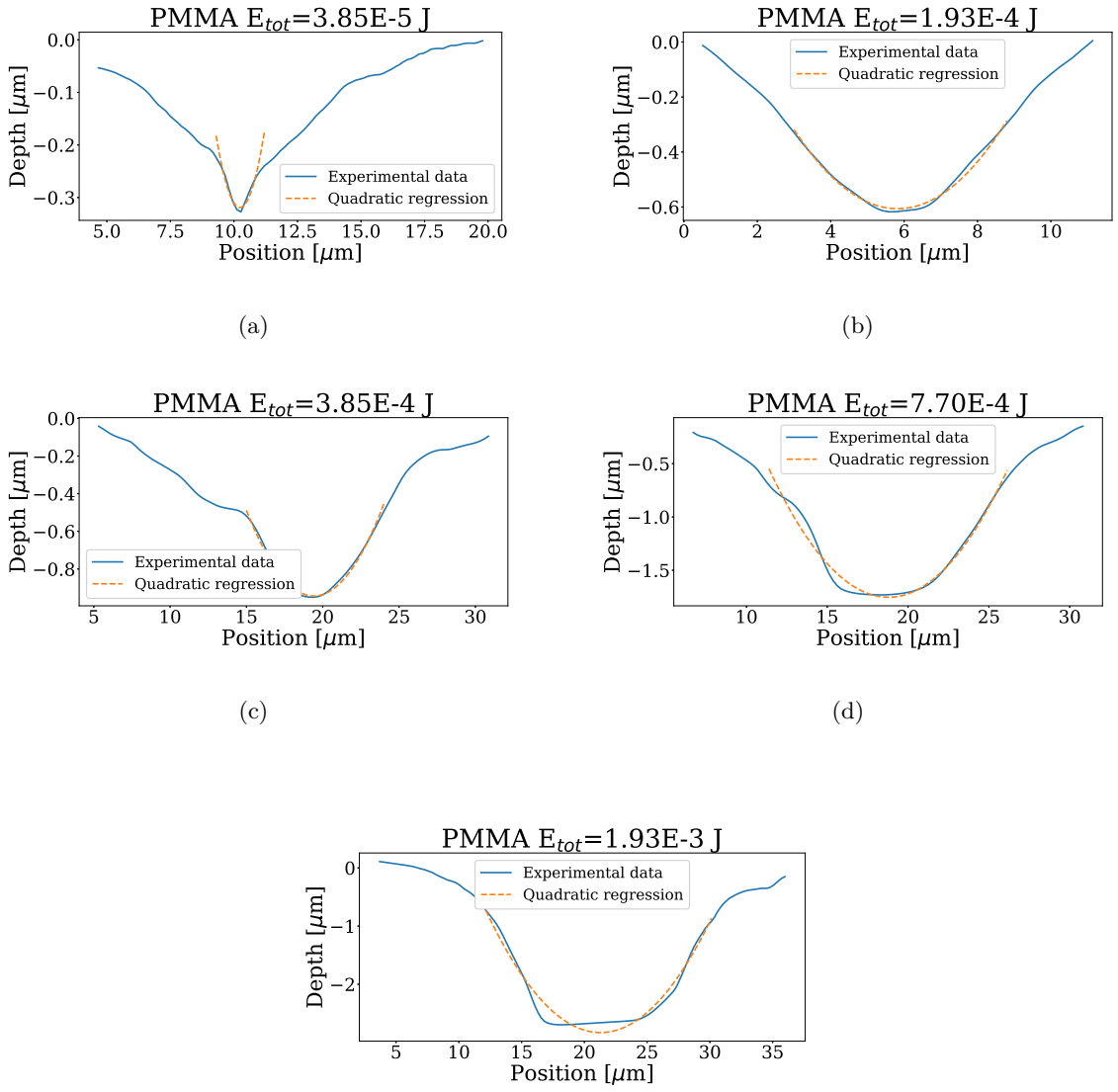

Figure 4.19: Ablation profiles for 1, 5, 10, 20 and 50 shots in a PMMA target using a 46.9 nm laser beam.

These figures show a clearer picture of the profiles of the craters created using EUV radiation. In general all the profiles presented smoother lineouts in comparison to the samples ablated using visible light. However, there is a clear tendency in all the samples to agglomerate piles of material around the crater to a considerable height. It is the case for copper that the average maximum height of these piles is around 1.2 times higher that the crater depth, for Au and PMMA these peaks are smaller but in average they are 50% and 70% of the lowest part in the craters.

The experimental results shown in figures 4.17-4.19 were fitted using quadratic curves, following equation 4.4. In most of the samples analysed there is a significant agreement

between the experimental data and the quadratic fit for Au and Cu. Figure 4.10 shows a representation of the analysis performed on all the samples and the area of interest for the process of comparing the shape of the craters with the ablation model. These materials showed that equation 4.4 still holds in the case of EUV light interaction with matter, i.e. the ablation depth depends logarithmically in the energy fluence distribution. However, in all the craters were found bumps surrounding the crater holes which might be induced by thermal processes melting the material and an eventual solidification in the outermost part of the crater holes. Contrary to the case of PMMA, where the overall shape seems to be vaulted and deformed in most of the samples. According to previous research works, the deformation of the craters in PMMA might be produced by radiation cross-linking of polymer chains which could reduce the ablation rate[79] or the attenuation of the laser beam by gaseous fragments of PMMA [26]. The metallic materials shown smoother and cleaner ablation patterns, also the ablation depths are bigger in comparison to PMMA suggesting different ablation mechanisms that could be related with the attenuation length of the materials.

4.5 Energy deposition

The results shown in the previous sections for each wavelength indicate clearly the difference of shape and cross section as they are observed on all the materials analysed. These gives a first insight for the measurement of the ablation thresholds at different wavelengths. Based on these previous results on the crater shapes, the ablation thresholds should be substantially different as it is expected that the ablation mechanisms change. The amount of material removed and the craters created are also different even if the energy fluences for the experiments are similar.

The micrographs presented in the previous sections for each wavelength show the differences of shape and cross sections in the materials ablated for the different wavelengths. Based on these results it is clear that the effects on the topography of the crater created and the maximum depth depends directly on the laser wavelength used, suggesting that the ablation mechanisms change. The different ablation mechanisms as a function of wavelength have been studied previously and demonstrated that depending on the wavelength the ablation mechanisms are completely different [80]. The type of material is also important in these interactions. Metals and polymers have been shown to have different ablation mechanisms, they could be thermal, thermo-mechanical, photo-chemical, multi-photon or avalanche ionisation processes [81]. Furthermore, the duration of the ablation laser pulse is a very important characteristic to be considered in further theoretical work about the different ablation mechanisms [31].

In this section, different materials were analysed to measure the physical characteristics of the crater drilled with multiple laser shots at 532 and 46.9 nm. The average ablation rate is presented to analyse the material removal for both laser wavelengths. Previous work in this field is also described and compared theoretically and experimentally.

4.5.1 Visible

In this section is presented the analysis of the ablation depth as function of the accumulated energy deposited in the materials for multiple shots. Figures 4.5.1, 4.5.1 and 4.5.1 show the crater depth as function of the total energy density accumulated after several shots in the same spot and the average material removal per shot as the number of shots increases in the same spot.

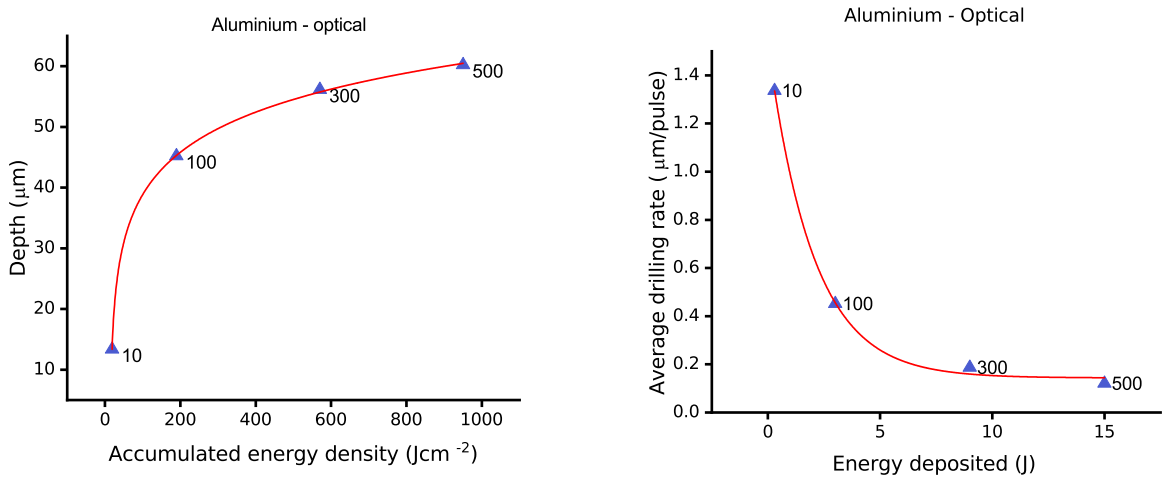

Figure 4.20: Ablation depth vs. accumulated energy (left) and the drilling rate as function of the energy deposited (right) with multiple shots on Al samples ablated with optical radiation at 532 nm.

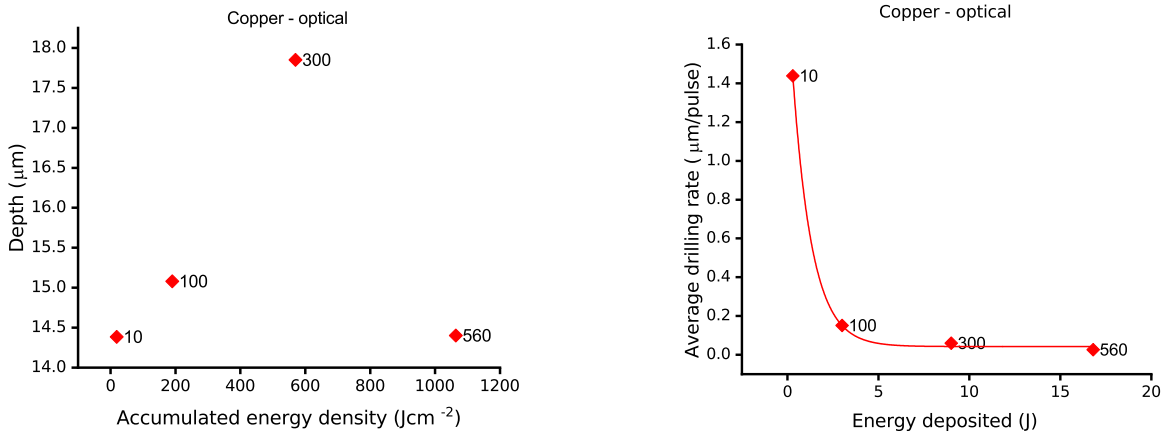

Figure 4.21: Ablation depth vs. accumulated energy (left) and the drilling rate as function of the energy deposited (right) with multiple shots on Cu samples ablated with optical radiation at 532 nm.

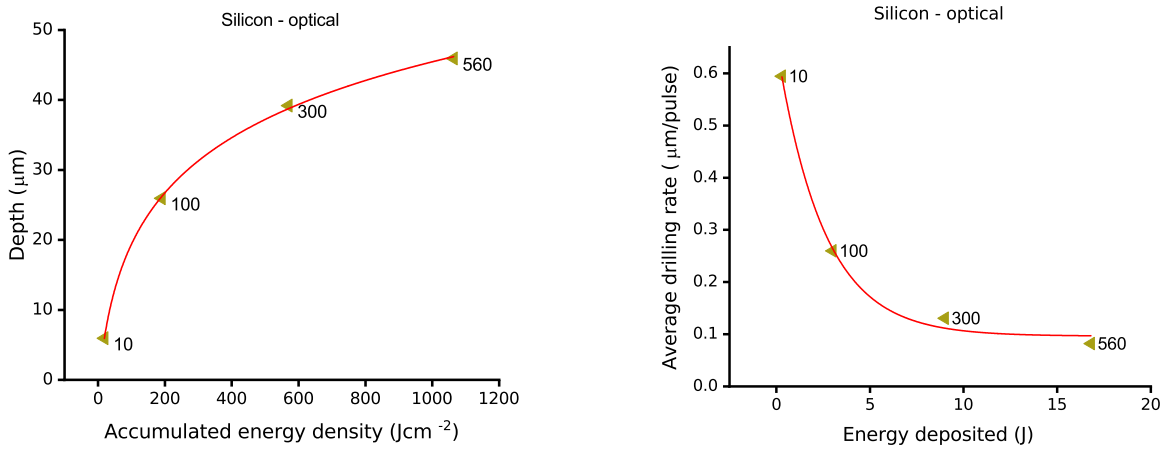

Figure 4.22: Ablation depth vs. accumulated energy (left) and the drilling rate as function of the energy deposited (right) with multiple shots on Si samples ablated with optical radiation at 532 nm.

The analysis shows relevant characteristics about the behaviour of the different materials during the ablation process. The depths of the craters as function of the energy density deposited into the materials show a logarithmic trend, this seems reasonable as the maximum depth of the craters should be limited by the thickness of the materials. None of the samples analysed presented a complete piercing through the material. The average material removal per shot presented an exponential decay as the numbers of shots increased in the same spot. It is clear from these pictures that the ablation efficiency decays as the numbers of shots increases, but it is not in the same rate for all the materials. The copper sample presented an interesting behaviour for 560 shots, the depth of the crater decreased in comparison to 300 shots. Cu has the shortest attenuation length meaning that the laser energy is deposited in the smallest volume. This might cause that the thermal effects such as melting occur more easy and the material resolidificates faster. Overall, it seems that the ablation depth for visible light follow the expected trends with energy deposition density, i.e. energy per volume, a key parameter, together with the amount of energy required to cause a phase change in the solid target. The error associated in this analysis is very difficult to estimate as a lot of parameters are important during the ablation processes such as the laser intensity, pulse length and spot size. Based on previous works, this analysis shows the material removal trend for a high number of shots in the same spot in comparison to previous works were they show a linear trend for a limited variation of shots.

4.5.2 EUV

The measurement of each maximum depth from figures 4.17-4.19 are summarised in figures 4.5.2, 4.5.2 and 4.5.2, as a function of accumulated energy density and accumulated energy. These figures shows also the behaviour of the materials as the number of shots increases and how the material removal changes.

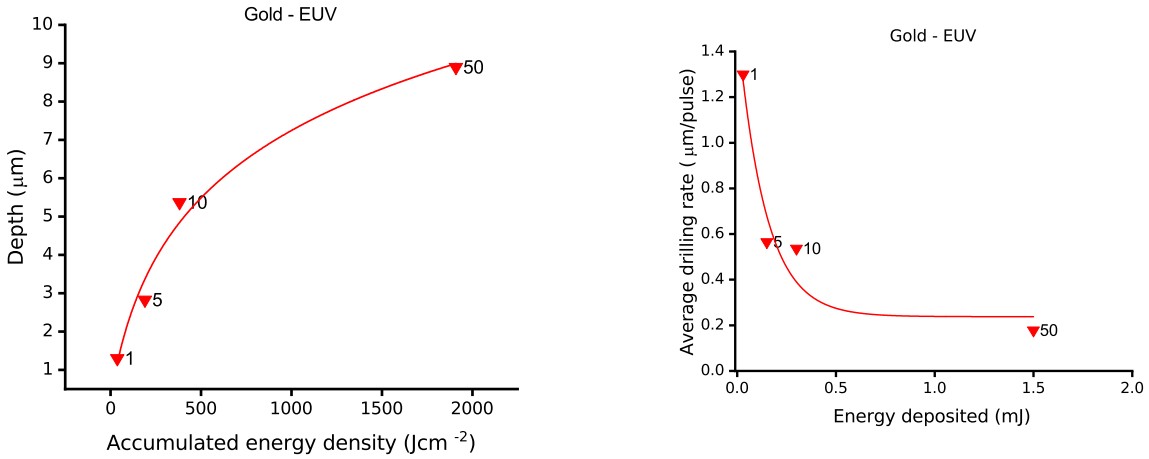

Figure 4.23: Ablation depth vs. accumulated energy (left) and the drilling rate as function of the energy deposited (right) with multiple shots on Au samples ablated with EUV radiation at 46.9 nm.

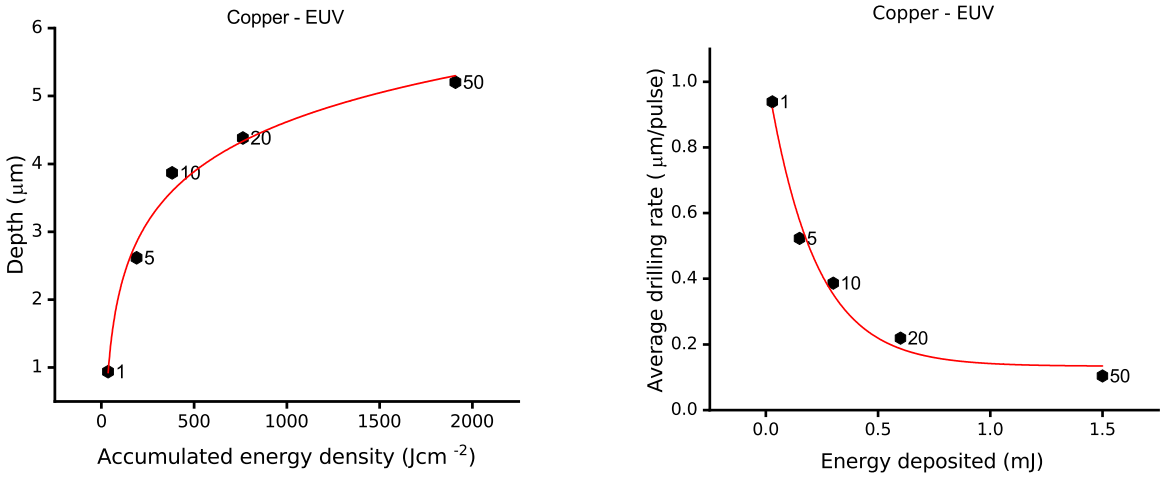

Figure 4.24: Ablation depth vs. accumulated energy (left) and the drilling rate as function of the energy deposited (right) with multiple shots on Cu samples ablated with EUV radiation at 46.9 nm.

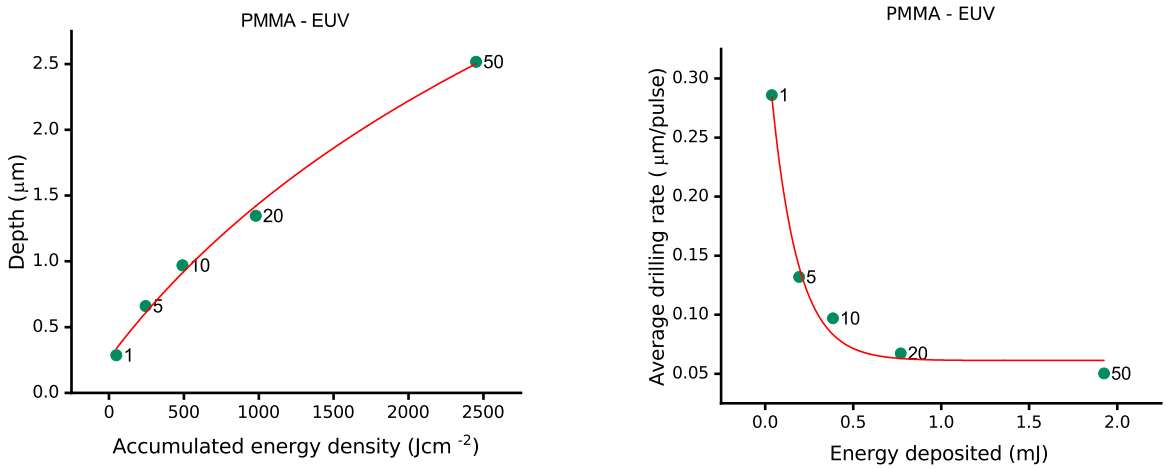

Figure 4.25: Ablation depth vs. accumulated energy (left) and the drilling rate as function of the energy deposited (right) with multiple shots on PMMA samples ablated with EUV radiation at 46.9 nm.

Because of the relatively difficult access to laser sources in the EUV range most of the literature on this topic is mainly developed in free-electron lasers. Based on the laser parameters, especially the wavelength and the pulse time and the materials used this is a unique experimental work. Overall, the ablation profiles are similar to what was observed for visible light. The energy density is similar for both cases because of the tight focus of the EUV lases, but the energy deposited into the materials is 3 orders of magnitude lower than the visible laser case. This EUV ablation results more efficient for material ablation with a smaller number of shots. The extrapolation of the ablation depth as function of the number of shots into the materials seems to have and asymptotic behaviour as in the optical case. However, it might be the case that the local dose is below the actual ablation regime and it is located in the desorption regime. This phenomenon is described by Chalupský *et al.* [82] and there is a steep gradient in the removal of material when the local dose is above certain limit.

Figure 4.26 shows the craters depth as function of the number of shots, the extrapolations for EUV show that the number of shots is rapidly convergent to maximum depth. The thickness of the materials are far from the maximum depth achieved, this suggest that the dominant regime is desorption rather than ablation on the samples. These better qualities in the crater were important during the analysis, these allowed to find the average crater depths and decreased the standard deviation from the average value. In general, the quality of the topography of the samples is notoriously better as they have a smoother surface and the resolidification of material decreases.

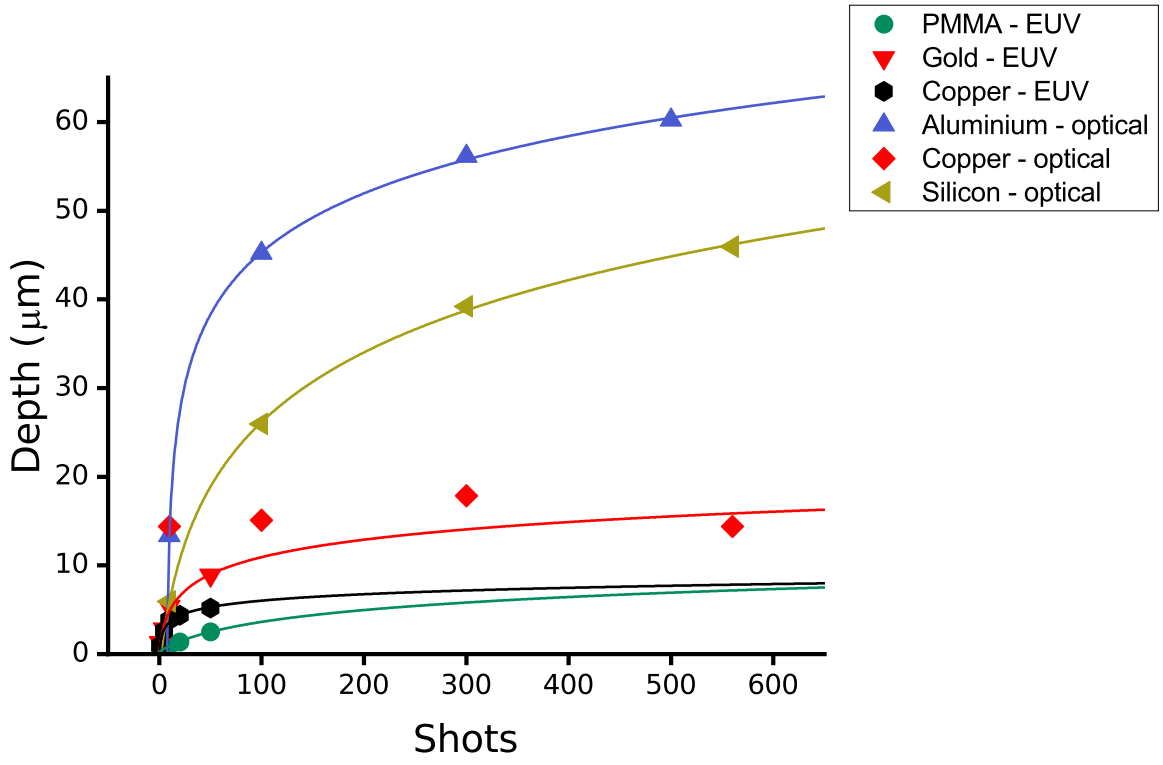

Figure 4.26:

This indicates that non-thermal ablation is dominant during this process even if the laser pulse duration is in the nanoseconds region. As previously mentioned, Chalupský *et al.* indicated that direct photo-etching occurs for energetic photons and this might be the dominant process during the material removal. This is different from the inverse bremsstrahlung absorption that is observed for visible light. One final comment can be made on the ablation of PMMA. The ablation rate decreases considerably in comparison to the other materials. This is significantly lower than what could be expected based on the attenuation length and latent heat. This anomaly might indicates that for organic polymers ablated at this wavelengths might coexist additional processes such as radiation induced cross-linking and chain scission, previously described for several authors in the same laser regime but at shorter pulses duration [72][82][83].

4.6 Beam reconstruction based on the experimental data

Based on the AFM and WLI micrographs, the energy spatial distribution of the laser pulses can be reconstructed using the lineouts measured and the coefficients of the polynomial fits. Liu's method [77] for beam reconstruction has been widely use for different laser wavelengths and proved to be reliable if the material ablated responds linearly to the incoming radiation energy and if the pulse is strongly localised in an area, which seems to be the case for EUV

radiation according to Chalupský *et al.[72]*

Equation 4.3 describes the energy spatial distribution of a Gaussian beam using the spatial radius and the peak energy E_0, where $E_0 = \sqrt{\pi}\tau I_0$ and τ is the pulse width of the laser pulse.

Using the fitting parameters of a Au sample ablated with EUV radiation, which are parabolic we obtained an analytical description of a Gaussian beam and the example is shown in figure 4.27

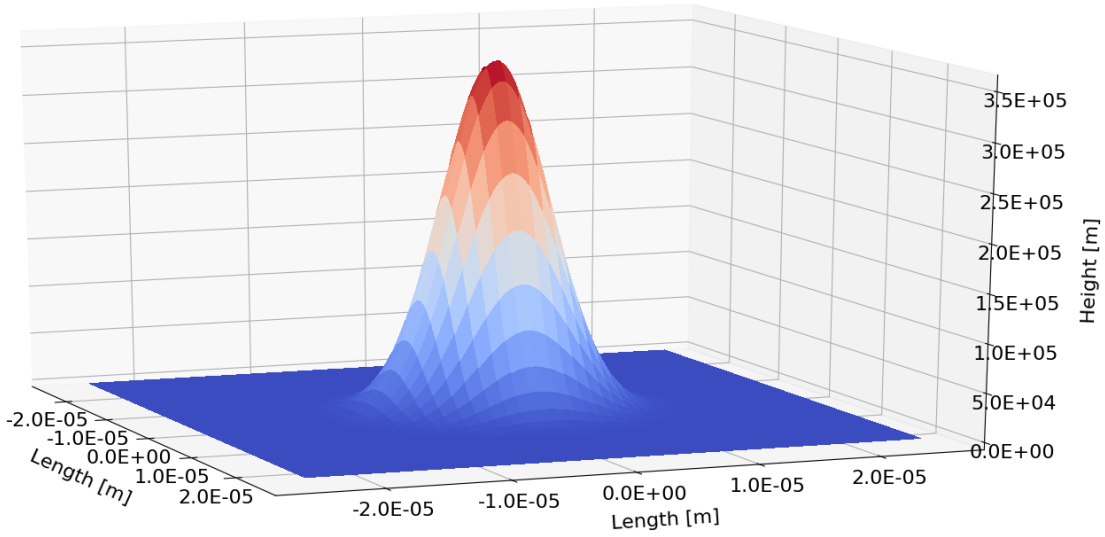

Figure 4.27: Reconstruction of the Gaussian beam used for the ablation of gold based on the ablation craters profiles.

In the case of the EUV laser source, the output beam has an annular shape and it is transformed into a Gaussian beam using a zone plate. In order to confirm that the pulse becomes Gaussian, this type of analysis was the best solution and based on the evidence of the parabolic lineouts extracted from all the samples, we can confirm that the pulses interacting with the samples are transformed effectively into Gaussian beams.

4.7 Conclusions

In this chapter we presented the experimental results and the analysis of the ablation of samples using two different laser sources at 532 and 46.9 nm. The results obtained gave a first insight of the ablation thresholds and crater characteristics using materials with different attenuation lengths. The laser intensities in both experiments are similar and the materials used have attenuation lengths also in the same order of magnitude to make the experiments comparable. The ablation quality of the samples was clearly better using EUV radiation as shown in figures 4.17-4.19 for EUV light, in comparison with the samples ablated using visible light shown in figures 4.4-4.6. Qualitatively, the EUV samples showed a smooth and

clear ablation spot and the AFM analysis did not show many sighs of re-solidification inside the crater but the rims created around the ablation spots shows evidence of a phenomenon named “piston” effect that occurs when the laser pulse duration is long enough and the lateral pressure of the laser is significant in comparison to the normal pressure. The samples ablated with visible light and analysed using white light interferometry showed a worst quality in the crater ablation. These craters have columns that could be an indication of thermal processes that do not occur during the ablation of samples using EUV radiation. Also, the shapes of the craters were compared with the expected theoretical shape based on the ablation laws. In both cases, the materials were ablated using Gaussian pulses and the created craters have a parabolic shape. This holds for both cases independently of the wavelength. Furthermore, based on the evidence of the parabolic shape for EUV a reconstruction of the laser shape was computed to understand its spatial energy distribution.

The material removal showed differences in the amount of material removed in comparison to the number of shots, there is a better efficiency for removal of material using EUV light. It seems that the ablation process for EUV is still located in the desorption regime, however the material removal as function of energy deposited shows a better performance. In both cases the ablation rate or drilling rate had an asymptotic behaviour. Finally, the experiments also showed a different ablation behaviour for the compound material PMMA, suggesting the importance of additional processes such as cross-linking and molecular fragmentation in these types of materials. Further investigations are needed to clarify the role of these processes in the overall ablation process.

Chapter 5

Extreme Ultraviolet Time-of-flight Mass Spectrometry

Laser ablation mass spectrometry (LA-MS) has been widely used as a reliable technique for the analysis of elemental composition of samples from diverse fields such as chemistry, biology and nuclear physics. This technique can be described as two independent tools that work together to analyse materials; a part of the system uses a laser to ablate a small part of the sample, inserting sample ions into the second part of the system, which analyses the masses of the sample ions. Traditionally, conventional lasers in the visible spectrum are used as ablation sources. In this regard, the laser source wavelength is proportional to the minimum ablation spot size achievable. In many cases, removing as little material as possible from the sample is critical, e.g. for biological or high-value samples.

Reducing the laser wavelength in laser sources for LA-MS is an evident solution to overcome this problem. However, the reduction in size and power consumption for laser sources at lower wavelengths has not evolved as fast as other components in mass spectrometers, meaning that VUV/EUV LA-MS is still a challenge. Nevertheless, table-top sources in the extreme ultraviolet (EUV) range have been developed over the last decades providing a reliable and high repetition source of radiation in the nanometer range. The incorporation of this type of laser in a mass spectrometer, has recently been shown at Colorado State University. Specifically, this device uses a capillary discharge Ne-like Ar laser [84], also described in section 2.1.2, which produces pulses of 10 μJ and 1.5 ns duration at 46.9 nm. It works together with a Time-of-flight (TOF) mass spectrometer. The reliability and high resolution of this device has been demonstrated in the analysis of well-characterized standard glasses using submicron ablation spots, where the results obtained were comparable with the analysis of the same material using a commercially available TOF secondary ion mass spectrometer (TOF SIMS)[85] . Furthermore, this new EUV TOF technique has shown it is capable of creating a 3D map of the chemical composition of different materials due to its submicron ablation spots [86].

In this chapter, the possibility of using EUV TOF as a plasma diagnostic are explored. In

particular, whether the measured mass spectrum can give information about the EUV-laser-produced plasma. If the expanding plasma plume is assumed to be in a coronal ionisation equilibrium, the temperature of the plume can be estimated from the measured distribution of ions. This would provide a non-perturbative technique to measure plasma temperature within the EUV TOF diagnostic without the need for further diagnostic equipment.

5.1 TOF MS: System overview

The experiments were carried out at the Colorado State University within the facilities provided by the Engineering Research Center for Extreme Ultraviolet Science and Technology. Their extreme ultraviolet time-of-flight mass spectrometer was used to analyse different materials. This device is unique due to the capillary discharge laser source used, its main parameters are described in table 5.1.

Table 5.1: Laser parameters of the laser used in the experiments

Laser parameters	
Wavelength:	46.9 nm
Energy output:	10-20 μJ
Pulse length:	1.2 ns
Spot size:	5 μm
Fluence:	100 Jcm^{-}2

This type of laser radiation offers advantages over its longer wavelength counterparts. For instance, this wavelength allows the beam to be focused down to 80 nm in diameter, in comparison to $\sim 0.25\,\mu$m for 532 nm. It also has a attenuation length of typically a few tens of nanometres, while for 532 nm the attenuation length can be as high tens of microns [87], for this reason the laser energy is deposited in a shallow volume when EUV radiation is used. The energy per photon is 26.4 eV compared to 1-3 eV for visible light, this high photon energy ionise the material very efficiently allowing soft ionisation by single photon ionisation, a feature especially important for biological analysis.

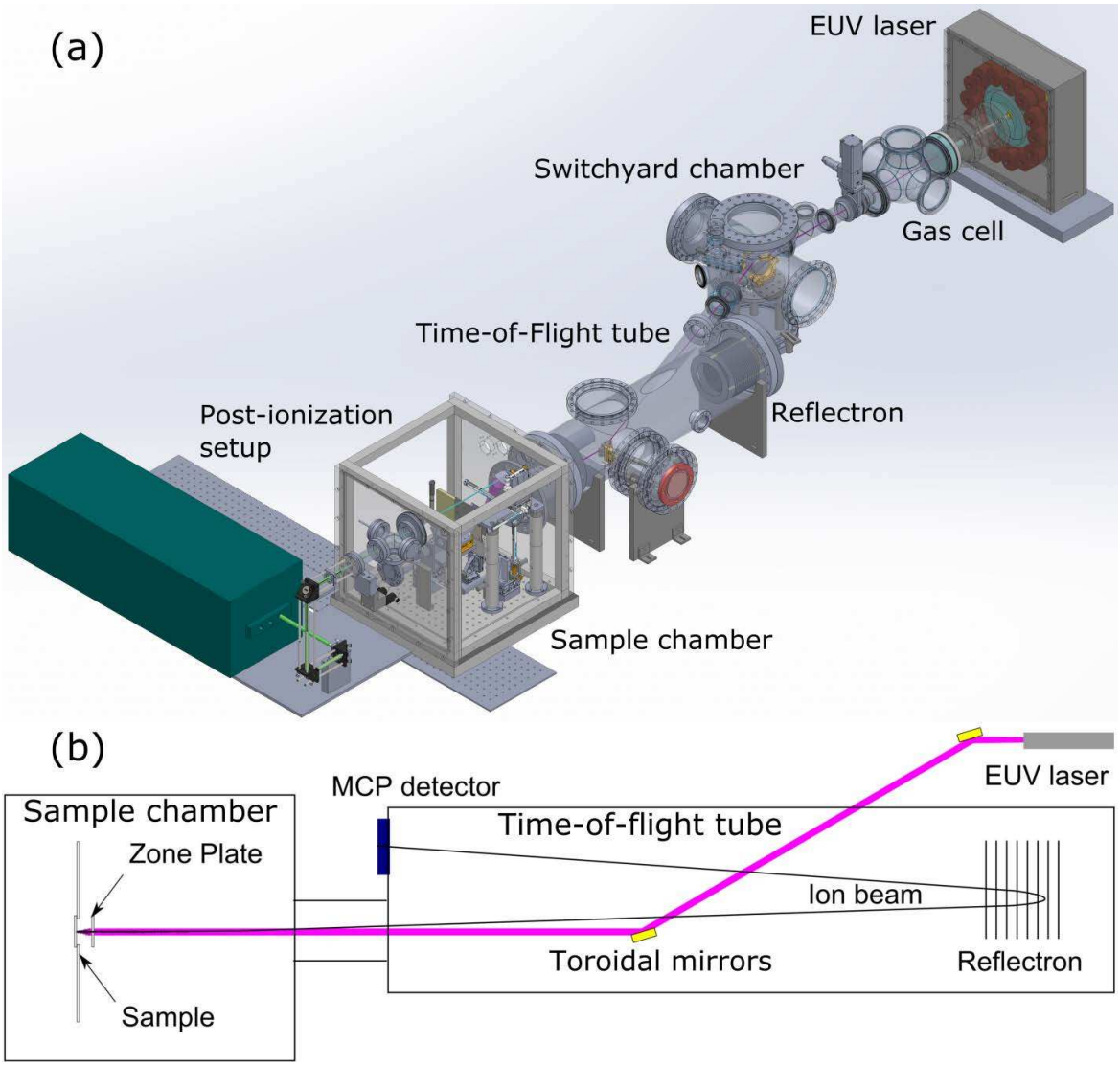

Figure 5.1: a) 3D CAD view of the complete EUV Time-of-Flight Mass Spectrometer. b) Schematic diagram of the laser and ion paths within the TOF MS device.

In figure 5.1 a 3D CAD design shows the mass spectrometer design. Roughly the general functioning of the device starts with the laser beam output travelling into the gas cell chamber where a flow of argon is used to attenuate the laser energy, if required, the beam is then guided into the interaction chamber using a set of two toroidal mirrors. The beam illuminates a zone plate right before the interaction chamber, this zone plate has a central opening that focuses the EUV beam into a Gaussian beam to ablate the target/sample. The sample is mounted in a holder with a bias that creates a potential with a grounded grid mounted next to the zone plate. This potential extracts and accelerates the ions which come through the central opening in the zone plate to enter into the Time-of-flight drift tube, also known as flying tube. Once in the flying tube the ions follow an elliptical or linear trajectory depending if the machine is used in reflectron mode or not. Finally the ions hit a microchannel plate

(MCP) that collects the ions and measure the time of flight in an automated way using LabVIEW®.

5.1.1 Laser setup

The mass spectrometer uses a capillary discharge laser, using an Ne-like Ar single pass gain medium. To create the lasing process, Ar gas flows at 400 mbar inside a 21 cm long alumina capillary, where a low-density glow discharge is produced using RF power. Subsequently, a high-voltage, high-current pulse at 90 kV and 22 kA, is sent through the capillary, creating a pinch discharge with a high density and temperature, capable of sustaining the EUV lasing process. Further details can be found in section 2.1.2.1, this produces a beam with a high divergence. This laser is operated at a repetition rate of 1 Hz, mainly for acquisition reasons. The discharge process is diagnosed using a Rogowski coil surrounding the capillary tube, whichs serves also as a triggering system since the discharge current and the light emission are offset by ∼120 ns.

5.1.1.1 Laser optics

As explained in section 2.1.2, the plasma created inside the capillary tube has a refractive index gradient which causes that the amplified rays tend to deflect to the sides forming an annular beam profile. In figure 5.2 is shown the profile of the annular beam used during the ablation experiments. The beam profile was measured using a gold detector located in a motorised stage, this image has a resolution of 20×20 pixels. The laser is collimated and focused using a set of non-conventional refractive optics due to the high absorption at this wavelength in normal mirrors.

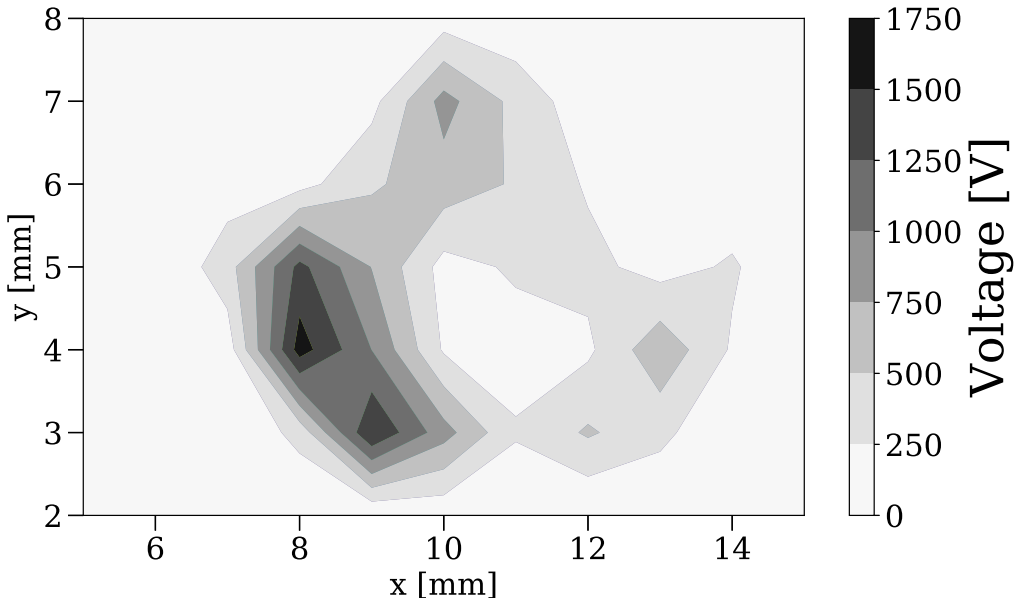

Figure 5.2: Intensity profile of the laser beam measured at the zone plate position inside the sample chamber. The profile has an annular shape with approximately 5 mm outer and 2 mm inner diameters.

A set of two toroidal mirrors collimate and guide the beam into the zone plate. This type of mirrors has the advantage over spherical, ellipsoidal or parabolic mirrors to reduce the astigmatism produced at small incident angles which is the case in this set-up. It is important to mention that because of the high divergence of the beam and the relatively long light-path (3 m) which would cause that the initial annular profile would spread out up to 15 mm at the zone plate (ZP). For this reason, the collimating mirrors are needed so that the zone plate is illuminated by a 3mm diameter EUV beam. The zone plate then focuses the EUV laser onto the sample to a spot of about (5.0 ± 0.5) µm, a relatively large focal spot was chosen for these experiments to maximise the signal for this novel method.

The zone plate was made by electron beam lithography in a 100 nm thick silicon membrane and both sides were covered with gold. Figure 5.3 shows and idealisation of the zone plate used, the centre of the ZP has a 0.5 mm opening that allows the ions to come into the TOF tube. The alternate pattern of opaque and transparent concentric rings decreases in width down to ∼200 nm on the edge. This outer zone width defines the focal length, numerical aperture and the focal spot diameter of the zone plate at the laser illumination. The overall efficiency is 10% at the first order and the smallest ablation volume in this configuration is in the 3$^{\text{rd}}$ diffraction order.

Table 5.2: Attenuation length of the materials ablated.

	Attenuation length
Au	5.98×10^{-9} m
Ag	6.97×10^{-9} m
Si	230.16×10^{-9} m
Al	40.80×10^{-9} m

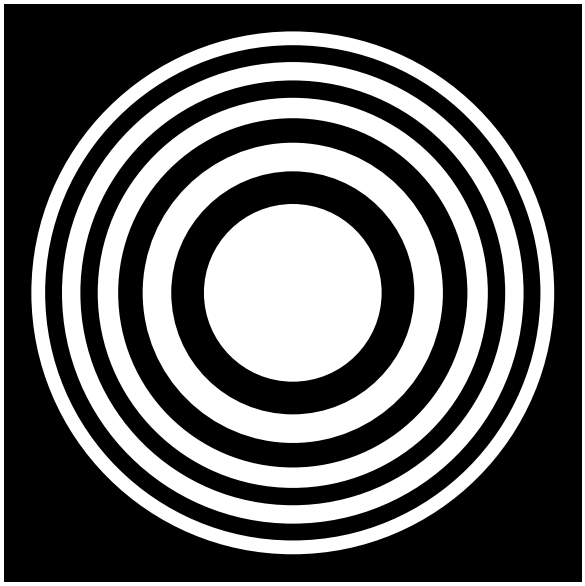

Figure 5.3: Idealisation of a Fresnel zone plate used in the experimental device

5.1.2 Targets

All the samples analysed were chosen in order to cover different attenuation lengths for EUV light. Au and Ag have an attenuation length in the order of magnitude of 10^{-9} m, while Al and Si have an attenuation length in the order of 10^{-6} m. The different ranges of attenuation lengths means the volume in which the laser energy is deposited will be different, leading to different plasma properties. The attenuation length information was obtained from the dataset provided by Henke *et al.* [88] and they are shown in table 5.2.

The samples are physically located in the target chamber in a motorised stage that allows a precise focusing. The holder is biased up to 6,000 V, while a grid near the zone plate is grounded to extract the ions into the TOF tube.

5.1.3 Baseline correction

During the data acquisition process, the MCP collects ions travelling in the TOF and arriving at different times because of their m/z ratio. Noise in the detection system will cause a

baseline (or offset) in the MS data [89], which needs to be corrected for in the analysis. The response of the MCP is assumed to be linear; an absolute calibration is not available.

This baseline correction algorithm is called a Whittaker smoother and it is a modified version made by Eilers in 2003 [90] for baseline corrections in chemistry applications. The general idea of this algorithm is that given a series y that might be noisy, but with a length of m points, sampled at equal distances. This last requirement is met in most of the experiments because the sampling rate is at a fixed frequency. For the given series y, we want to fit a smooth series z. However, we need to find the balance between two incompatible goals: first, try to keep the data accuracy and secondly, reduce the roughness of z.

These two conditions could be achieved using the penalised least square regression method,

$$S = \sum_i (y_i - z_i)^2 + \lambda \sum_i (\Delta^2 z_i)^2 \tag{5.1}$$

where Δ^2 is defined as, $\Delta^2 z_i = (z_i - z_{i-1}) - (z_{i-1} - z_{i-2}) = z_i - 2z_{i-1} + z_{1-2}$. Where the first terms in S measures the fit to the data, and the second term corrects or penalises the roughness behaviour of z, and λ balances the two terms. A generalisation of this equation S is given including a vector w of weights. This weighting allows to prioritise data that you know is more accurate than other data,

$$S = \sum_i w_i (y_i - z_i)^2 + \lambda \sum_i (\Delta^2 z_i)^2 \tag{5.2}$$

This leads to a set of equations, as follows

$$(W + \lambda D^{'} D)z = Wy \tag{5.3}$$

with $W = diag(w)$ and D is the difference matrix $Dz = \Delta^2 z$, these are the system of equations that need to be solved.

The most important advantage of this method is that it can be implemented very easily with a few line codes in any modern programming language. As can be seen from eq. 5.3, this method does require user-defined inputs. Compared to a fully automated fitting procedure, this method provides better accuracy of the baseline fit, but of course does introduce a human judgement.The baseline correction in this experiments were performed using Python3 and the code written can be found in Appendix A.1. An example of the effectiveness of the correction is shown in figure 5.4 for a low energy test shot where at low m/z ratios the baseline offset is higher.

Figure 5.4 shows the comparison using the proposed method and a traditional polynomial baseline correction. Figure 5.4 a) shows at the initial masses that the polynomial fit in comparison with the Matrix method differs substantially, but as the mass number increases, this difference is reduced. Quantitatively, the ion peaks ratio using the polynomial correction for Au, Ag, Al and Si differ with respect to the matrix correction between 5 % to 24%. These

differences show how the matrix correction method improve the data analysis. The final mass spectra used for the analysis after the correction are shown in figures 5.5a to 5.5d.

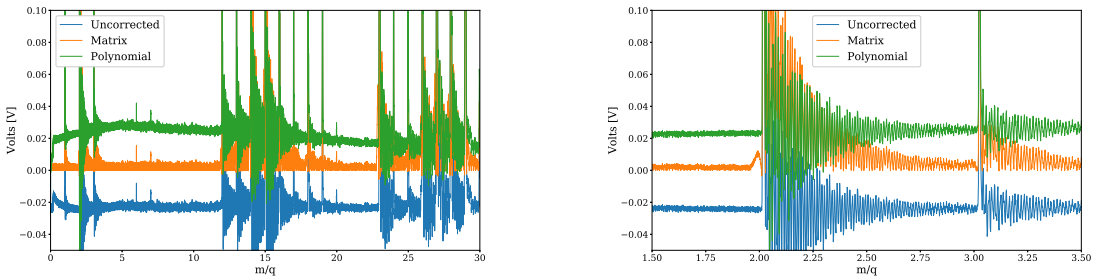

(a) (b)

Figure 5.4: Mass spectra showing the correction of the baseline algorithms. a) shows a complete view of an uncorrected mass spectra and the different correction algorithms. b) presents zoomed in version of figure a), 1.5 to 3.5 m/q, to show clearly the different correction algorithms.

Figure 5.5a) shows the Ag results with double peaks for 2 isotopes of Ag, 107 and 109. The singly charged ions are at m/z of 107 and 109 respectively. In addition, the doubly charged ions can be seen at 53.5 and 54.5. For Al in 5.5b), there is a clear peak for Al+ at 27. For Au in figure 5.5c), 3 ionisation stages can be identified at 197, 98.5 and 65.6. Finally, for Si in 5.5d), the 3 isotopes of the singly charged ion can be seen at 28, 29 and 30. Doubly charged ions for Al and Si are obscured by hydrocarbon contamination. This type of contamination occurs when a sample has a long period in an open environment due to all the air pollutants produced by fossil fuels.

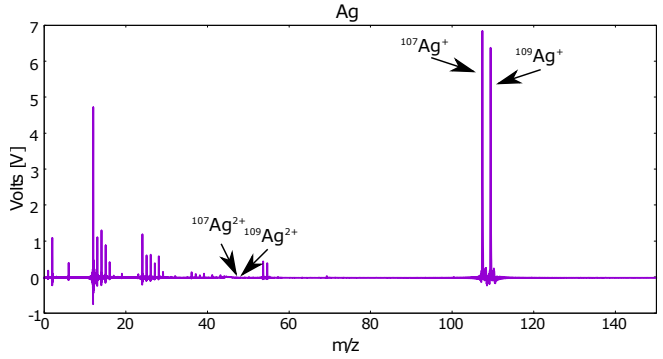

(a)

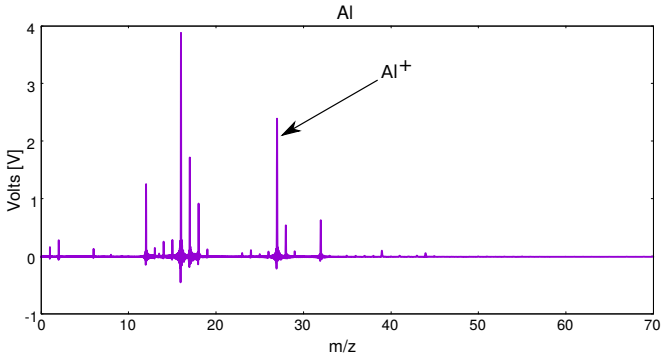

(b)

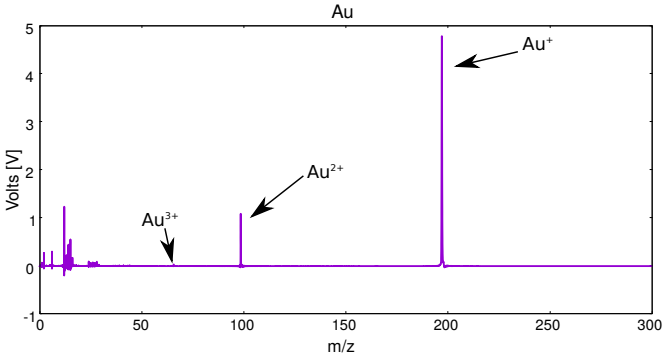

(c)

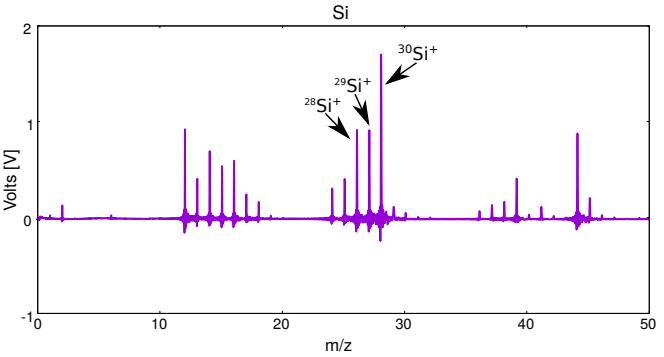

(d)

Figure 5.5: Mass spectra corrected and filtered for the materials ablated.

5.2 Temperature calculations

Mass spectrometry is primarily used for the elemental identification, especially of trace elements. However, in this work the focus is on investigating the possibility of extracting further information about the plasma plume from the mass spectra. For this reason, simple, single element samples were chosen. As expected, the spectra in figure 5.5 show the sample ions, mainly singly ionised, with some doubly ionised and even 3+ for Au. The rest of this chapter focuses on a method to calculate a plasma temperature from the mass spectra.

Based on the results obtained from all the mass spectra and using equation 2.34 we can calculate the effective plasma temperature. The mass spectra shows the peaks corresponding to the different ionisation levels. In order to obtain the ionisation ratio, the area underneath those peaks are calculated and used as an input for equation 2.34. The coronal model equation is a Lambert's transcendental equation and needs to be solved using Lambert-W inverse function. The ratio of the ions experimentally measured in the TOF MS device show that the plasma is heavily dominated by 1^+ ions. In addition, because the lower ionisation state Z_i is a slowly varying function of temperature and 1^+ is the dominant state, so we assume $Z_i = 1$. Subsequently, the experimental ion ratios were used to calculate the plasma temperature. Table 5.3 shows the calculated plasma temperatures with this equation. The accuracy of the temperature values can be estimated as ∼5% based on an error of up to 20% in the ionization ratio determined from the mass spectra.

Table 5.3: Temperature calculation of the plasma plumes.

Material	n_2/n_1	Temperature (eV)
Ag	0.05	1.84
Al	0.02	1.47
Au	0.24	1.72
Si	0.20	1.35

Recalling the initial objective of these experiments; use the TOF device as a new technique to measure the plasma temperature during the ablation process. The issue with this is that the ions measured by the TOF MS device arrive are from different parts of the ablation plume, which will be at different temperatures. This means that taking time-integrated TOF measurements will give an "effective temperature" of the plasma plume, a convolution of ions entering the TOF device with different temperatures. This can be a useful parameter for process control or comparative studies and parameter variations within the same experiment, but it is of somewhat limited value for understanding the physics of the ablation plume.

As previously mentioned these temperatures seem reasonable as they were expected given the laser parameters. Nevertheless, the question is whether we can learn more about the

spatial and temporal distribution of the plasma plume from the measured mass spectra. Of course, there are some assumptions to take into consideration, any ion or electron inside the Debye length does not feel any external radiation. Therefore, an adiabatic expansion model should be able to provide a decent description of the expansion process, including intrinsic parameters such as temperature, pressue and density.

5.2.1 Modelling results

Section 2.3 presents the equations of the adiabatic expansion model that describe the plasma plume evolution over time after the laser interaction with the material surface. These equations are solved numerically using python and the results describe the temporal and spatial evolution of the plasma density, temperature and pressure. From these three plasma parameters and the assumption of a coronal equilibrium, the number of ions entering the TOF MS device can be calculated, i.e. the flux of ions and the ionisation states.

As well as the general applicability of the adiabatic expansion model, the applicability of two different initial conditions for the model, an isoentropic and an isothermal condition, are investigated. Both have been successful in literature to match experimental ablation experiments. Agreement with the experimental results in this experiment will determine which model describes the TOF MS experiments better. The initial conditions required for calculating the gas dynamics were obtained either from previous experimental work or inferred from previous simulation work made by Rossall *et al.*[36] and Aslanyan *et al.* [37].

The initial conditions of the plume are the main connection with the experimental results in this case, the initial laser energy used was 9.5×10^{-5} J (E0) and the initial size in the X direction was 9.5×10^{-5} m (X0). A general overview of the results obtained from the equations are shown in figures 5.6a)-5.6d). The experimental measured ion ratios in the TOF MS device were measured at 2 mm from the laser interaction point. The simulations in figure 5.6 show the temporal evolution of plasma density and temperature at 2 mm. From these parameters, and the coronal equilibrium assumption, the ionisation state and ion flux can be calculated, which can be compared to the experimental TOF MS results. It should be noted that the values for E0 and X0 are initial estimates based on experiments (E0) and previous modelling (X0). They are used as fitting parameters in the model to match the experimental MS spectra. These figure are representative of all the following calculations using different initial conditions and all of them have the same shape for density, pressure and temperature with a maximum point for both the isoentropic and isothermal model. For the temperature case, for all modelled energies and sizes have the same peak shape in the isoentropic case and the same convex shape in the case of the isothermal model.

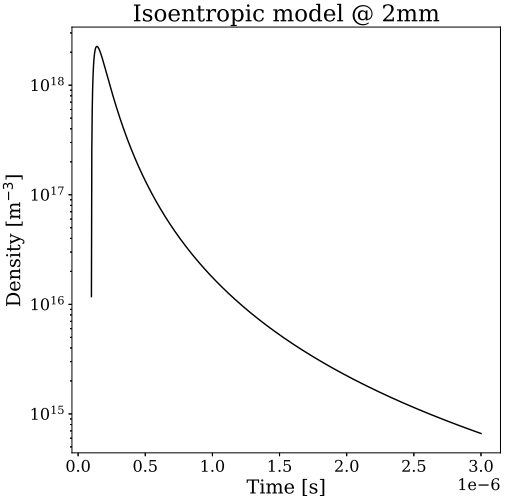

(a) Time evolution of plasma density reaching the TOF MS device at 2mm, for the isoentropic model.

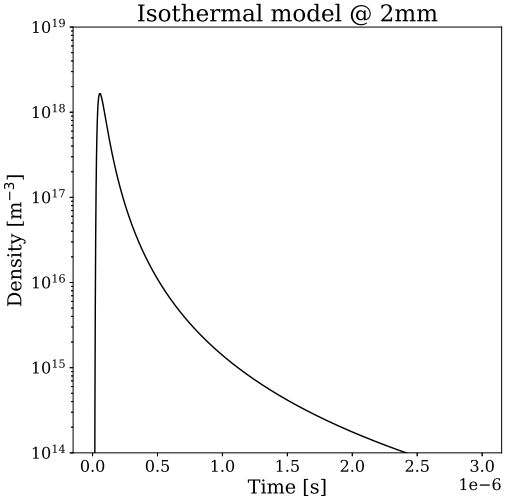

(b) Time evolution of plasma density reaching the TOF MS device at 2mm, for the isothermal model.

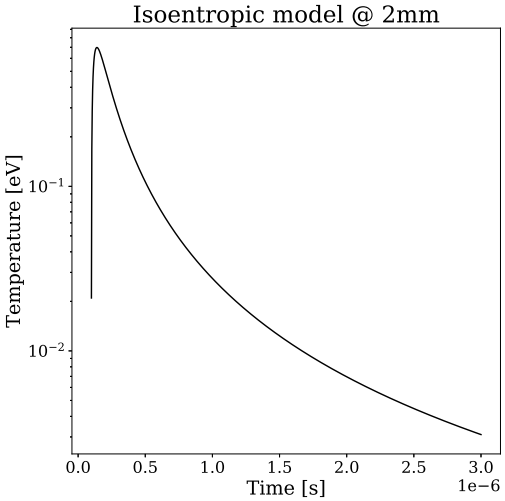

(c) Time evolution of plasma temperature reaching the TOF MS device at 2mm, for the isoentropic model.

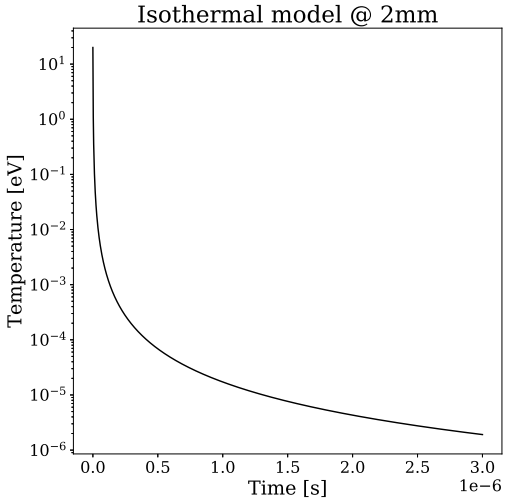

(d) Time evolution of plasma temperature reaching the TOF MS device at 2mm,for the isothermal model.

Figure 5.6: Temporal evolution of density and temperature for the plasma modelled at 2 mm

Figure 5.6 shows that the ions arriving at the entrance of the TOF MS device at different times have a range of temperatures. The time-integrated experimental spectra will be a (density-weighted) average of these ions at different temperatures. This means that the temperatures derived in table 5.3 are not directly related to a single plasma temperature in the plume, but an “effective temperature”, representing an density-weighted average value.

Even though this can be used when comparing different conditions, it makes direct interpretation of the plasma physics of the plume difficult. The temperature calculated in figure 5.6d) with the isothermal model seems to be unfeasible due to the laser parameters, at $t = 0$ the plasma temperature would reach 10 eV which would require a higher laser intensity. The plasma temperature modelled using the isoentropic model is more likely to be in accordance with the experiments, for this reason the following results were calculated using this model.

From the model predictions of density and temperature, the total number of ions in different ionisation stages reaching the TOF MS entrance as a function of time can be calculated. For every time point, the average ionisation stage can be calculated from the temperature and total density using the coronal equilibrium model. This then gives a density of different ionisation stages reaching the TOF MS entrance. An example of this is shown in figure 5.7. This figure shows the number of particles at different ionisation stages reaching the extraction grid and passing through the hole into the free flight zone in the TOF device. From this picture the temporal evolution shows that after the laser interaction with the material (t=0) there is a peak in the 2^+ ions and rapidly decays, the same behaviour is observed for the 1^+ ions but there is a local increase of these ions probably produced by the 2^+ ions decay, a notch in the neutrals is observed probably produced by the decay of the 1^+ ions. As in the previous cases with the plasma parameters, there is a peak point where the number of particles reach its maximum value and the count of particles starts to decrease. By integrating each of these signals over time, a comparison to the experimental TOF MS spectra can be made by looking at ratios of different ionisation stages.

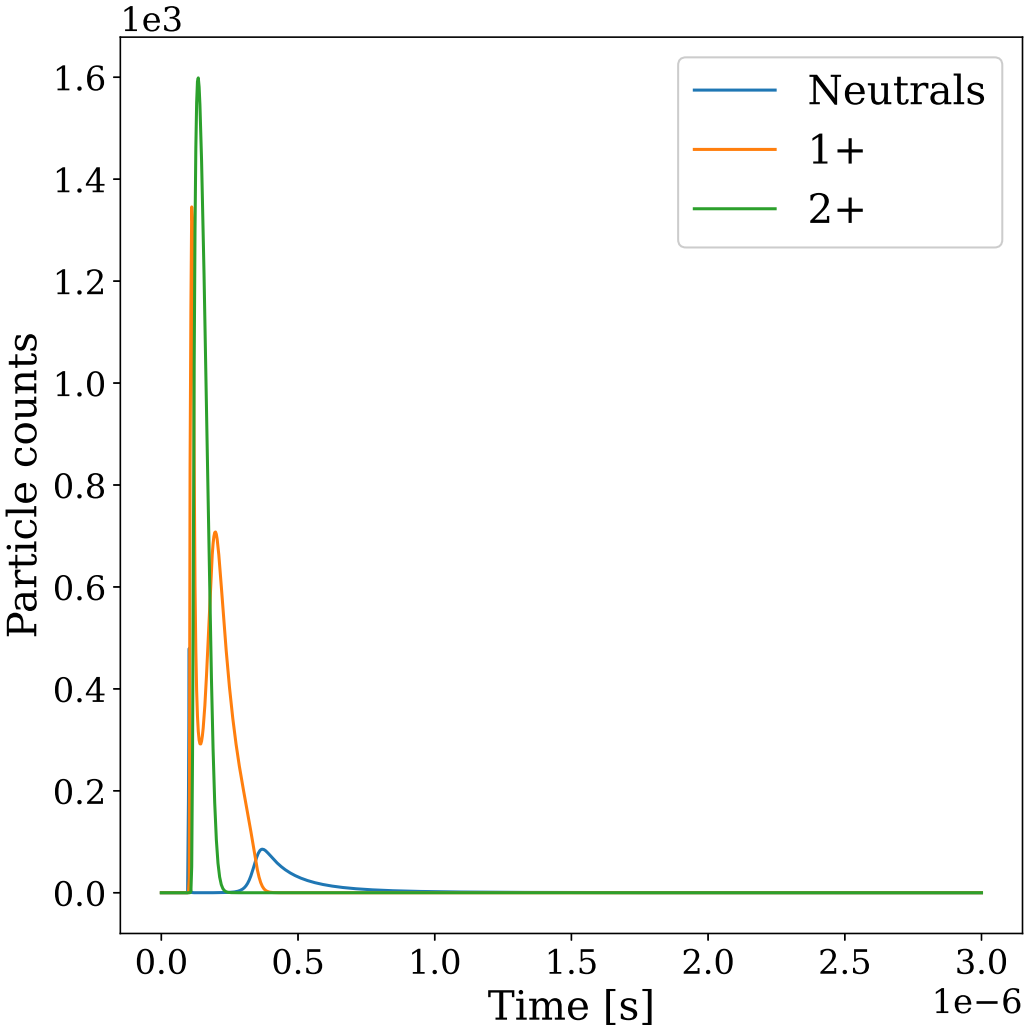

Figure 5.7: Ions measured in the plasma for the modelled conditions at 2 mm using the isoentropic model.

The experimental ratios measured in the TOF spectrometer are used to compare the simulated ratios. As previously mentioned, the physical characteristics of the TOF device restrict the plasma expansion up to 2 mm, this is the place where the ground plate is located. The distance of 2 mm is taken as a fixed parameter in the model. The initial plume size in the x direction (perpendicular to the target surface) is considered as a fitting parameter, but only within a limited range of 20-100 um, based on previous simulations. The energy is also a fitting parameter, based on experimental measurements of the energy. These ranges were taken into account and simulations were found where the values of energy and size give a modelled ion ratio that matches the experimental one.

Since there are 2 free parameters (free within a limited range), it is not possible to find a single point of best fit, there is a range of combinations of size and energy that produce the required ratios.

Figures 5.8(a)-5.8(d) show the values that are within the experimental ratio values. Namely, the black dots in these figures represent the combination of initial energy and initial plume size that agree with the ionisation rates measured in the experiments for these materials. From these images, it is clear that these values follow a trend that seems natural in the sense that an increase in energy would decrease de size of the plume after the interaction as the particles travel to the extraction grid with higher velocity.

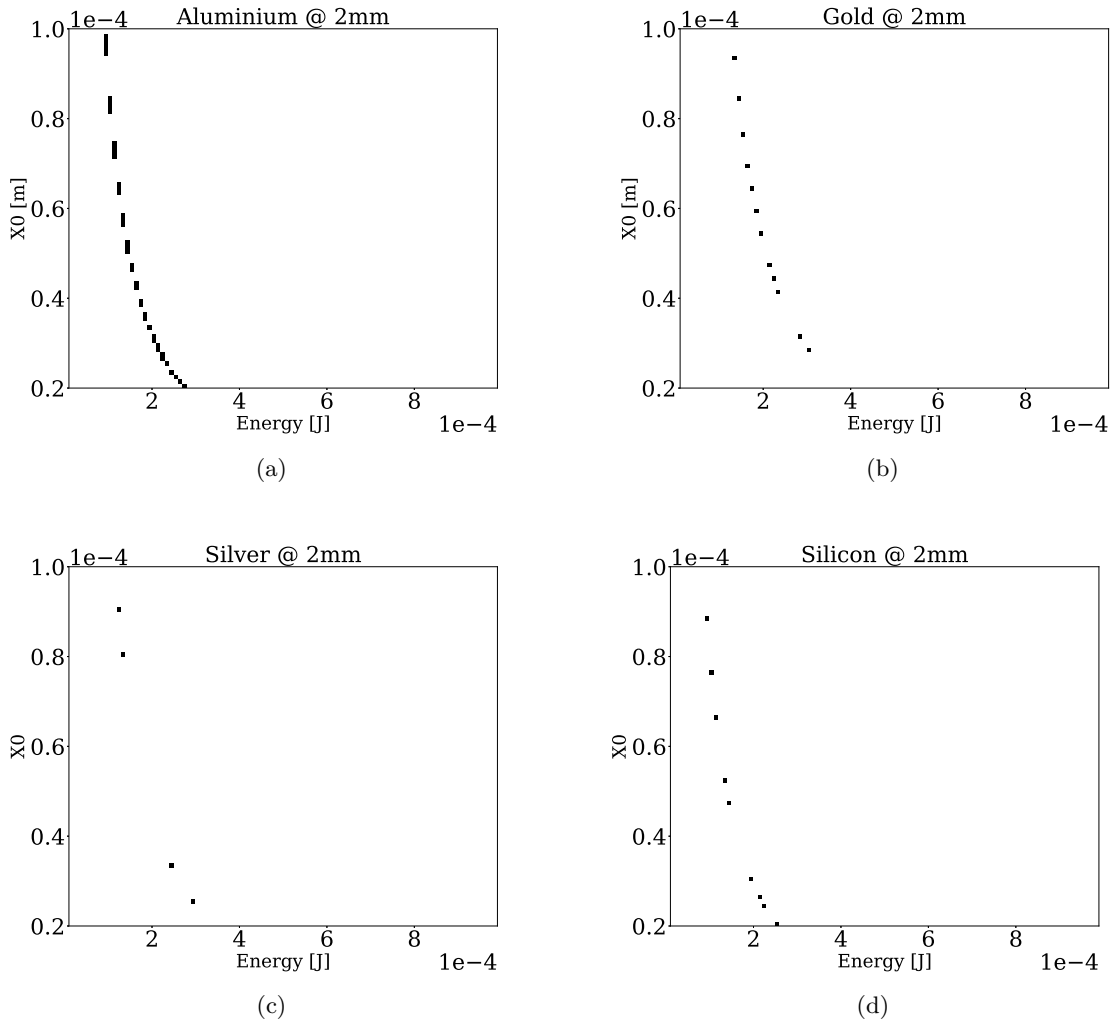

Figure 5.8: Initial plume size in the the perpendicular direction versus the energy

The simulations in figure 5.8 are based on the plume properties at 2 mm from the interaction point. From a plasma physics point of view, the properties at the target surface, immediately after the laser interaction are more relevant. The model used describes the full temporal and spatial evolution of the plume, so the initial temperature at t=0 s after

the laser can also be studied in the model. In order to do this, it is required to trace back the peak temperatures in different points, the minimum distance calculated was at 2 μm. All the temperature on the surface were calculated using the corresponding values for the coronal model, figures 5.9-5.12 show these temperatures for all the materials at $x = 2\,\text{mm}$. These figures correspond at $t = 30\,\mu\text{s}$, at this time the ionisation rates are similar to the experimental results. With the expansion model(s) matching the experimental ion ratios, we have some confidence that the plume expansion is well described by the expansion model. This then allows to investigate the modelled plume parameters more carefully. Figure 5.7 show that the time at which ions are entering the TOF MS is sharply peaked. Therefore, the spatial profiles of the density and temperature of the expanding plume at this time, give a fairly accurate representation of the time at which the (majority) of the plume reaches the TOF MS device.

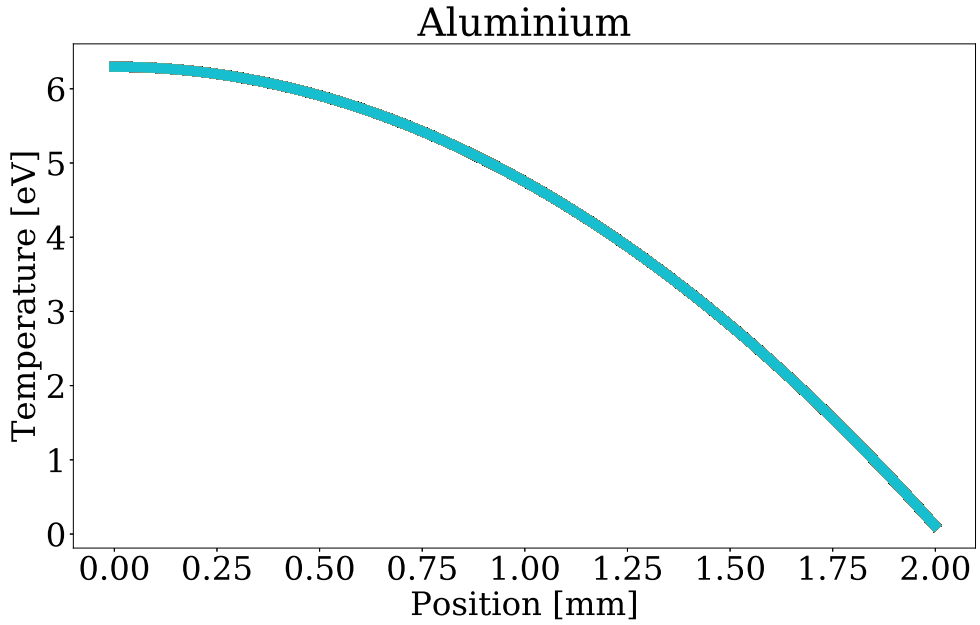

Figure 5.9: Plasma temperature vs. length at t=30 µs for aluminium

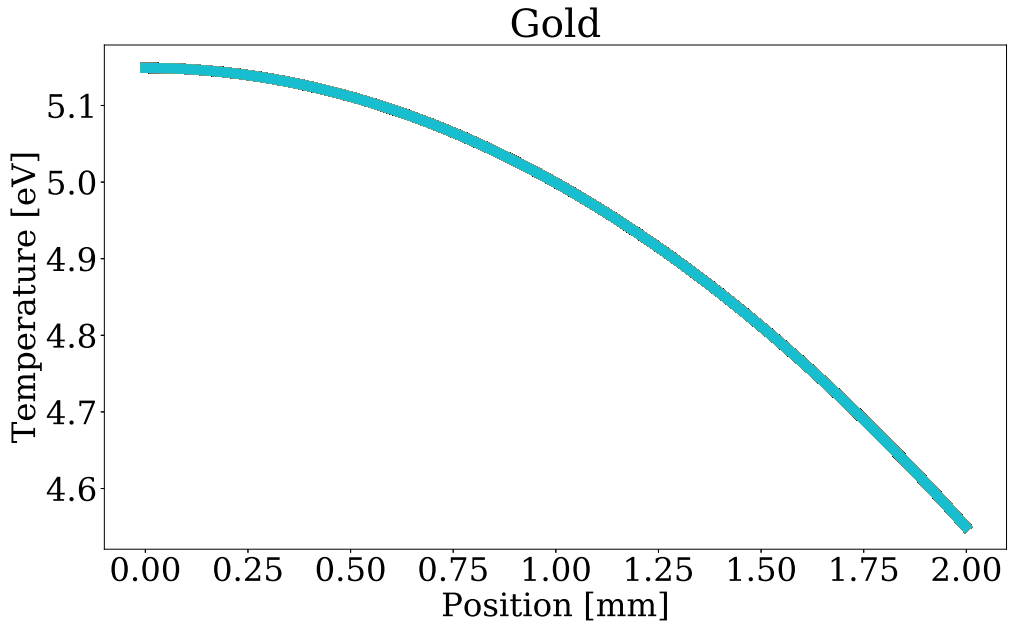

Figure 5.10: Plasma temperature vs. length at t=30 µs for gold

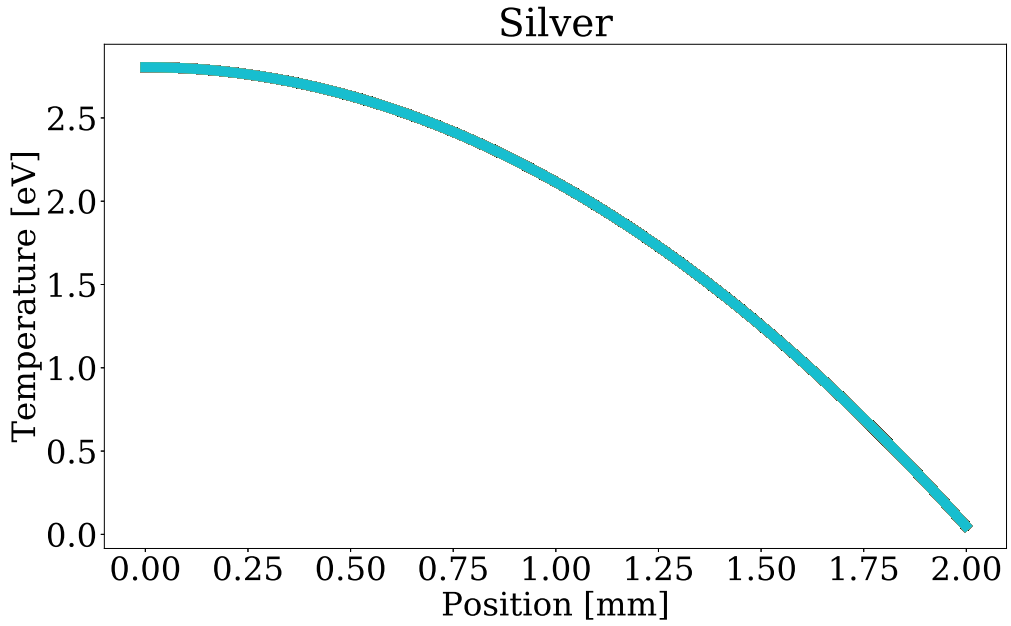

Figure 5.11: Plasma temperature vs. length at t=30 µs for silver

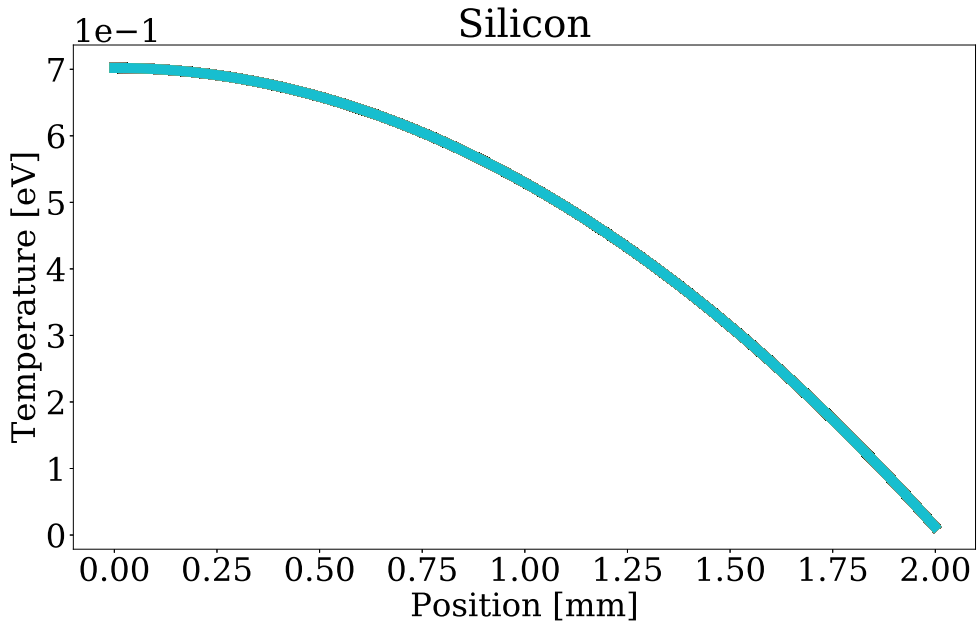

Figure 5.12: Plasma temperature vs. length at t=30 µs for silicon

If the temperature profile is traced back to t=0 s, then the temperature at the target surface, right after the laser interaction with the material can be found. However, when this is done, temperatures several orders of magnitude higher than what is realistic are found for all materials, indicating that these predictions for t=0 s are not correct.

5.3 Discussion and conclusion

In comparison to the results obtained for the ionisation ratios and the coronal model presented in table 5.3, clearly there is a difference with the results at $x = 2\,\text{mm}$ using the isoentropic model calculations. Moreover, there is consistency in the order of magnitude of the measured values across the materials, giving some confidence in the method. On closer inspection, higher temperatures are observed for the heavier materials Au and Ag. This is in line with what was calculated by Whittaker et *al.* [91] for x-ray illumination of C and Fe. It is important to note that the temperatures presented in table 5.3 are temperatures of an equivalent plasma in steady-state coronal equilibrium. In reality, there is a plasma with time-varying properties arriving at the grid position. Because the measurement is effectively time-integrated (on the time scales of the expansion), the measured ion ratio will represent an "effective temperature", not necessarily a true representation of the time-dependent plasma plume.

If the model is used to trace back the plasma properties at t =0 sec that would be needed to produce the experimentally obtained ion ratios, it is clear that this is not feasible. Temperatures, several orders of magnitude higher than what is realistic would be needed to

obtain a match with the experimental ion ratios.

A possible explanation is that the measured ions might be dominated by the most energetic ions created after the laser interaction, so-called fast ions. This could lead to an overestimate of the temperature, this could also lead to the mismatching of the temperatures measured based on the experimental ion ratios and the calculated with the expansion models. It is clear that the plume expansion is more complex than a simple adiabatic expansion. The existence of (highly charged) fast ions is not predicted by these expansion models, but it is clear that they significantly affect the results measured by the MS. On one side, this makes it difficult to derive bulk plasma plume temperatures from the MS measurements, on the other hand, it allows the further study of these low-density fast ions, in particular if some time-resolution in the MS measurements can be achieved.

Chapter 6

Feasibility study of using EUV radiation for shadowgraphy of laser-produced plasma plumes

In this chapter, the use of EUV radiation for shadowgraphy of laser-produced plasma plumes is investigated. In particular, high-density regions are studied where conventional optical shadowgraphy does not work because the plasma density is above the critical density for optical light. The critical density for EUV radiation is much higher, opening up the possiblity of probing the high-density parts of the plasma plume, inaccessible with optical light shadowgraphy. In this chapter, a shadowgraphy diagnostic is modelled, calculating the effects of both refraction and absorption when EUV and optical radiation interact with a laser-produced plasma plume.

6.1 Laser produced-plasma simulations

The laser-produced plasma plumes that are to be diagnosed by EUV shadowgraphy were calculated using Pollux. This code is described in section 3.5 and the outcomes are datasets with the spatial and temporal distribution of different parameters such as, temperature, density and ionisation degree of the plasma. These simulations are taken as example plasmas on which the EUV shadowgraphy diagnostics is tested and compared to traditional optical shadowgraphy. Section 2.5.2 describes the shadowgraphy diagnostic in more detail, including a typical experimental arrangement for this diagnostic.

Sections 2.5.2 and 2.6 describe the absorption and refraction phenomena observed when an electromagnetic wave interacts with a plasma. The objective of this chapter is to investigate the feasibility of EUV shadowgraphy by quantifying the effects of refraction and absorption of a typical diagnostic setup as well as comparing performance to shadowgraphy with optical light.

Table 6.1 describes the laser parameters utilised for the Pollux simulations. The wavelength range is in the optical spectrum and the chosen intensities and pulse lengths are comparable to most of the commercial visible lasers available.

Table 6.1: Laser parameters for the EUV laser source.

Laser parameters	
Optical	
Wavelength:	532 and 1064 nm
Energy output:	up to 80 μJ
Pulse length:	1 ns
Spot size:	0.625- 5 mm

The intensity of the laser in the simulations was varied to achieve higher density plasmas and understand the main difference of the laser interaction above the critical density in shadowgraphy.

Gold, copper, and aluminium targets were simulated in POLLUX to understand also how different conditions of the laser-produced plasma affect the absorption and refraction of the incoming probing beam used for shadowgraphy. Figures 6.1-6.3 present some representative examples of the data outputs from POLLUX. These figures are for an aluminium target and they were taken at 3 ns after the laser interaction with the sample. These figures are representative and all the materials had similar behaviours.

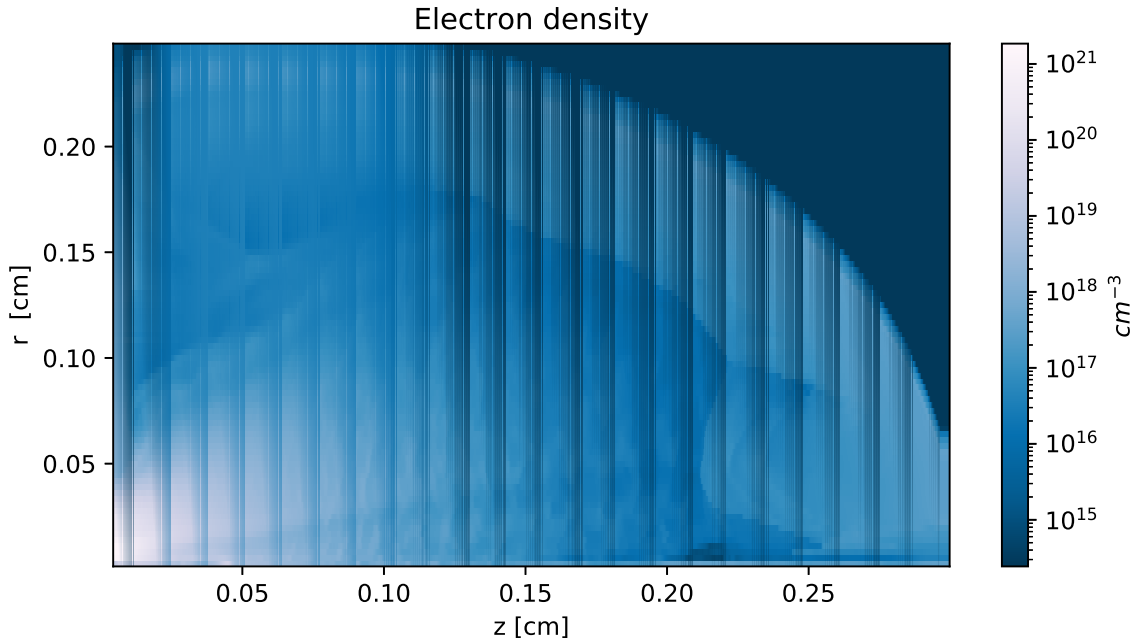

Figure 6.1: Electron density of an aluminium plasma produced with a 532 nm laser source with an intensity of 5×10^{11} Jcm^2 and a spot size with a radius of 6.25 mm after 8 ns of interaction.

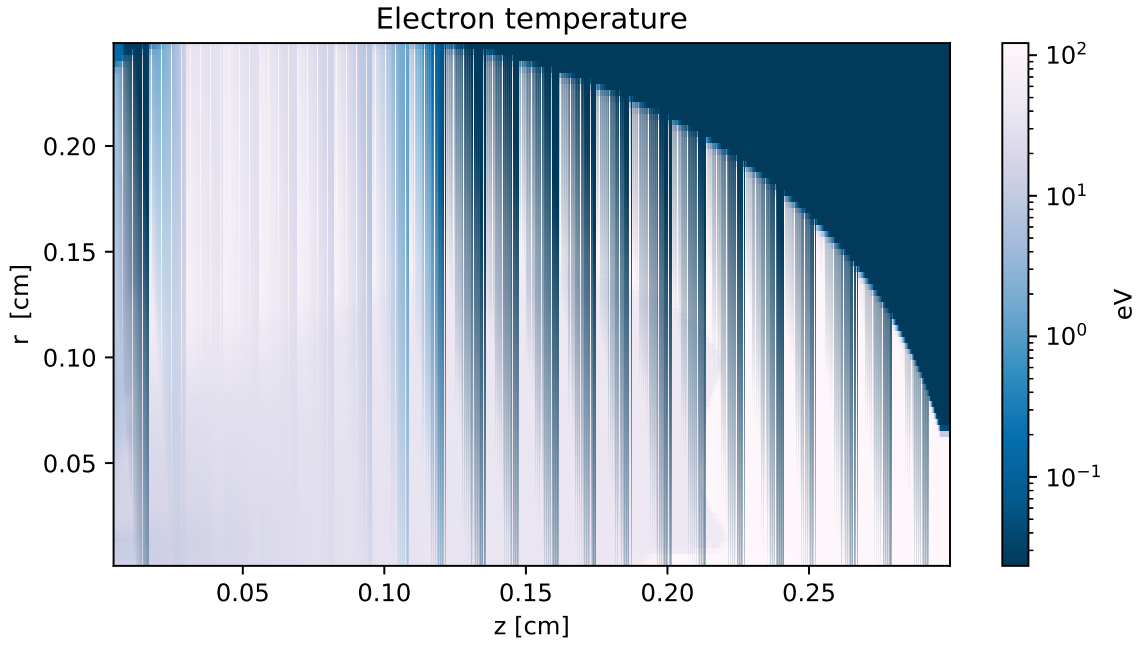

Figure 6.2: Electron temperature of an aluminium plasma produced with a 532 nm laser source with an intensity of 5×10^{11} Jcm^2 and a spot size with a radius of 6.25 mm after 8 ns of interaction.

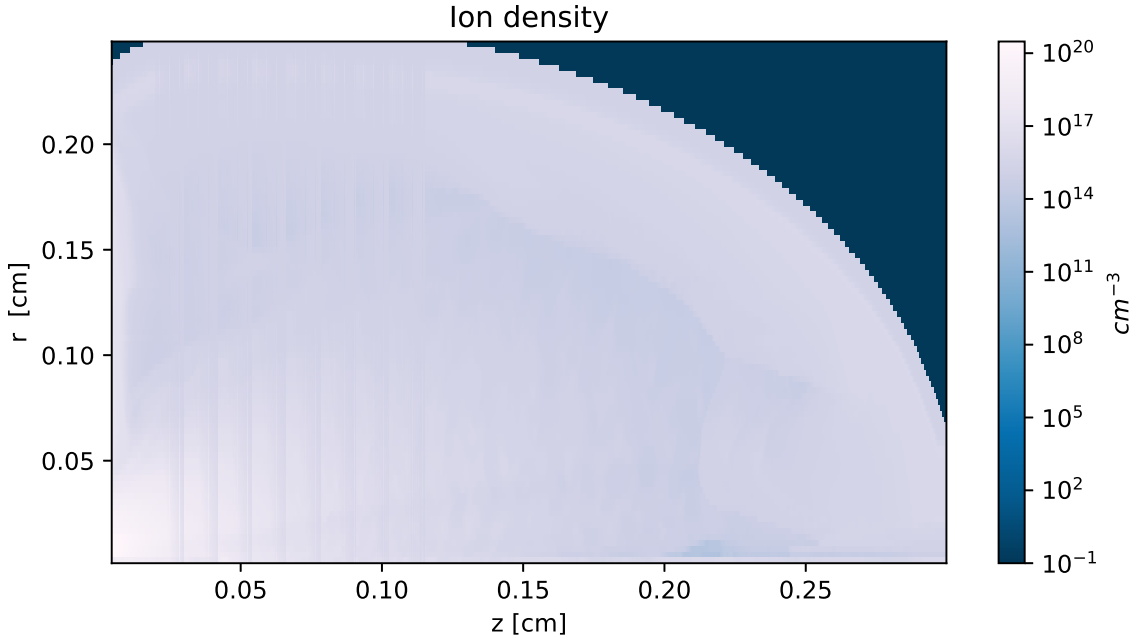

Figure 6.3: Ion density of an aluminium plasma produced with a 532 nm laser source with an intensity of 5×10^{11} Jcm^2 and a spot size with a radius of 6.25 mm after 8 ns of interaction.

POLLUX output datasets have an azimuthal symmetry around the z axis and the figures presented previously are half of the spatial distribution of the plasma. Figure 6.4 shows the complete scheme of the analysed simulation. An uniform beam of light travelling from the bottom of the image, moving upwards through the plasma plume and is then detected, spatially resolved along the z axis (but only on axis in the perpendicular direction).

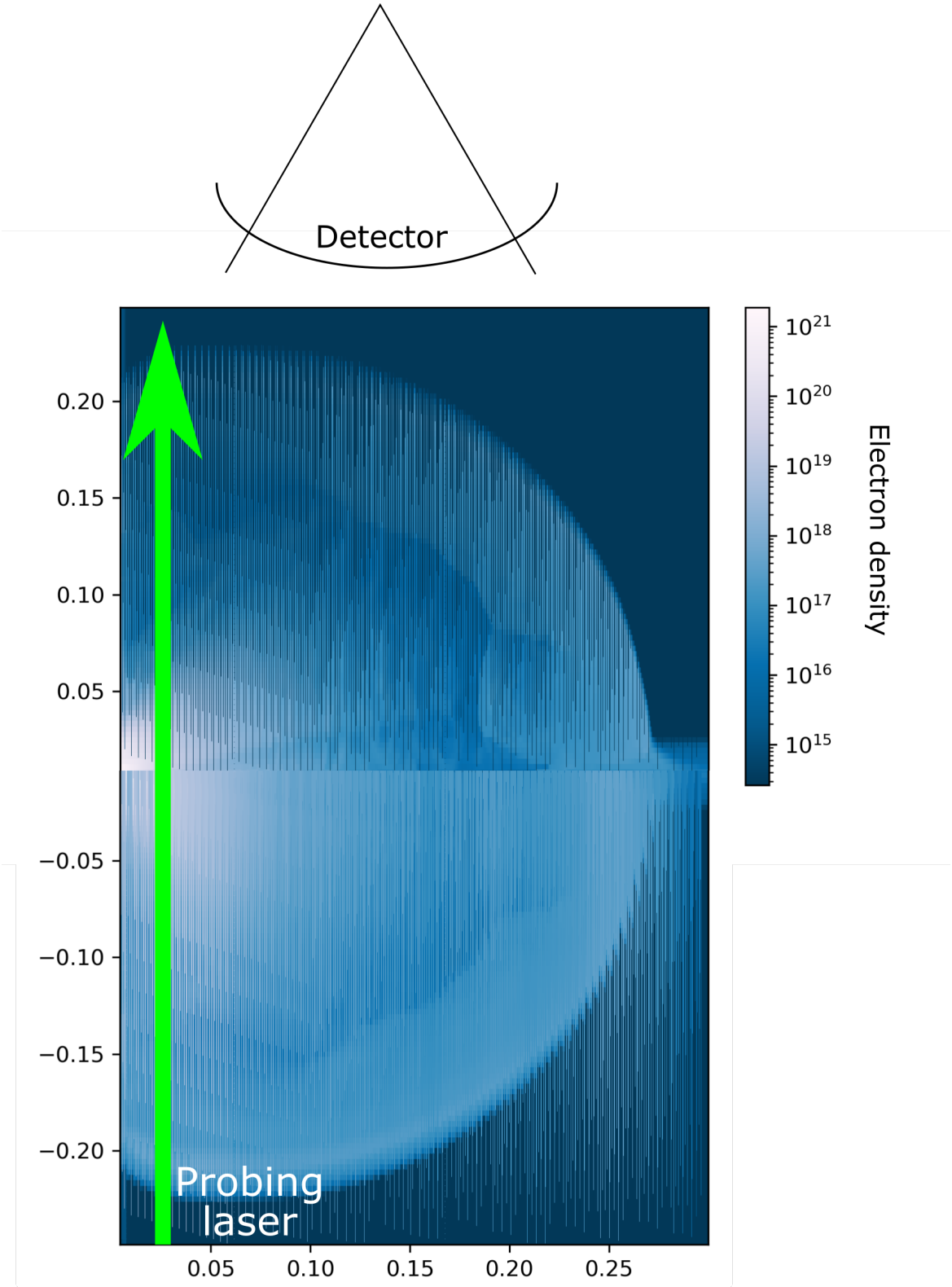

Figure 6.4: Probing beam travelling through the complete plasma plume from the bottom of the mesh to the top where is located the detector

6.2 Refractive index

The refractive index spatial distribution can be calculated based on the spatial distribution of the electron density of plasma. An example is presented in figure 6.1. This distribution can be calculated using the expression [92],

$$N^2 = 1 - n_e/n_c \tag{6.1}$$

where, N is the refractive index of the plasma, n_e is the electron density of the plasma and n_c is the cutoff or critical density of the plasma defined as,

$$n_c \equiv \omega^2 m\epsilon_0/e^2 \tag{6.2}$$

where ω is the frequency of the incident probe light. In figure 6.5 and 6.6 are presented the refractive index spatial distributions for the probe beam wavelengths of interest, 46.9 and 532 nm. These wavelengths are chosen since laser sources are available at these wavelengths; EUV capillary laser at 46.9 nm and a Nd:YAG laser (frequency-doubled) at 532 nm. These figures are representative and all the targets present a similar behaviour.

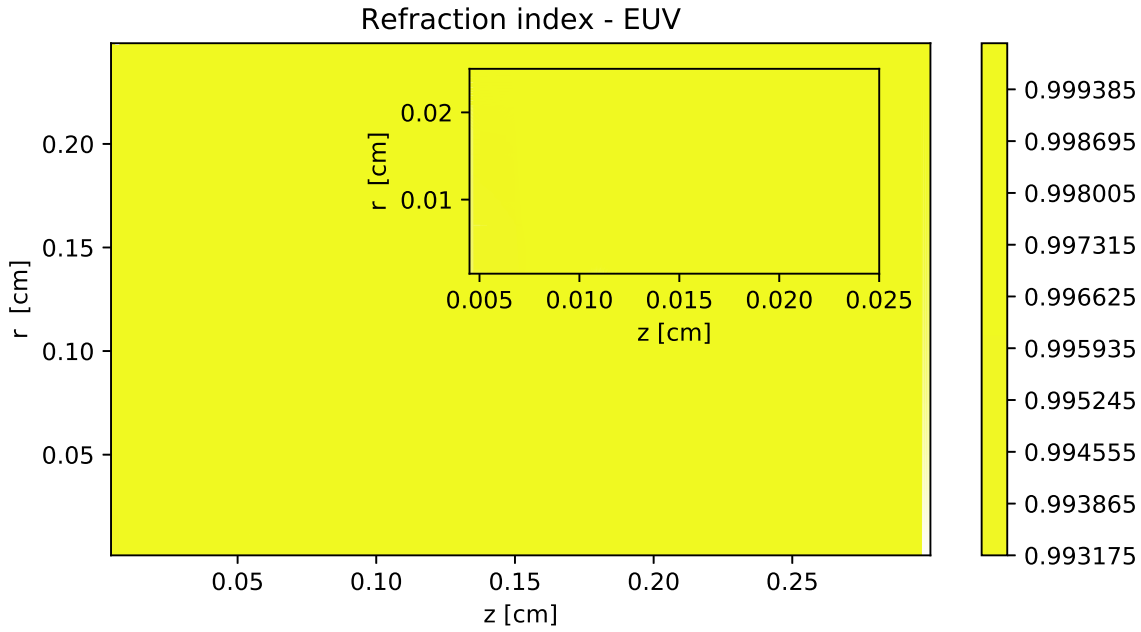

Figure 6.5: Spatial distribution of the refractive index for a gold target at 7 ns after the laser interaction. The wavelength of the probe beam is assumed to be 46.9 nm.

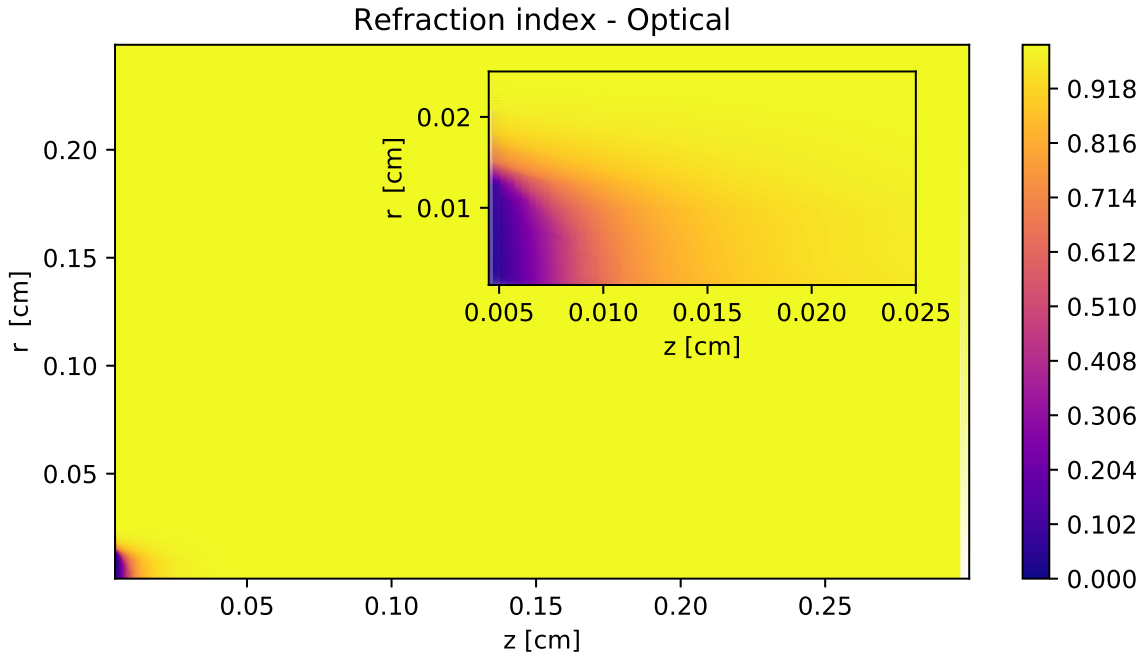

Figure 6.6: Spatial distribution of the refractive index for a gold target at 7 ns after the laser interaction. The wavelength of the incident probe beam is assumed 532 nm.

Figure 6.5 clearly shows a minimum effect in the refractive index, the electron density is two orders of magnitude lower than the critical density for 46.9 nm which is $4.5 \times 10^{23}\,\mathrm{cm}^{-3}$. In contrast, for radiation at 532 nm where the critical density is $3.53 \times 10^{21}\,\mathrm{cm}^{-3}$ and the refractive index gets as low as zero in figure 6.6, indicating that the density is above the critical density for this wavelength and all radiation will be absorbed. The refraction effects produced by the refractive index are investigated for different plasmas and compared with the absorption effects of the plasma for different wavelengths.

6.3 Refraction effects

The effects of refraction were quantified based on the Poisson's equation described in section 2.5.2 where the refractive index is related with the effect of the total intensity changes after the interaction. Poisson's equation 2.59 shows that gradients of refractive index in both the z and r direction need to be taken into account. The direction of propagation of the EUV light is s and that equation 2.59 integrates the refractive index effects along the s direction. Then the effects of both r and z refraction are calculated. Based on this information all the targets were analysed using this equation to quantify the intensity change due to refraction.

$$\left(\frac{\partial^2}{\partial z^2} + \frac{\partial^2}{\partial r^2}\right) \int_0^{\Delta s} n(z, r, s)\mathrm{d}s = -\frac{1}{L}\frac{I(z, r) - I_0}{I_0} \tag{2.59}$$

Examples of the refraction effects of density gradients in the plasma in the z and r directions are shown in figures 6.7 and 6.8 respectively. The plotted intensity is the intensity at the symmetry axis (r=0) but as a function of z.

These figures correspond to an aluminium target at 8 ns after a 532 nm laser was irradiated on the target. The electron density is above the critical density at this wavelength and these figures are a good example to show the effects of a laser travelling in a plasma plume above the critical density. In these particular cases, the laser final intensity of the backlight laser is completely refracted and cannot travel through the plasma in any point of plume.z

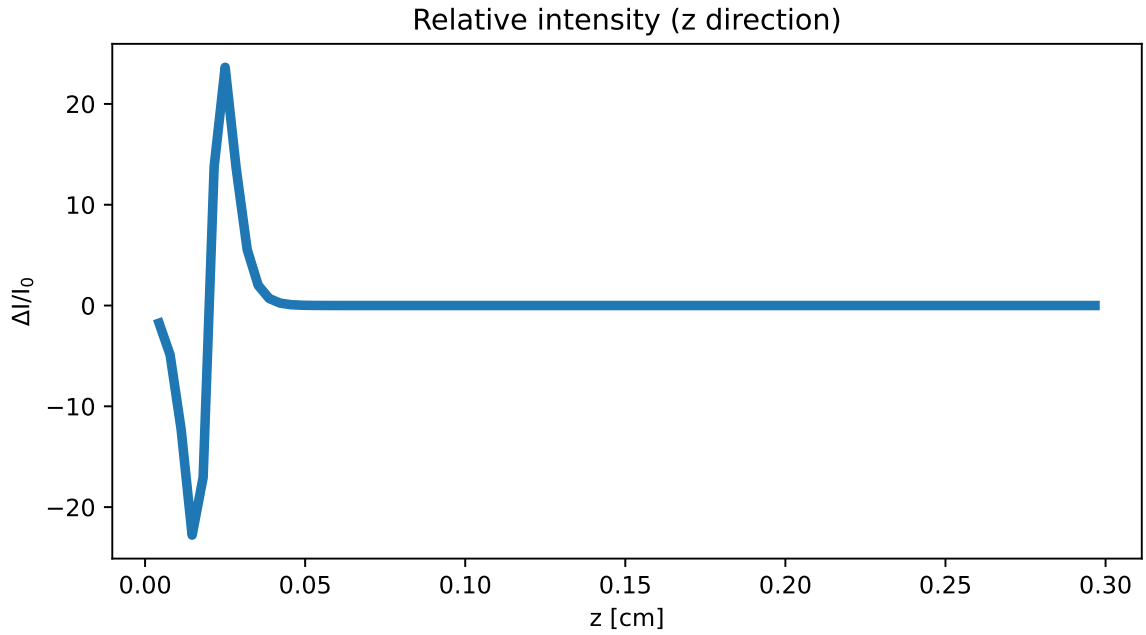

Figure 6.7: Refraction effects produced in the z direction in a 532 nm laser travelling through a plasma plume.

Figure 6.7 shows that because of the shape of the density gradient in z, light at small z is refracted away from the laser interaction point, causing a decrease in measured intensity at small z, and a corresponding increase at slightly larger z. Figure 6.8, the decrease in intensity for small z values is due to the gradient in r causing light on axis (r=0) being refracted away from the centre towards the edges ($r > 0$). Since the detector is assumed to only measure on axis (r=0), a reduction of the intensity is observed as a result of the density gradients in r.

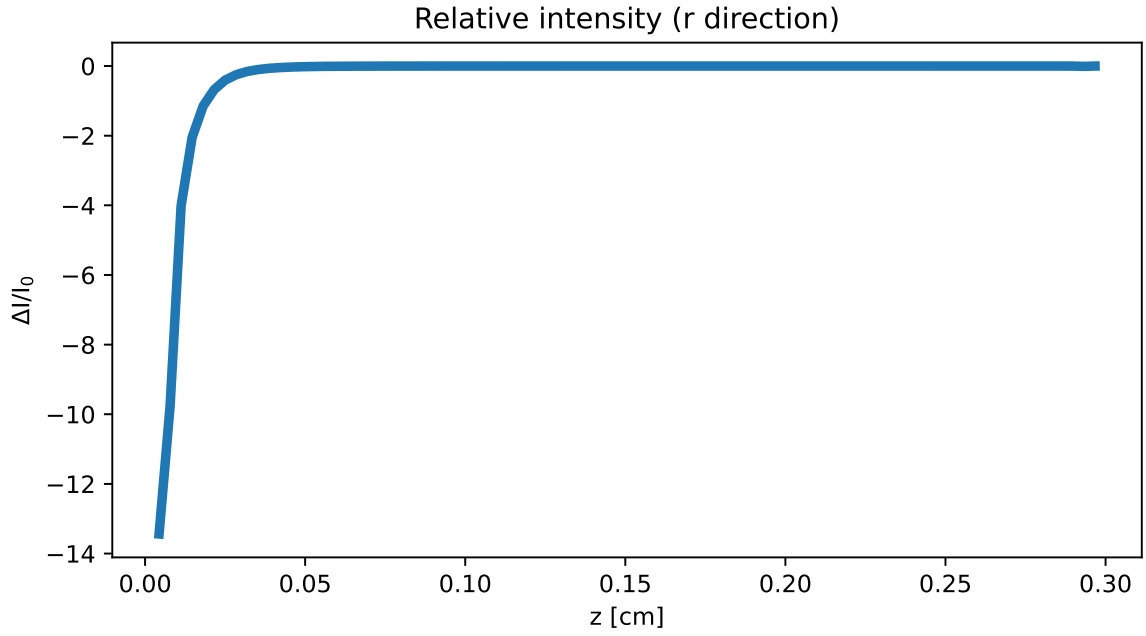

Figure 6.8: Refraction effects produced in the r direction in a 532 nm laser travelling through a plasma plume.

The total effect of the contributions of the z and r directions are summarised in figure 6.9. An important note is that the values of the intensity change are larger than 1, implying that all the light is refracted. The reason is that the plasma is above the critical density. This means that the general trend of the figure, a decrease at low z, leading to an increase at slightly larger z is real, the values in the figure are not.

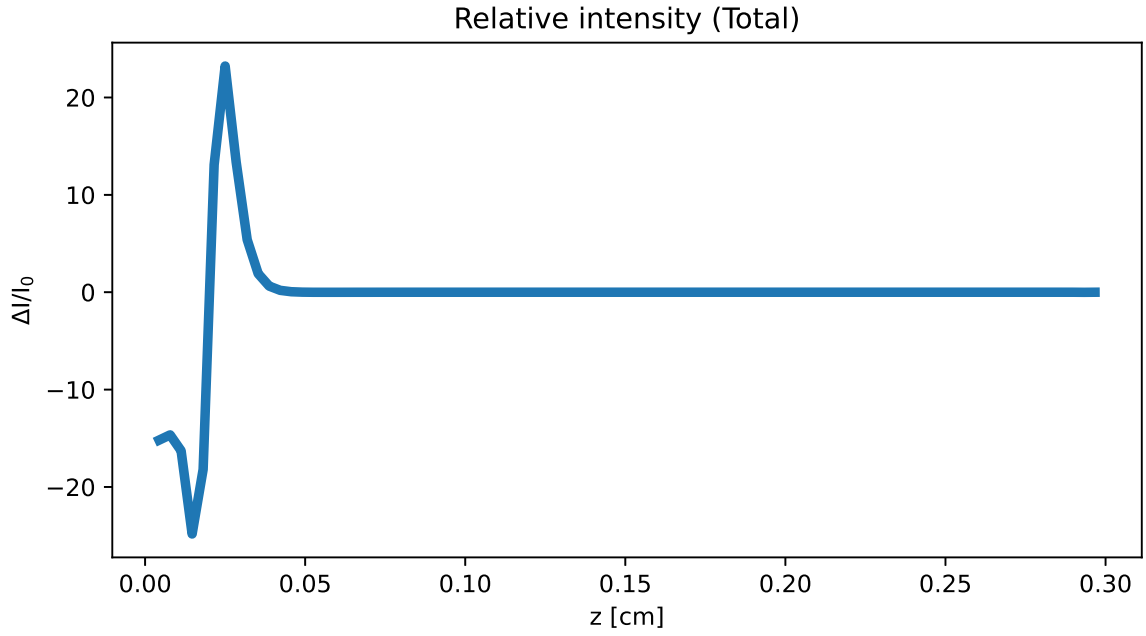

Figure 6.9: Total refraction effects produced in the z and r directions when a 532 nm laser travels through a plasma plume.

In order to compare the effects of the refraction with a shorter wavelength laser, figure 6.10 shows the total intensity changes. The overall shape of the figure is very similar to the visible wavelength laser (figure 6.9), with a large decrease at small z; resulting from a combination of refraction in both z and r. The increase in intensity at slightly larger z (z> 0.3 cm) is due to the refraction in z, similar to figure 6.7 for the visible laser.The biggest difference is the magnitude of the intensity change, For the EUV light, the variation is +/- 10 %. The main reason is that the plasma density is below the critical density for EUV light. Importantly, this is a change that can be measured experimentally.

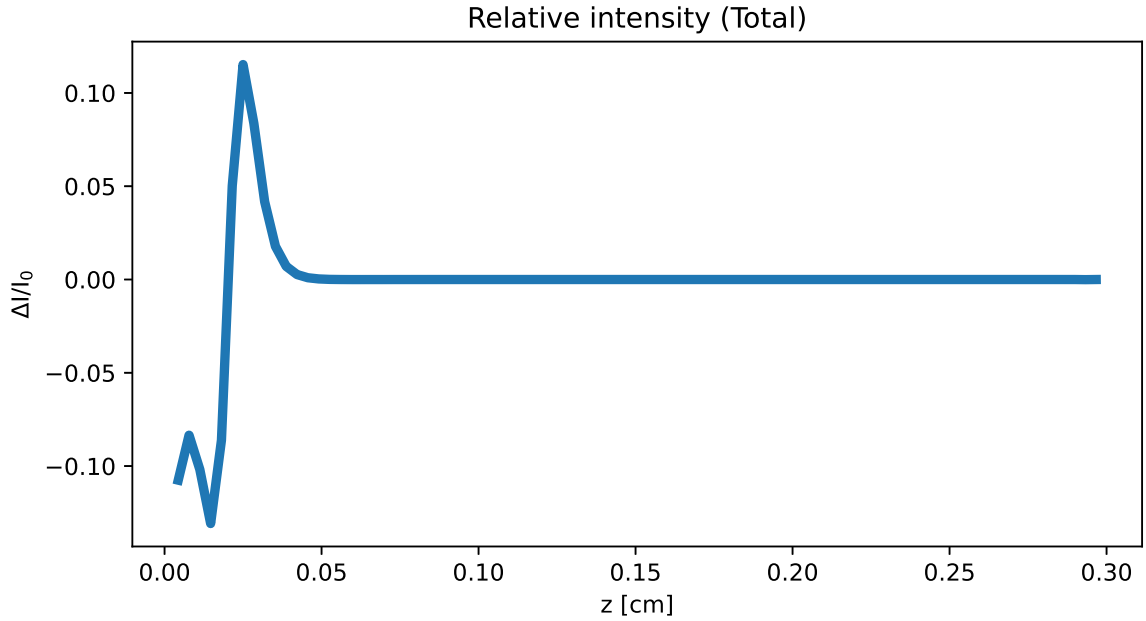

Figure 6.10: Total refraction effects produced in the z and r directions when a 46.9 nm laser travels through a plasma plume.

The results so far show that the effects of electron density gradients are noticeable when the density is close to the critical density (for a certain wavelength). In the remainder of this section, a plasma with a density significantly below the critical density will be investigated. For this a plasma plume produced with a laser at 1064 nm, an irradiance of 5×10^9 $\mathrm{Js}^{-1}\mathrm{cm}^2$ and a spot size of 5 mm was considered. Figure 6.11 shows the electron density profile of the plume 11 ns after the laser interaction. The electron density is three orders of magnitude lower than the critical desnity for the 532 nm laser used for the comparison between the optical and EUV backlight. Close to critical density, the wavelength used for backlighting the shadowgraph should be planned to get adequate information.

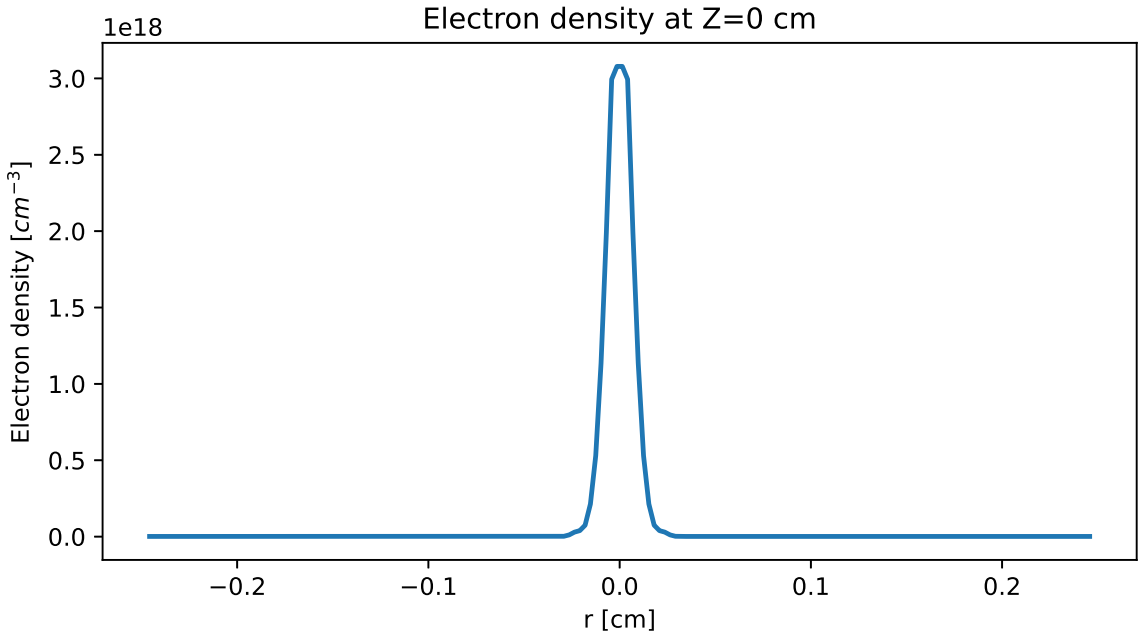

Figure 6.11: Electron density of the plasma plume produced after the ablation of an aluminium target

In this case where the electron density is significantly below the critical density, the refraction effects are minimal as shown in figure 6.12 and there is a maximum change of intensity of $\sim 4\%$. This could be difficult to measure in a real detector and a longer wavelength laser would be better in this case. For the case of an EUV source as backlight in the shadowgraph as presented in figure 6.13, the maximum change of intensity is $\sim 1 \times 10^{-5}\%$ which makes this wavelength unviable for these plasma conditions.

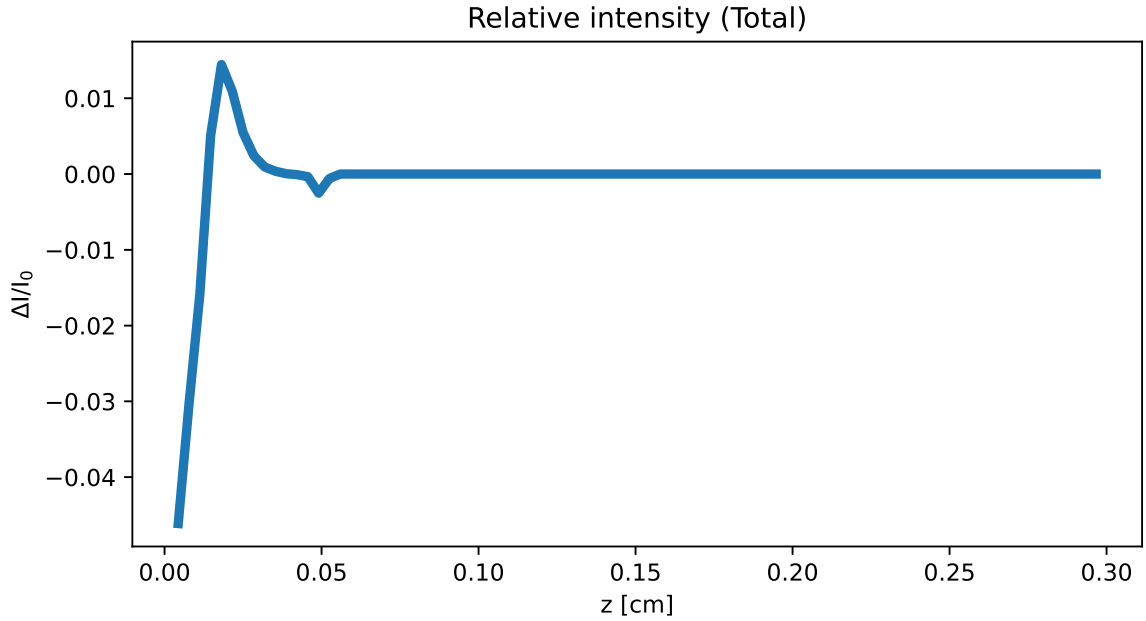

Figure 6.12: Refraction effects produced for a low density plasma using a 532 nm laser to probe the plume

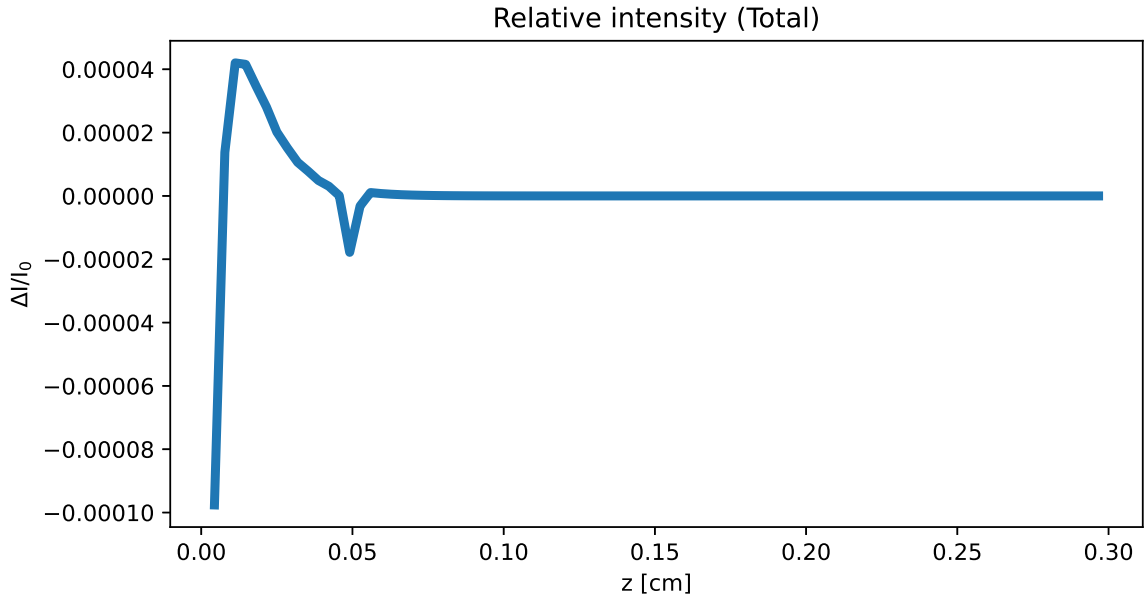

Figure 6.13: Refraction effects produced for a low density plasma using a 46.9 nm laser to probe the plume

6.4 Absorption effects

During the interaction of laser radiation with plasma, the absorption of the beam energy is one of the most important effects to consider during the probing of a plasma. As mentioned in section 2.6, inverse bremsstrahlung is the main absorption process. Equation 2.66 quantifies the absorption produced by the plasma plume. Pollux provides all the information required to compute this equation and calculate the spatial distribution of the absorption.

$$K_{ff} = 8\sqrt{\pi}\Big(\frac{e^2}{4\pi\epsilon_0}\Big)^3 \frac{4}{3c^3}\frac{Z_i^2}{m_0^2} n_e n_{z_i} \Big(\frac{m_0}{2k_B T}\Big)^{1/2} \frac{\pi^2 c^2}{\hbar\omega^3}\Big(1 - \exp\big(-\frac{\hbar\omega}{k_B T}\big)\Big) \tag{2.66}$$

To compare refraction and absorption in shadowgraphy during laser-plasma interactions and the effects of the probing backlight wavelength, in this section are presented the absorption effects on the same simulations as section 6.3. An aluminium target will be used as a representative case but gold and copper were also analysed. The absorption in electron density under and above critical density are presented for 532 and 46.9 nm backlighters.

A low density plasma plume ($3.0\times10^{19}\,\mathrm{cm}^{-3}$) obtained using a 1064 nm laser for ablation of aluminium with a laser irradiance of $3.5 \times 10^9\,\mathrm{Jcm}^{-2}\mathrm{s}^{-1}$ after 12 ns of interaction and a spot size diameter of $6 \times 10^{-2}\,\mathrm{cm}$ was used for the analysis of the absorption effects in shadowgraphy for a case of electron density below critical density. The total absorption is calculated using Beer-Lambert equation 2.17 where the absorption coefficient α is K_{ff} and the final intensity is calculated with the accumulative value of the total length Δz,

$$I(z) = I_0 e^{-\alpha z} \tag{2.17}$$

Figures 6.14 and 6.15 are the total absorption of a 532 and 46.9 nm beam travelling through the plasma. As expected, the effects of absorption are limited to the high density part of the plasma plume. For the leading edge of the plume, z>0.3 mm, the absorption effects are negligible due the to low density and small thickness of plasma the light travels through.

In figure 6.14 is presented the absorption effects for a 532 nm laser travelling inside the plasma plume. Moreover, the magnitude of the absorption effects is very small $< 10^{-4}$, meaning that it is below what can be routinely measured using existing detector technology.

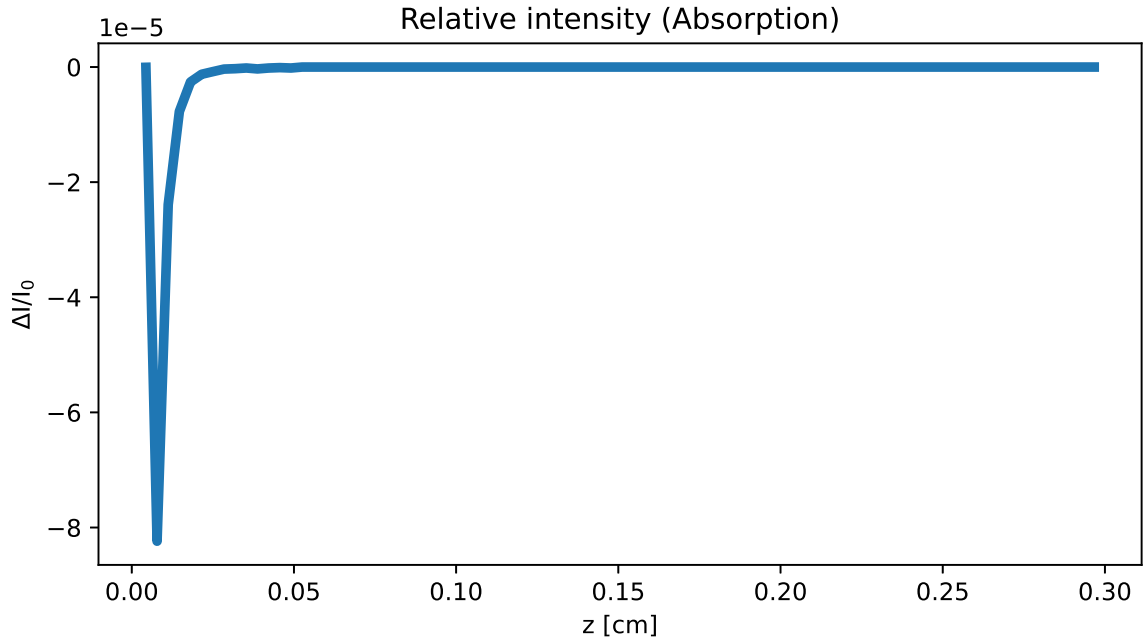

Figure 6.14: Absorption effects of the intensity of a 532 nm laser inside a low density aluminium plasma

Figure 6.15 show the absorption effects for the previous case where the electron peak density is 10^{18}cm^{-3}. This density is 5 orders of magnitude smaller than the critical density for 46.9 nm laser radiation. The maximum absorption point is of the order 10^{-7} and as in the optical case no detector would be able to measure these small changes in intensity.

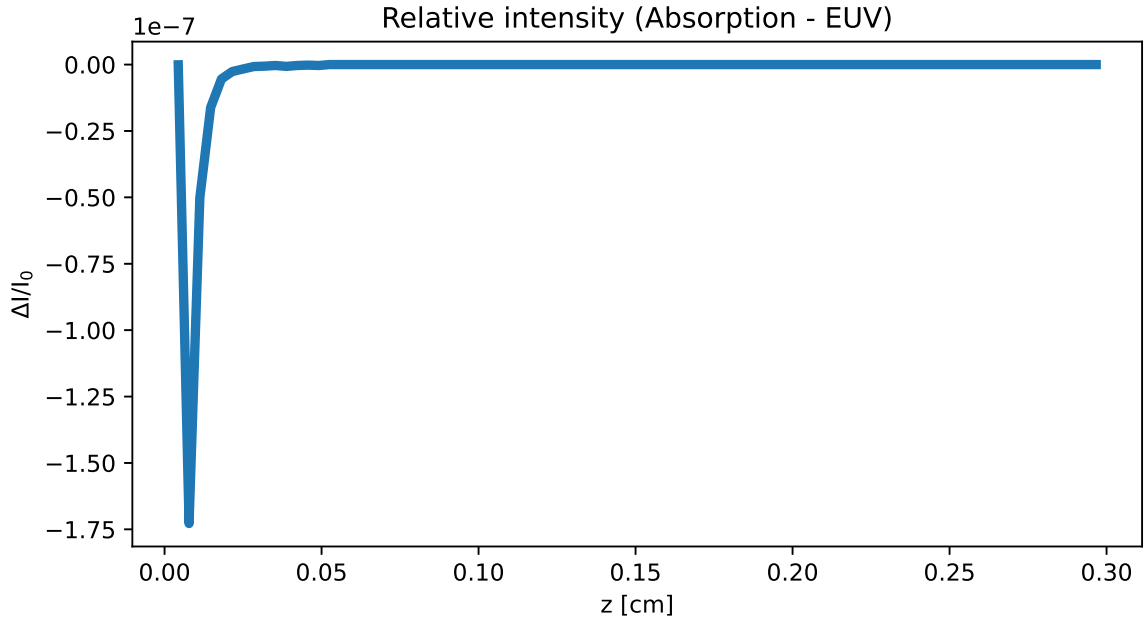

Figure 6.15: Absorption effects of the intensity of a 46.9 nm laser inside a low density aluminium plasma

Next, a high density plasma plume is considered. For this the same simulations as before is used: a 532 nm laser ablates an aluminium target with an irradiance of 3.5×10^9 Jcm^{-2}s^{-1}. The plasma plumes created were analysed using two different probing beam, a 532 nm and a 46.nm laser beam.

In the case of a 532 nm laser travels through the plasma plume and the electron density is above the critical density for small z and all of the laser is absorbed in the plasma as shown in figure 6.16. The plasma plume expands up to 0.5 mm after 7 ns of interaction and the absorption effects are high near the target surface where the electron density is high.

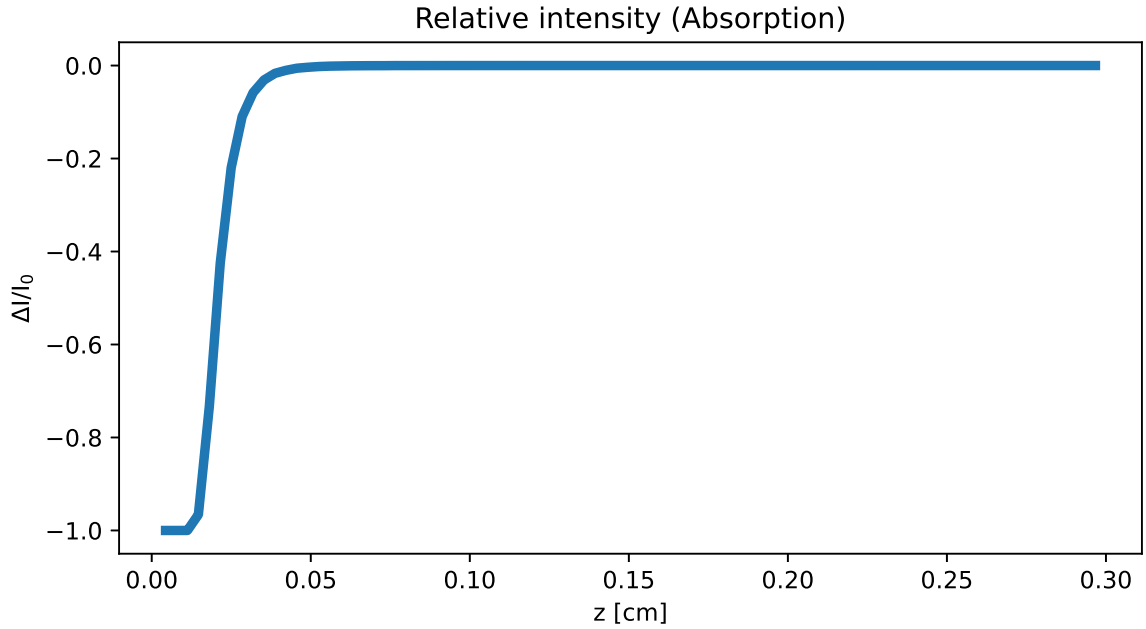

Figure 6.16: Absorption effects of the intensity of a 532 nm laser inside a high density aluminium plasma

For the case of a 46.9 nm laser in the same simulation scenario the absorption effects are smaller. In this case the percentage of the laser absorbed is smaller than the optical case. The absorption of the laser beam in the plasma are presented in figure 6.17, where the maximum value is $\sim 30\%$. In comparison to the optical case, the absorption of the beam is still big enough to be measured in a detector. The maximum absorption of the beam is located at ~ 0.2 mm, the same place as in the optical case.

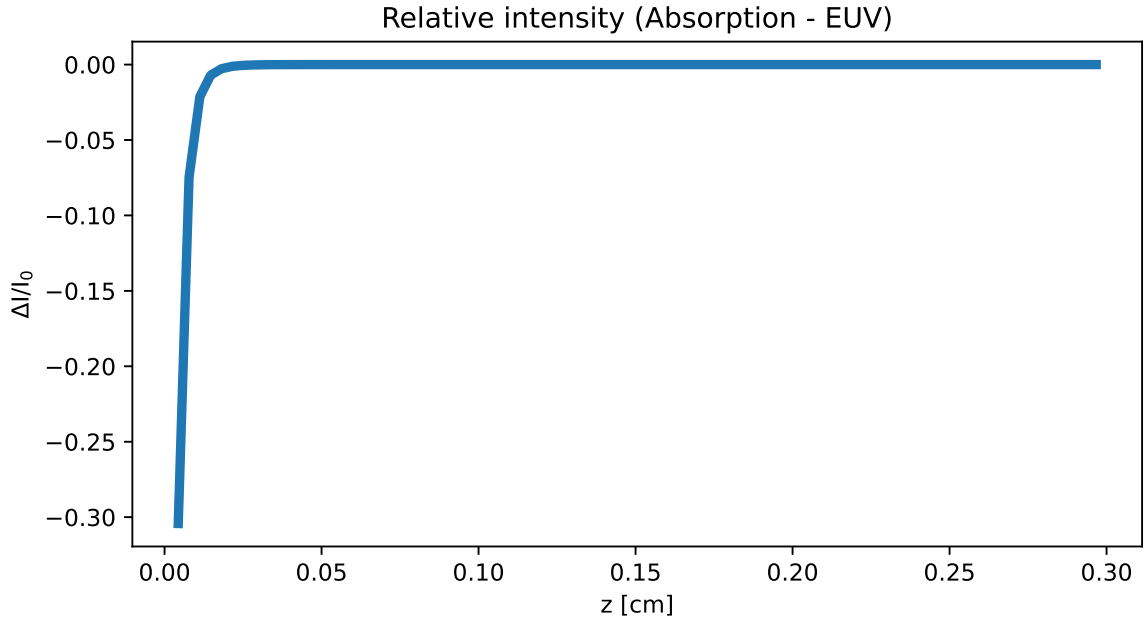

Figure 6.17: Absorption effects of the intensity of a 46.9 nm laser inside a high density aluminium plasma

These results for aluminium give a clear understanding of the effects of the plasma electron density for shadowgraphy purposes. As expected, when the backlighter laser is used to to measured a plasma close to the critical density for that probing light, the absorption effects are considerable and if the density is above the critical density all the laser beam is absorbed in the plasma. It is evident from this analysis that for higher densities a shorter wavelength backlight beam is able to penetrates the whole plasma plume, reducing the losses during this interaction. In contrast, if the backlight wavelength is considerably above the cutoff frequency, the absorption and refraction effetcs are too small to be measured, making a real world application not viable. In short, a shadowgraphy diagnostic will have a limited range of electron density that can be probed. An EUV backlighter certainly opens up the possibility to study high density plasmas, but the trade off is that it will not be able to measure lower densities, for this visible light backlighters are still needed.

6.5 Effects on different materials

The effects of refraction and absorption on different materials are presented in this section. Plasma plumes created with gold and copper targets are presented, these plumes were created using a 532 nm laser and the electron critical density corresponds to 3.53×10^{21} and 4.50×10^{23} when a 532 nm and a 46.9 nm laser are used as probing backlight respectively. The laser intensity was intended to be high enough to create a plasma plume with an electron density above the critical density.

The refraction effects followed the same characteristics as in the previous case. The plasma plume was created using a 532 nm laser with an irradiance of $5 \times 10^9\,\mathrm{Jcm^{-2}s^{-1}}$ and a spot size diameter of $1.250 \times 10^{-2}\,\mathrm{cm}$. The maximum electron density is on the target surface and it expands over 0.3 mm length. Figure 6.18 shows the refraction effect on a 532 nm laser for shadowgraphy. Again at the wavelength, the plasma density is above the critical density, which means the magnitude of the refraction in figure 6.18 is not physical.

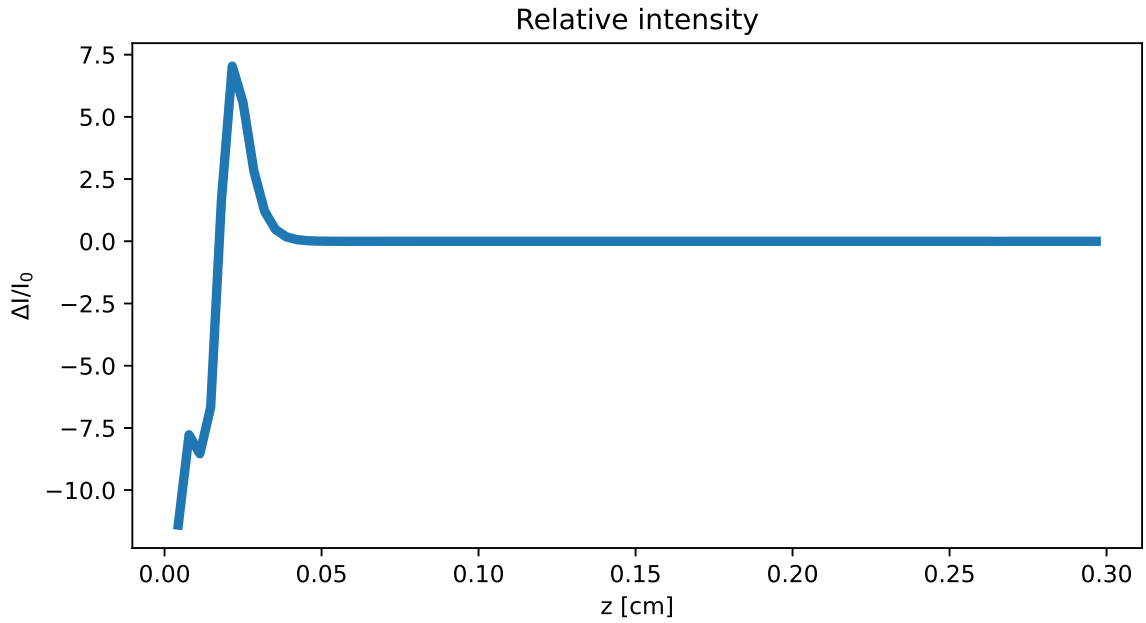

Figure 6.18: Refraction effects for a high density copper plasma using a 532 nm backlight laser

As in the previous case, when a shorter wavelength beam is used as backlight, the refraction effect is reduced considerably. In this case for the copper target, the laser parameters for ablation and a 46.9 nm probing beam it is clear that the refraction effects are considerably reduced as presented in figure 6.20. For this case, there is a change of intensity from -6% at the highest electron density point and an intensity peak of 4% produced by the deflection of the beam. These intensity changes are significant and they could be detected in a real experiment.

In general, the refraction effects on copper follow the same characteristics as alumininium, for high electron density the absorption effects are reduced considerably for the 46.9 nm probing beam. The main difference in this case is the evolution of the copper plasma plume in comparison to the aluminium target. This behaviour is expected given the different characteristics of each material. These results indicates that the material does not represent any particular challenge in shadowgraphy as long as the electron density is not above the critical density. As previously mentioned, for a 46.9 nm laser there is virtually no restriction in the possibility to measure any plasma plume as the critical electron density is close to

solid state density.

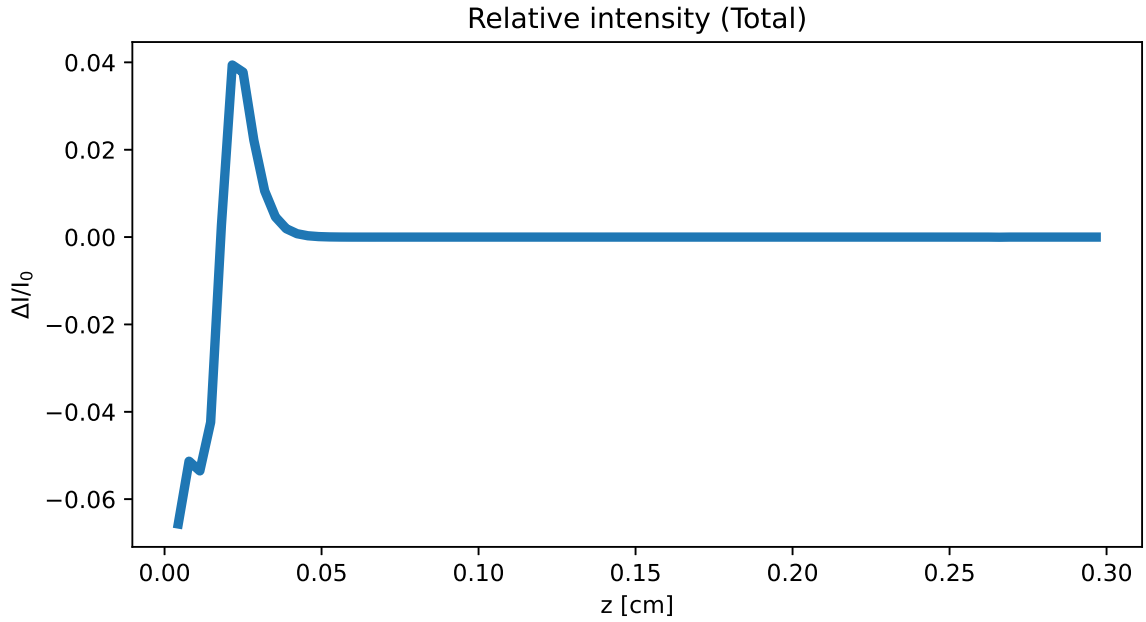

Figure 6.19: Refraction effects for a high density copper plasma using a 46.9 nm backlight laser

The absorption effects for the same probing wavelengths are presented in figure 6.20 and 6.21 for 532 nm and 46.9 nm respectively. Figure 6.20 shows that optical laser is completely absorbed in some points in the plasma plume and the absorption effect is considerably high in all the plasma plume and most of the laser beam travelling through it will be completely absorbed in the plasma.

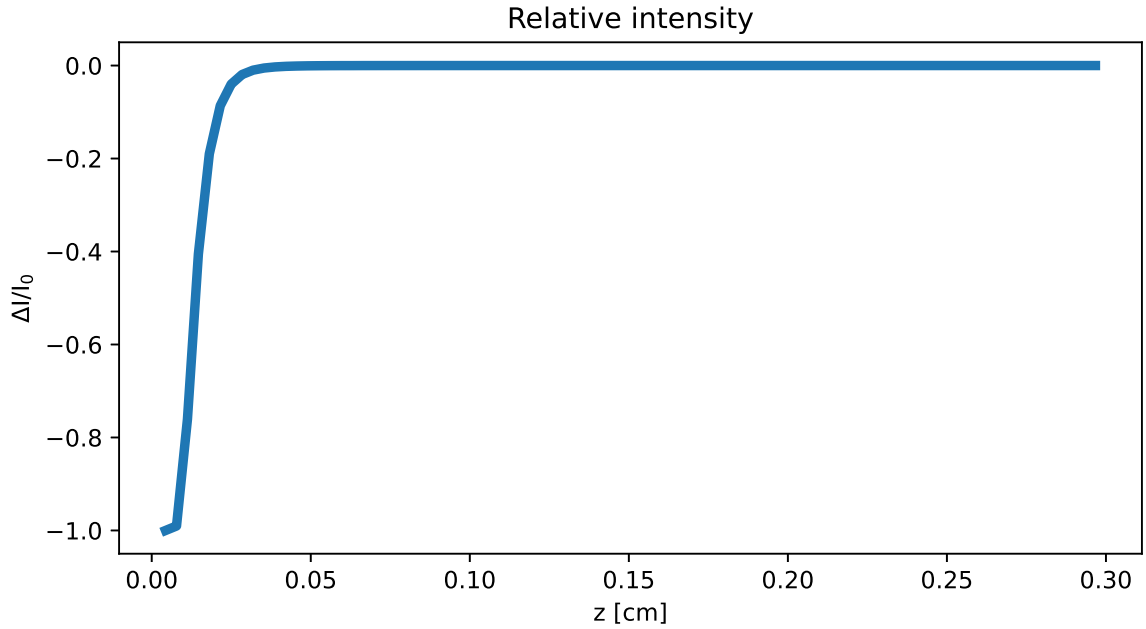

Figure 6.20: Absorption effects for a high density copper plasma using a 532 nm backlight laser

For a 46.9 nm laser, the absorption scenario is considerably better as the laser beam suffers a considerably reduction in the absorption. As expected, at this wavelength the critical density is far from the maximum electron density peak and the absorption effects are appreciable, but the maximum absorption is in the maximum electron density in the plume plume, close to the target surface and this corresponds to 3.5% absorption of the beam.

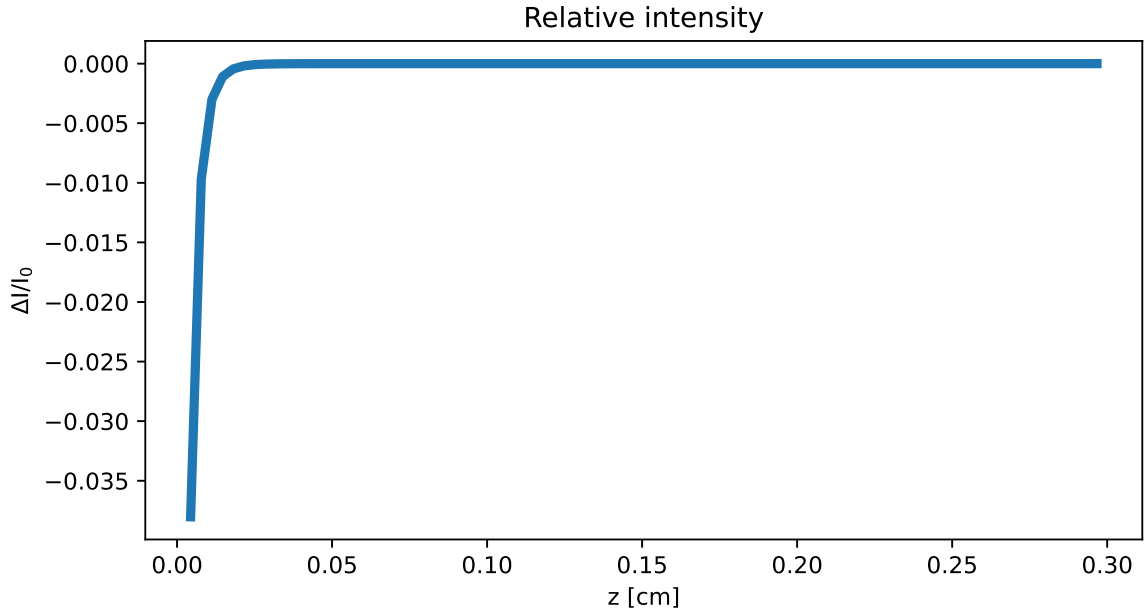

Figure 6.21: Absorption effects for a high density copper plasma using a 46.9 nm backlight laser

Based on these results, it is clear that for the case of a copper plasma plume the refraction and absorption effects produced at high density are greatly reduced in the 46.9 nm laser backlight case. This also helps to understand the clear dominance of the refraction effects as the main responsible to produces the change of intensity during the light interaction in shadowgraphy.

Another example is considered for a material with higher atomic number, in this case a gold target was used in the simulation to create a plasma plume. The laser parameters for the ablation were similar as the copper example with a 532 nm laser with an irradiance of $5 \times 10^9\,\mathrm{Jcm^{-2}s^{-1}}$ and a spot size diameter of $1.0 \times 10^{-3}\,\mathrm{cm}$. The plasma plume was also taken at 8 ns after the laser shining on the target.

Figures 6.22 and 6.23 show the refraction effects for the gold target using a 532 nm and a 46.9 nm laser as backlight. There are a few difference in comparison to the previous simulations as in the previous case the highest electron density 8×10^{20} density is located almost at the target surface but there is an important increase of the plasma plume electron density at 1.25 mm. As in the previous cases for 532 nm an important amount of the laser beam is absorbed in the plasma. For our case of study, the laser energy is not enough to create a complete plasma plume with higher density than the critical density.

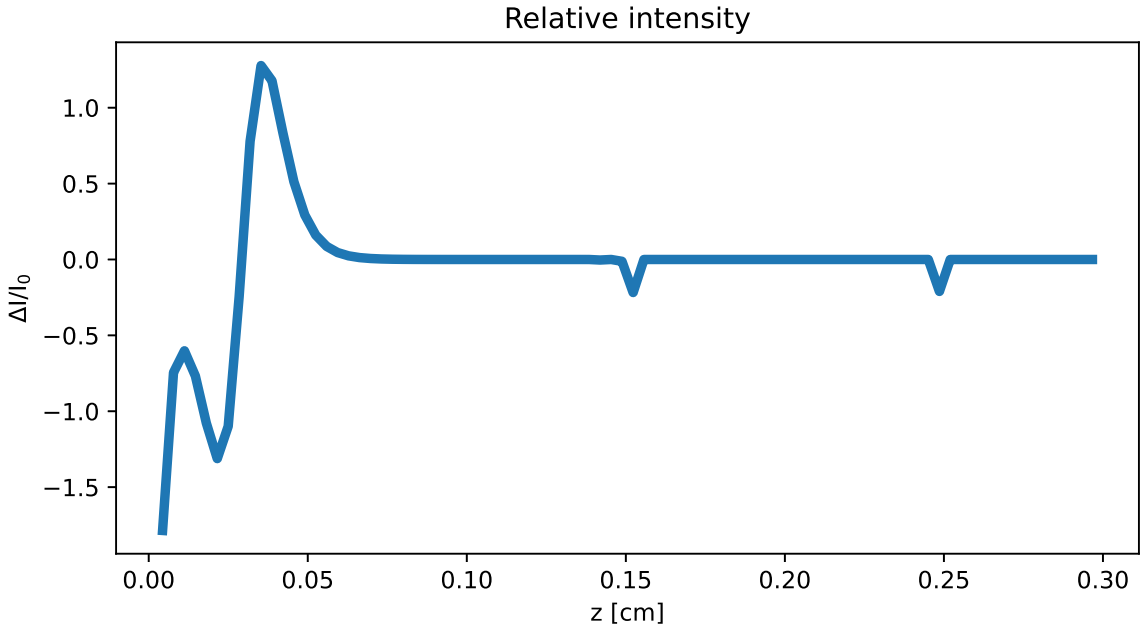

Figure 6.22: Refraction effects for a high density gold plasma using a 532 nm backlight laser

In general, the effects of refraction are also stronger for large wavelengths. Figure 6.23 shows the refraction effects in a gold plasma plume, it is clear that the change in intensity is reduced in comparison to the optical laser case. There is an interesting effect at 0.2 mm where for 532 nm there is a small intensity peak but in the case of 46.9 nm this peak is not presented. The total refraction is reduced and it has a maximum intensity change of -0.0006% at the maximum electron density peak, in this case this wavelength is not adequate for any real application as it would be out of the capabilities of any device.

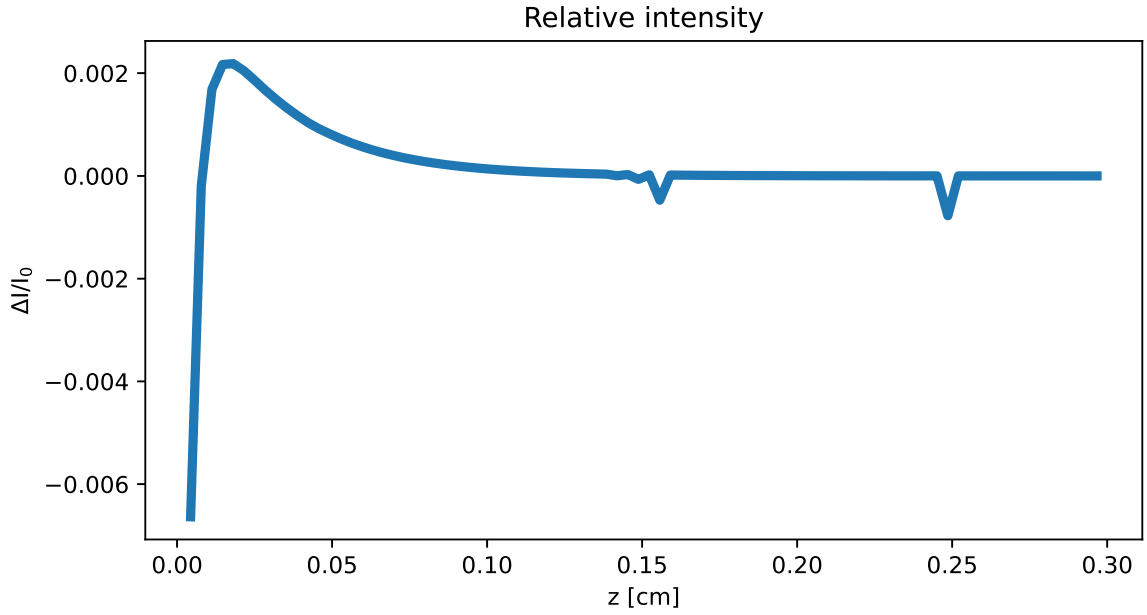

Figure 6.23: Refraction effects for a high density gold plasma using a 46.9 nm backlight laser

In figures 6.24 and 6.25 are presented the absorption effects on the same gold plasma plume. As expected, the absorption effects are considerably higher at 532 nm and the laser beam is completely absorbed near to the target surface and decrease as the electron density of the plume decreases. It is important to notice that in this case the absorption effects are bigger than the refraction effects at 46.9 nm. In general the same behaviour was observed as in the previous cases where a shorter wavelength laser has a considerably lower absorption.

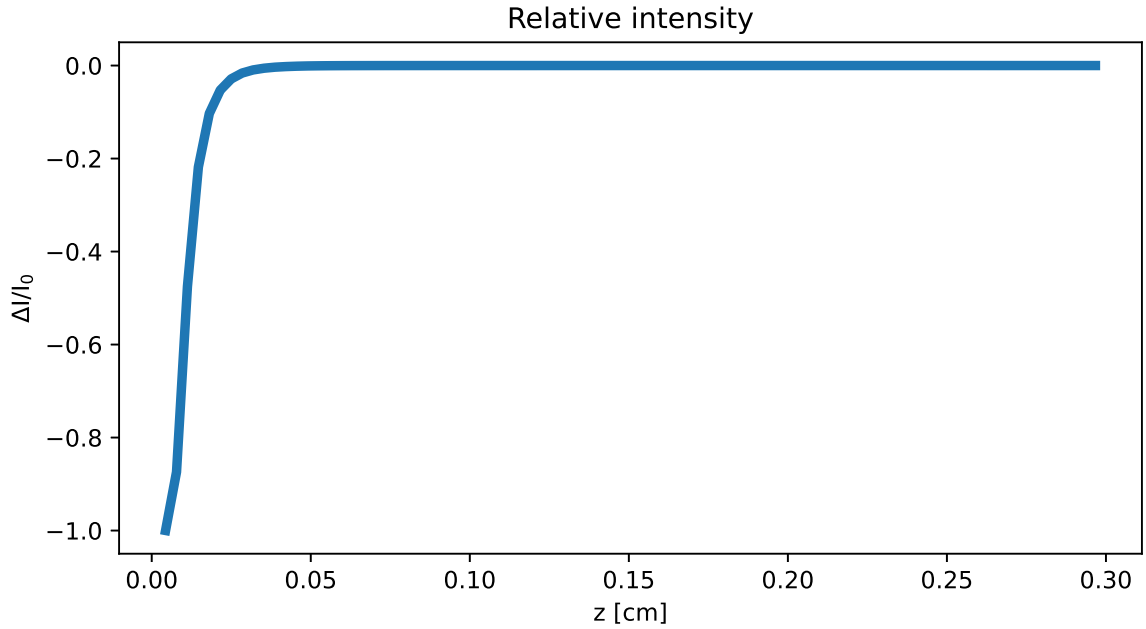

Figure 6.24: Absorption effects for a high density gold plasma using a 532 nm backlight laser

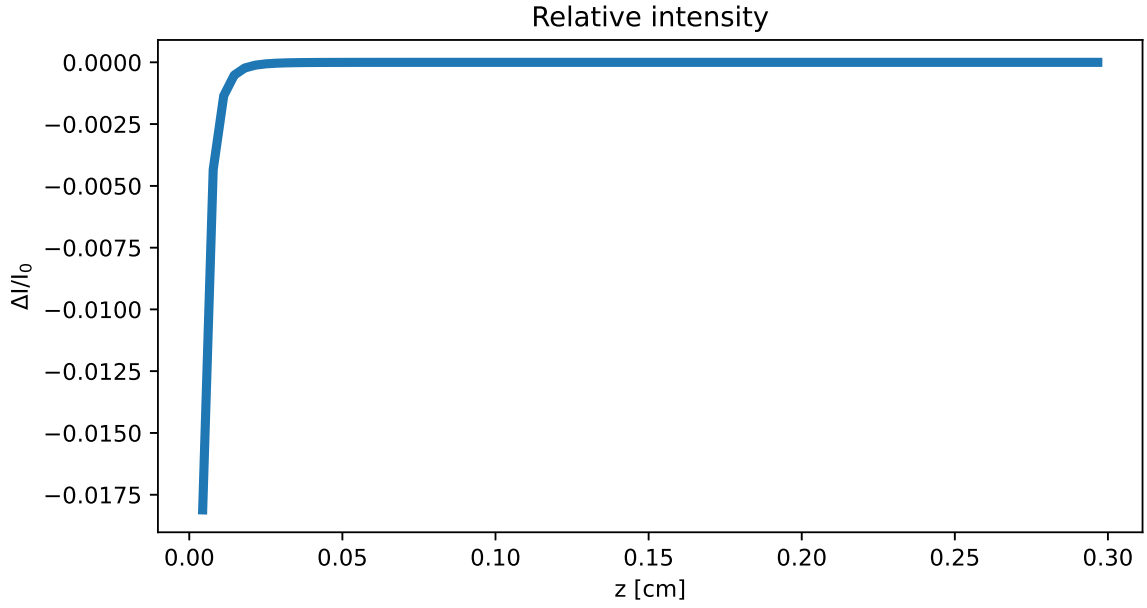

Figure 6.25: Absorption effects for a high density gold plasma using a 46.9 nm backlight laser

6.6 Conclusion

Based on all these results we can compare the main difference between the interactions of backlight laser radiation used in shadowgraphy using different wavelengths. From the previous examples it is clear that when the electron density is close or above the critical density for certain wavelength, the refraction and absorption effects are strong enough to completely bend away or absorb the incoming radiation. Because of this, using a shorter wavelength laser beam for probing the plasma, in this specific case we used 46.9 nm and it results in an adequate change of intensity for a real application during experiments where shadowgraphy is required for high density plasmas.

However, it is important to realise that a shadowgraphy diagnostic will have a limited range of electron density that can be probed. An EUV backlighter certainly opens up the possibility to study high density plasmas, but the trade off is that it will not be able to measure lower densities, for this visible light backlighters are still needed. Finally, it is also clear that for an EUV backlighter it is important to consider both the refraction and absorption effects when analysing shadowgraphy data since they have comparable magnitudes.

Chapter 7

Conclusion

This thesis presents the work focused on the understanding of the interaction of extreme ultraviolet coherent radiation with matter. Experimental and computational work were presented in this work to study and analyse the effect on different type of materials. Firstly, the comparison of the ablation process with an EUV (46.9 nm) and a visible laser sources is presented to show the key differences in ablation at different wavelength regimes. Second, the ion measurements from a time-of-flight mass spectrometer are used to understand the expansion of the plasma plume created after the interaction of an EUV laser source with different solid materials. Finally, the analysis of the interaction of laser radiation at 46.9 and 532 nm with plasma plumes created with optical radiation at different intensities using the code POLLUX.

In order to understand the ablation mechanisms that occur at different wavelength and the dominant processes, materials with different attenuation lengths were ablated using a 46.9 and a 532 nm laser sources. From these experiments, the ablation threshold at these wavelengths were obtained and they showed a clear dependence on the wavelength; at 46.9 nm the ablation threshold is smaller. The morphology of the craters created is also discussed, the experimental results show the benefits of EUV radiation in comparison to visible radiation. The craters created with the EUV laser source are smoother and deeper in comparison with the visible laser source. The laser sources used were tuned to have similar intensities in both experiments and the materials have comparable attenuation lengths to make the experiments comparable. The shapes of the craters were compared with previous theoretical work to model the shape based on ablation laws for visible laser. It was found that these laws are still valid for both cases independently of the wavelength. Furthermore, based on the evidence of the craters shape for EUV, a reconstruction of the laser pulse shapes were computed to understand the spatial energy distribution. Finally, the ablation thresholds for all the materials ablated were calculated. These experimental results for these thresholds were compared with previous work at visible wavelength and the results were similar to these works and for EUV it is presented new ablation threshold results.

The incorporation of EUV sources as an ionisation source is still a relevant area of

study. The characteristics of the ablation profiles is still an active research field as previously mentioned. Moreover, the characteristics of the plasma plume created with EUV radiation is also an interesting research opportunity. Using the time-of-flight mass spectrometer with EUV light at Colorado State University were measured the number of ions created in different materials and based on these results, the temperature of the plasma were calculated using a Coronal model approximation. The temperatures calculated for the plasma plumes seem reasonable for the conditions of the laser. It was observed that for the elements with a higher atomic number reached higher temperatures. These results are in line with a previous work that described the temperature of the plasma plume created for different materials [91].

In order to understand the plasma plume expansion process and try to model the experimental results obtained, ideal expansion processes were modelled to give an approximation that match the experimental ratio for the number of particles measured in the TOF device. The temperatures modelled were too high given the parameters of the EUV laser source and it will not be possible to reach these temperatures in these conditions. It is important to note that the temperatures modelled are temperatures of an equivalent plasma in steady-state coronal equilibrium. In reality, there is a plasma with time-varying properties arriving at the grid position. Because the measurement is effectively time-integrated, the measured ion ratio will represent an effective temperature, not necessarily a true representation of the time-dependent plasma plume. In addition, the measured ions might be dominated by the most energetic ions created after the laser interaction, so-called fast ions. This could lead to an overestimate of the temperature, this could also lead to the mismatching of the temperatures measured based on the experimental ion ratios and the calculated with the expansion models.

Lastly, the refraction and absorption on different plasma plumes simulated with different target materials were analysed and studied. The creation of these plasma plumes were computed with POLLUX. The results showed the percentage of absorption on overdense and underdense plasma for visible light and how this affect EUV radiation. These results helped to understand the kind of results expected in diagnostic techniques such as shadowgraphy.

The absorption and refraction effects in plasma are directly related with the wavelength of the incident radiation and these are considerably higher when the plasma density is close to the critical density for such wavelength. From these result it is clear that EUV light is virtually able to penetrate to any plasma plume, in this particular case where 46.9 nm were analysed the critical density is above solid density. For overdense plasma at 532 nm, most part of the incoming radiation is absorbed in the plasma and important part of is refracted. The combined effect of refraction and absorption for a probing beam at 532 nm for an overdense plasma blocked all the beam, in contrast EUV radiation is affected below 10$ combining refraction and absorption. Nevertheless, for underdense plasma cases the use of EUV beams to probe plasma results impractical as the effects for absorption and refraction are below 5% which results impractical in real experiments. In general, EUV laser are ideal for probing techniques for high density plasmas as they can travel virtually any

plasma plume.

This work has presented an extensive analysis of different experiments of EUV interacting with matter. The understanding of the underlying process during ablation or laser-plasma interactions were studied in this work. There are some similarities with visible radiation interaction with matter as it was showed with the ablation experiments. The ablation laws for visible light seem to be still valid for EUV radiation as it follows the same law. For the expansion modelling it seems there are still some pieces missing to completely understand the effects for the creation of fast ions that seem to be an important part with EUV. Finally, EUV is undoubtedly the best laser source for probing high density plasmas but also at the moment there not exist high repetition EUV lasers as fast as visible wavelength lasers. This helps to understand the benefits of EUV light over visible light in particular cases as ablation or probing but also ponder the application of it in experiments as it results nowadays have small and reliable EUV laser sources.

Future work on the experimental design and setup for shadowgraphy is being considered to compare with the simulations presented. The TOF device offers the option to analyse the material through mass spectrometry, a more detailed model for the plasma expansion including the interaction of EUV radiation and its particular processes such as direct photoionisation could be an state-of-the-art tool in plasma diagnostic techniques.

Appendix A

Appendix

A.1 Baseline

```
import os
import numpy as np
import matplotlib.pyplot as plt
import peakutils
from scipy import sparse
from scipy.sparse.linalg import spsolve
from scipy import integrate


def baseline_als(y, lam, p, niter=10):
  L = len(y)
  D = sparse.diags([1,-2,1],[0,-1,-2], shape=(L,L-2))
  w = np.ones(L)
  for i in range(niter):
    W = sparse.spdiags(w, 0, L, L)
    Z = W + lam * D.dot(D.transpose())
    z = spsolve(Z, w*y)
    w = p * (y > z) + (1-p) * (y < z)
  return z
```

A.2 Analysis

```
#!/usr/bin/env python
# coding: utf-8

# In[1]:


import matplotlib.pyplot as plt
import numpy as np
from scipy.optimize import curve_fit

```

```
11
12 # Import all the function required for the curve fitting. In this case the
       gaussian curve.
13
14 # In[2]:
15
16
17 def gaussian(x, *params):
18     A = params[0]
19     B = params[1]
20     C = params[2]
21     D = params[3]
22     return A + B*np.exp(-(x-C)**2/(2*D*D))
23
24
25 # In[3]:
26
27
28 def quadratic(x, *params):
29     A = params[0]
30     B = params[1]
31     C = params[2]
32     return A*x*x+B*x+C
33
34
35 # Next line opens the data file and reads the first line.
36
37 # In[4]:
38
39
40 File = open("Cu_27_20shots_run3_190718_0_00002.dat", "r")
41 line = File.readline()
42
43
44 # I initialised 5 set of (x,y) columns, one for each profile.
45
46 # In[5]:
47
48
49 x1 = []
50 x2 = []
51 x3 = []
52 x4 = []
53 x5 = []
54 y1 = []
55 y2 = []
56 y3 = []
57 y4 = []
58 y5 = []
```

```
59
60
61 # This for loop reads every line in the dataset and appends line by line the
       value of each column. In the dataset the columns are separated by
       semicolons.
62
63 # In[6]:
64
65
66 for line in File:
67     words = line.split(";")
68     x1.append(float(words[0]))
69     y1.append(float(words[1]))
70     x2.append(float(words[2]))
71     y2.append(float(words[3]))
72     x3.append(float(words[4]))
73     y3.append(float(words[5]))
74     x4.append(float(words[6]))
75     y4.append(float(words[7]))
76     x5.append(float(words[8]))
77     y5.append(float(words[9]))
78
79
80 # It's important to close the file with the dataset. Next command does that.
81
82 # In[7]:
83
84
85 File.close()
86
87
88 # I initialised other set of columns to store the mean value of the dataset.
89
90 # In[8]:
91
92
93 x = []
94 y = []
95
96
97 # This for loop calculates the mean value of all the x-s and y-s in the
       profiles.
98
99 # In[9]:
100
101
102 for i in range(len(x1)):
103     x.append(float((x1[i]+x2[i]+x3[i]+x4[i]+x5[i])/5.0))
104     y.append(float((y1[i]+y2[i]+y3[i]+y4[i]+y5[i])/5.0))
```

```
105
106
107 # This line calculates the best parameters to fit a gaussian in the data. The
        initial guesses p0 are given lookin the values very roughly in the plot.
108
109 # In[10]:
110
111
112 popt,pcov = curve_fit(gaussian,x,y, p0 = [9e-7,-3.5e-6, 9e-7, 1e-5])
113 perr = np.sqrt(np.diag(pcov))
114
115
116 # yg is the y-value of the gaussian calculated using the popt parameters.
117
118 # In[11]:
119
120
121 yg = gaussian(x, *popt)
122 print(popt[1],perr[1])
123
124
125 # In[12]:
126
127
128 plt.figure(figsize=(14.22,8))
129 plt.rc('font', family='serif',  size='20')
130 plt.rc('xtick', labelsize='small')
131 plt.rc('ytick', labelsize='small')
132 plt.ticklabel_format(style='scientific',scilimits=(0,0))
133 plt.title('Copper/Gaussian')
134 plt.xlabel("Position [m]")
135 plt.ylabel("Depth [m]")
136
137 plt.plot(x,y, lw='3')
138 plt.plot(x,yg, ls='dashed',lw='3')
139 plt.show()
140
141
142 # In[13]:
143
144
145 y2 = y[70:]
146 y2 = y2[:-45]
147
148
149 # In[14]:
150
151
152 x2 = x[70:]
```

```
x2 = x2[:-45]


# In[15]:


z = np.polyfit(x2,y2,2)


# In[16]:


print(z)


# In[17]:


p = np.poly1d(z)


# In[18]:


plt.figure(figsize=(14.22,8))
plt.rc('font', family='serif',  size='40')
plt.rc('xtick', labelsize='small')
plt.rc('ytick', labelsize='small')
plt.ticklabel_format(style='scientific',scilimits=(0,0))
plt.title('Copper 20 shots')
plt.xlabel("Position [m]")
plt.ylabel("Depth [m]")

plt.plot(x,y,lw='3',label='Experimental data')
plt.plot(x2,p(x2),lw='3',ls='dashed',label='Quadratic regression')
plt.legend(loc='lower left', shadow=True, fontsize='20')
plt.tight_layout()
plt.savefig('Cu_Parabolic_20.eps', dpi=600, facecolor='w', edgecolor='w',
    orientation='portrait')

plt.show()


# In[19]:


popt,pcov = curve_fit(quadratic,x,y, p0 = [9e-7,-3.5e-6, 9e-7])
perr = np.sqrt(np.diag(pcov))

```

```
201
202 # In[20]:
203
204
205 print(perr)
```

Bibliography

[1] J. J. Rocca, F. G. Tomasel, M. C. Marconi, V. N. Shlyaptsev, J. L. Chilla, B. T. Szapiro, and G. Giudice, "Discharge-pumped soft-x-ray laser in neon-like argon," *Physics of Plasmas*, vol. 2, no. 6, pp. 2547–2554, 1995.

[2] M. N. Ashfold, F. Claeyssens, G. M. Fuge, and S. J. Henley, "Pulsed laser ablation and deposition of thin films," *Chemical Society Reviews*, vol. 33, no. 1, pp. 23–31, 2004.

[3] A. Gopal, M. Tatarakis, and S. Minardi, "Quantitative two-dimensional shadowgraphic method for high-sensitivity density measurement of under-critical laser plasmas," *Optics Letters, Vol. 32, Issue 10, pp. 1238-1240*, vol. 32, pp. 1238–1240, may 2007.

[4] "Department of physics, *Extreme ultra-violet laser physics and applications.*" `https://www.york.ac.uk/physics/ypi/research/matter-at-the-extremes/euvlasers/extremeultra-violetlaserphysicsandapplications/`. Accessed: 25 July 2022.

[5] J. Schmit and A. Pakuła, *White Light Interferometry*, pp. 421–467. Cham: Springer International Publishing, 2019.

[6] D. Meehan, *Plasma enhanced pulsed laser deposition: A study of laser produced and radio frequency plasmas, and deposited films.* PhD thesis, University of York, 2019.

[7] D. Burg and J. H. Ausubel, "Moore's law revisited through intel chip density," *PloS one*, vol. 16, no. 8, p. e0256245, 2021.

[8] A. H. Boozer, *Physics of magnetically confined plasmas.* APS, 2004.

[9] J. H. Nuckolls *et al.*, "Early steps toward inertial fusion energy (ife)(1952 to 1962)," tech. rep., Lawrence Livermore National Lab., CA (United States), 1998.

[10] R. Toschi, "Nuclear fusion, an energy source," *Fusion Technology 1996*, pp. 1–8, jan 1997.

[11] A. Casner, C. Mailliet, G. Rigon, S. F. Khan, D. Martinez, B. Albertazzi, T. Michel, T. Sano, Y. Sakawa, P. Tzeferacos, D. Lamb, S. Liberatore, N. Izumi, D. Kalantar, P. Di Nicola, J. M. Di Nicola, E. Le Bel, I. Igumenshchev, V. Tikhonchuk, B. A.

Remington, J. Ballet, E. Falize, L. Masse, V. A. Smalyuk, and M. Koenig, "From ICF to laboratory astrophysics: ablative and classical Rayleigh–Taylor instability experiments in turbulent-like regimes," *Nuclear Fusion*, vol. 59, p. 032002, dec 2018.

[12] R. Craxton, K. Anderson, T. Boehly, V. Goncharov, D. Harding, J. Knauer, R. McCrory, P. McKenty, D. Meyerhofer, J. Myatt, *et al.*, "Direct-drive inertial confinement fusion: A review," *Physics of Plasmas*, vol. 22, no. 11, p. 110501, 2015.

[13] J. Lindl, "Development of the indirect-drive approach to inertial confinement fusion and the target physics basis for ignition and gain," *Physics of Plasmas*, vol. 2, p. 3933, jun 1998.

[14] J. Filevich, J. J. Rocca, J. L. A. Chilla, K. Kanizay, and M. C. Marconi, "Dense plasma diagnostics with an amplitude-division soft-x-ray laser interferometer based on diffraction gratings," *Optics Letters, Vol. 25, Issue 5, pp. 356-358*, vol. 25, pp. 356–358, mar 2000.

[15] K. Tiedtke, A. Azima, N. von Bargen, L. Bittner, S. Bonfigt, S. Düsterer, B. Faatz, U. Frühling, M. Gensch, C. Gerth, N Guerassimova, U. Hahn, T. Hans, M. Hesse, K. Honkavaar, U. Jastrow, P. Juranic, S. Kapitzki, B. Keitel, T. Kracht, M Kuhlmann, W. B. Li, M. Martins, T. Núñez, E. Plönjes, H. Redlin, E. L. Saldin, E. A. Schneidmiller, J. R. Schneider, S Schreiber, N. Stojanovic, F. Tavella, S. Toleikis, R. Treusch, H. Weigelt, M. Wellhöfer, H. Wabnitz, M. V. Yurkov, and J Feldhaus, "The soft x-ray free-electron laser FLASH at DESY: beamlines, diagnostics and end-stations," *New Journal of Physics*, vol. 11, no. 2, p. 23029, 2009.

[16] J. J. Rocca, "Table-top soft x-ray lasers," *Review of Scientific Instruments*, vol. 70, no. 10, pp. 3799–3827, 1999.

[17] A. M. Kondratenko and E. L. Saldin, "Generation of coherent radiation by a relativistic electron beam in an ondulator," *Particle Accelerators*, vol. 10, pp. 207–216, 1980.

[18] S. V. Milton, E. Gluskin, N. D. Arnold, C. Benson, W. Berg, S. G. Biedron, M. Borland, Y. C. Chae, R. J. Dejus, P. K. D. Hartog, B. Deriy, M. Erdmann, Y. I. Eidelman, M. W. Hahne, Z. Huang, K. J. Kim, J. W. Lewellen, Y. Li, A. H. Lumpkin, O. Makarov, E. R. Moog, A. Nassiri, V. Sajaev, R. Soliday, B. J. Tieman, E. M. Trakhtenberg, G. Travish, I. B. Vasserman, N. A. Vinokurov, X. J. Wang, G. Wiemerslage, and B. X. Yang, "Exponential gain and saturation of a self-amplified spontaneous emission free-electron laser," *Science*, vol. 292, pp. 2037–2041, 6 2001.

[19] B. W. J. McNeil and N. R. Thompson, "X-ray free-electron lasers," *Nature Photonics*, vol. 4, no. 12, pp. 814–821, 2010.

[20] R. C. Elton, *X-ray lasers*. Academic Press, 1990.

[21] G. Tomassetti, A. Ritucci, A. Reale, L. Palladino, L. Reale, S. V. Kukhlevsky, F. Flora, L. Mezi, J. Kaiser, A. Faenov, and T. Pikuz, "Capillary discharge soft X-ray lasing in Ne-like Ar pumped by long current pulses," *European Physical Journal D*, vol. 19, no. 1, pp. 73–77, 2002.

[22] M. Shuker, A. Ben-Kish, R. A. Nemirovsky, A. Fisher, and A. Ron, "The effects of the prepulse on capillary discharge extreme ultraviolet laser," *Physics of Plasmas*, vol. 13, no. 1, pp. 1–4, 2006.

[23] J. J. Rocca, V. Shlyaptsev, F. G. Tomasel, O. D. Cortzar, D. Hartshorn, and J. L. Chilla, "Demonstration of a discharge pumped table-top soft-x-ray laser," *Physical Review Letters*, vol. 73, no. 16, pp. 2192–2195, 1994.

[24] J. J. Rocca, O. D. Cortzar, B. Szapiro, K. Floyd, and F. G. Tomasel, "Fast-discharge excitation of hot capillary plasmas for soft-x-ray amplifiers," *Physical Review E*, vol. 47, no. 2, pp. 1299–1304, 1993.

[25] J. C. Miller, "A brief history of laser ablation," *AIP Conference Proceedings*, vol. 288, p. 619, 5 2008.

[26] F. Barkusky, C. Peth, A. Bayer, and K. Mann, "Direct photo-etching of poly(methyl methacrylate) using focused extreme ultraviolet radiation from a table-top laser-induced plasma source," *Journal of Applied Physics*, 2007.

[27] L. Juha, M. Bittner, D. Chvostova, J. Krasa, Z. Otcenasek, A. R. Präg, J. Ullschmied, Z. Pientka, J. Krzywinski, J. B. Pelka, A. Wawro, M. E. Grisham, G. Vaschenko, C. S. Menoni, and J. J. Rocca, "Ablation of organic polymers by 46.9-nm-laser radiation," *Applied Physics Letters*, vol. 86, no. 3, pp. 1–3, 2005.

[28] E. G. Gamaly, A. V. Rode, B. Luther-Davies, and V. T. Tikhonchuk, "Ablation of solids by femtosecond lasers: Ablation mechanism and ablation thresholds for metals and dielectrics," *Physics of Plasmas*, vol. 9, p. 949, 2 2002.

[29] R. F. Haglund, "2. Mechanisms of Laser-Induced Desorption and Ablation," *Experimental Methods in the Physical Sciences*, 1997.

[30] R. F. Haglund, "Microscopic and mesoscopic aspects of laser-induced desorption and ablation," in *Laser Ablation* (E. FOGARASSY, D. GEOHEGAN, and M. STUKE, eds.), European Materials Research Society Symposia Proceedings, pp. 1–13, Oxford: Elsevier, 1996.

[31] A. Kon, H. Kinoshita, K. Mikami, M. Nishikino, M. Ishino, N. Hasegawa, S. Owada, S. Motokoshi, T.-H. Dinh, and Y. Inubushi, "Laser-induced damage thresholds and mechanism of silica glass induced by ultra-short soft x-ray laser pulse irradiation," *Optics Letters, Vol. 45, Issue 8, pp. 2435-2438*, vol. 45, pp. 2435–2438, apr 2020.

[32] B. D. Guenther, *Modern Optics Simplified*. Oxford University Press, 09 2019.

[33] S. Rajendiran, *Plasma enhanced pulsed laser deposition*. PhD thesis, University of York, 2017.

[34] G. Koren, A. Gupta, R. Baseman, M. Lutwyche, and R. Laibowitz, "Laser wavelength dependent properties of yba2cu3o7- δ thin films deposited by laser ablation," *Applied Physics Letters*, vol. 55, no. 23, pp. 2450–2452, 1989.

[35] J. Hoffman, J. Chrzanowska, S. Kucharski, T. Moscicki, I. N. Mihailescu, C. Ristoscu, and Z. Szymanski, "The effect of laser wavelength on the ablation rate of carbon," *Applied Physics A*, vol. 117, no. 1, pp. 395–400, 2014.

[36] A. K. Rossall, V. Aslanyan, G. J. Tallents, I. Kuznetsov, J. J. Rocca, and C. S. Menoni, "Ablation of submicrometer holes using an extreme-ultraviolet laser," *Physical Review Applied*, vol. 3, no. 6, 2015.

[37] V. Aslanyan, I. Kuznetsov, H. Bravo, M. R. Woolston, A. K. Rossall, C. S. Menoni, J. J. Rocca, and G. J. Tallents, "Ablation and transmission of thin solid targets irradiated by intense extreme ultraviolet laser radiation," *APL Photonics*, vol. 1, p. 066101, sep 2016.

[38] L. Wilson, G. Tallents, J. Pasley, D. Whittaker, S. Rose, O. Guilbaud, K. Cassou, S. Kazamias, S. Daboussi, M. Pittman, O. Delmas, J. Demailly, O. Neveu, and D. Ros, "Energy transport in short-pulse-laser-heated targets measured using extreme ultraviolet laser backlighting," *Physical Review E - Statistical, Nonlinear, and Soft Matter Physics*, vol. 86, no. 2, 2012.

[39] A. Hassanein, V. Sizyuk, T. Sizyuk, and S. Harilal, "Effects of plasma spatial profile on conversion efficiency of laser produced plasma sources for EUV lithography," in *Metrology, Inspection, and Process Control for Microlithography XXIII*, 2009.

[40] R. Moors, V. Banine, G. Swinkels, and F. Wortel, "Extreme-ultraviolet source specifications: tradeoffs and requirements," *Journal of Micro/Nanolithography, MEMS, and MOEMS*, 2012.

[41] T. Yamazaki, H. Nakarai, T. Abe, K. M. Nowak, Y. Kawasuji, T. Okamoto, H. Tanaka, Y. Watanabe, T. Hori, T. Kodama, T. Yamagida, Y. Shiraishi, T. Saitou, and H. Mizoguchi, "Development of 250W EUV light source for HVM lithography," in *China Semiconductor Technology International Conference 2017, CSTIC 2017*, 2017.

[42] S. Shwartz, M. Fuchs, J. B. Hastings, Y. Inubushi, T. Ishikawa, T. Katayama, D. A. Reis, T. Sato, K. Tono, M. Yabashi, S. Yudovich, and S. E. Harris, "X-ray second harmonic generation," *Phys. Rev. Lett.*, vol. 112, p. 163901, Apr 2014.

[43] G. Doumy, C. Roedig, S.-K. Son, C. I. Blaga, A. D. DiChiara, R. Santra, N. Berrah, C. Bostedt, J. D. Bozek, P. H. Bucksbaum, J. P. Cryan, L. Fang, S. Ghimire, J. M. Glownia, M. Hoener, E. P. Kanter, B. Krässig, M. Kuebel, M. Messerschmidt, G. G. Paulus, D. A. Reis, N. Rohringer, L. Young, P. Agostini, and L. F. DiMauro, "Nonlinear atomic response to intense ultrashort x rays," *Phys. Rev. Lett.*, vol. 106, p. 083002, Feb 2011.

[44] Y. Murti and C. Vijayan, *Essentials of Nonlinear Optics*. John Wiley & Sons, Ltd, 2014.

[45] T. Shibuya, K. Sakaue, H. Ogawa, H. Ogawa, D. Satoh, D. Satoh, T.-H. Dinh, M. Ishino, M. Tanaka, M. Tanaka, M. Washio, T. Higashiguchi, M. Nishikino, A. Kon, A. Kon, Y. Kubota, Y. Kubota, Y. Inubushi, Y. Inubushi, S. Owada, S. Owada, Y. Kobayashi, R. Kuroda, and R. Kuroda, "Independent contribution of optical attenuation length in ultrafast laser-induced structural change," *Optics Express, Vol. 29, Issue 21, pp. 33121-33133*, vol. 29, pp. 33121–33133, 10 2021.

[46] N. Rohringer and R. Santra, "X-ray nonlinear optical processes using a self-amplified spontaneous emission free-electron laser," *Phys. Rev. A*, vol. 76, p. 033416, Sep 2007.

[47] R. K. Singh and J. Narayan, "Pulsed-laser evaporation technique for deposition of thin films: Physics and theoretical model," *Physical Review B*, 1990.

[48] S. I. Anisimov, B. S. Luk'yanchuk, and A. Luches, "An analytical model for three-dimensional laser plume expansion into vacuum in hydrodynamic regime," *Applied Surface Science*, 1996.

[49] G. J. Tallents, *An Introduction to the Atomic and Radiation Physics of Plasmas*. Cambridge University Press, feb 2018.

[50] I. H. Hutchinson, *Principles of Plasma Diagnostics*. Cambridge University Press, 2 ed., 2002.

[51] A. M. Baptista Boné, *Shadowgraphy based diagnostics for laser-plasma interactions*. PhD thesis, Instituto Superior Técnico da Universidade de Lisboa, 2015.

[52] K. Lan, E. Fill, and J. Meyer-Ter-Vehn, "Photopumping of xuv lasers by xfel radiation," *Laser and Particle Beams*, vol. 22, pp. 261–266, 9 2004.

[53] C. Gong, *Optical Probing of CO2 Laser-Plasma Interactions at Near Critical Density*. PhD thesis, University of California, Los Angeles, 2015.

[54] G. Binnig, C. F. Quate, and C. Gerber, "Atomic Force Microscope," *Physical Review Letters*, vol. 56, p. 930, mar 1986.

[55] R. Asmatulu and W. S. Khan, "Characterization of electrospun nanofibers," *Synthesis and Applications of Electrospun Nanofibers*, pp. 257–281, jan 2019.

[56] P. Eaton, *Atomic force microscopy [electronic resource]*. Oxford: Oxford University Press, 2010.

[57] Y. Denisyuk, "Photographic Reconstruction of the Optical Properties of an Object in Its Own Scattered Radiation Field," *undefined*, 1962.

[58] Y. N. Denisyuk, Denisyuk, and Y. N., "On the Reproduction of the Optical Properties of an Object by the Wave Field of Its Scattered Radiation. II," *OptSp*, vol. 18, p. 152, 1965.

[59] E. N. Leith and G. J. Swanson, "Achromatic interferometers for white light optical processing and holography," *Applied Optics, Vol. 19, Issue 4, pp. 638-644*, vol. 19, pp. 638–644, feb 1980.

[60] J. Schmit, "White-light interference 3d microscopes," *Handbook of optical dimensional metrology*, vol. 10, 2013.

[61] J. T. M. F.R.S., "XLVII. On rays of positive electricity," *https://doi.org/10.1080/14786440709463633*, vol. 13, pp. 561–575, may 2009.

[62] F. W. Aston, *Mass spectra and isotopes*. Edward Arnold London, 1942.

[63] S. W. E *Physical Review, Vol. 69, Issue 11-12*, 1946.

[64] G. J. Pert, "Two-dimensional hydrodynamic models of laser-produced plasmas," *Journal of Plasma Physics*, vol. 41, no. 2, p. 263–280, 1989.

[65] J. P. Boris and D. L. Book, "Flux-corrected transport. III. Minimal-error FCT algorithms," *Journal of Computational Physics*, vol. 20, pp. 397–431, apr 1976.

[66] S. Thompson and H. Lauson, "Improvements in the chart d radiation-hydrodynamic code iii: Revised analytic equations of state," tech. rep., Sandia Labs., 1974.

[67] R. Latter, "Temperature Behavior of the Thomas-Fermi Statistical Model for Atoms," *Physical Review*, vol. 99, p. 1854, sep 1955.

[68] H. K. Chung, M. H. Chen, W. L. Morgan, Y. Ralchenko, and R. W. Lee, "FLYCHK: Generalized population kinetics and spectral model for rapid spectroscopic analysis for all elements," *High Energy Density Physics*, vol. 1, pp. 3–12, dec 2005.

[69] B. N. Chichkov, C. Momma, S. Nolte, F. Von Alvensleben, and A. Tünnermann, "Femtosecond, picosecond and nanosecond laser ablation of solids," *Applied Physics A: Materials Science and Processing*, 1996.

[70] F. Barkusky, A. Bayer, S. Döring, P. Grossmann, and K. Mann, "Damage threshold measurements on EUV optics using focused radiation from a table-top laser produced plasma source," *Optics Express*, vol. 18, no. 5, pp. 4346–4355, 2010.

[71] A. Spiro, M. Lowe, and G. Pasmanik, "Drilling rate of five metals with picosecond laser pulses at 355, 532, and 1064 nm," *Applied Physics A*, vol. 107, pp. 801–808, 2012.

[72] J. Chalupský, L. Juha, J. Kuba, J. Cihelka, V. Hájková, S. Koptyaev, J. Krása, A. Velyhan, M. Bergh, C. Caleman, J. Hajdu, R. M. Bionta, H. Chapman, S. P. Hau-Riege, R. A. London, M. Jurek, J. Krzywinski, R. Nietubyc, J. B. Pelka, R. Sobierajski, J. Meyer-ter Vehn, A. Tronnier, K. Sokolowski-Tinten, N. Stojanovic, K. Tiedtke, S. Toleikis, T. Tschentscher, H. Wabnitz, and U. Zastrau, "Characteristics of focused soft X-ray free-electron laser beam determined by ablation of organic molecular solids," *Optics Express*, 2007.

[73] E. D. Palik, *Handbook of Optical Constants of Solids*. Academic Press.

[74] S. Wilson, *A Study of Extreme Ultraviolet Capillary Discharge Lasers and the Ablation of Solid Targets*. PhD thesis, University of York, 2018.

[75] N. Stojanovic, D. V. D. Linde, K. Sokolowski-Tinten, U. Zastrau, F. Perner, E. Förster, R. Sobierajski, R. Nietubyc, M. Jurek, D. Klinger, J. Pelka, J. Krzywinski, L. Juha, J. Cihelka, A. Velyhan, S. Koptyaev, V. Hajkova, J. Chalupsky, J. Kuba, T. Tschentscher, S. Toleikis, S. Düsterer, and H. Redlin, "Ablation of solids using a femtosecond extreme ultraviolet free electron laser," *Applied Physics Letters*, vol. 89, p. 241909, 12 2006.

[76] P. E. Dyer, "Excimer laser polymer ablation: Twenty years on," *Applied Physics A: Materials Science and Processing*, vol. 77, no. 2, pp. 167–173, 2003.

[77] J. M. Liu, "Simple technique for measurements of pulsed Gaussian-beam spot sizes.," *Optics letters*, 1982.

[78] D. Nečas and P. Klapetek, "Gwyddion: An open-source software for SPM data analysis," 2012.

[79] T. Mocek, B. Rus, M. Stupka, M. Kozlová, A. R. Präg, J. Polan, M. Bittner, R. Sobierajski, and L. Juha, "Focusing a multimillijoule soft x-ray laser at 21 nm," *Applied Physics Letters*, 2006.

[80] M. Chaja, T. Kramer, and B. Neuenschwander, "Influence of laser spot size and shape on ablation efficiency using ultrashort pulse laser system," in *Procedia CIRP*, 2018.

[81] L. Torrisi, S. Gammino, L. Andò, V. Nassisi, D. Doria, and A. Pedone, "Comparison of nanosecond laser ablation at 1064 and 308 nm wavelength," *Applied Surface Science*, vol. 210, 2003.

[82] J. Chalupský, L. Juha, V. Hájková, J. Cihelka, L. VyšÍn, J. Gautier, J. Hajdu, S. P. Hau-Riege, M. Jurek, J. Krzywinski, R. A. London, E. Papalazarou, J. B. Pelka, G. Rey, S. Sebban, R. Sobierajski, N. Stojanovic, K. Tiedtke, S. Toleikis, T. Tschentscher, C. Valentin, H. Wabnitz, and P. Zeitoun, "Non-thermal desorption/ablation of molecular solids induced by ultra-short soft x-ray pulses," *Opt. Express*, vol. 17, pp. 208–217, Jan 2009.

[83] L. Juha, M. Bittner, D. Chvostová, J. Krása, M. Kozlová, M. Pfeifer, J. Polan, A. R. Präg, B. Rus, M. Stupka, J. Feldhaus, V. Létal, Z. Otcenasek, J. Krzywinski, R. Nietubyc, J. B. Pelka, A. Andrejczuk, R. Sobierajski, L. Ryc, F. P. Boody, H. Fiedorowicz, A. Bartnik, J. Mikolajczyk, R. Rakowski, P. Kubát, L. Pína, M. Horváth, M. E. Grisham, G. O. Vaschenko, C. S. Menoni, and J. J. Rocca, "Short-wavelength ablation of molecular solids: pulse duration and wavelength effects," *https://doi.org/10.1117/1.2037467*, vol. 4, p. 033007, 7 2005.

[84] J.-J. Rocca, M. Frati, B. Benware, M. Seminario, J. Filevich, M. Marconi, K. Kanizay, A. Ozols, I. Artiukov, A. Vinogradov, and Y. Uspenskii, "Capillary discharge tabletop soft x-ray lasers reach new wavelengths and applications," *Comptes Rendus de l'Académie des Sciences - Series IV - Physics*, vol. 1, no. 8, pp. 1065 – 1081, 2000.

[85] T. Green, I. Kuznetsov, D. Willingham, B. E. Naes, G. C. Eiden, Z. Zhu, W. Chao, J. J. Rocca, C. S. Menoni, and A. M. Duffin, "Characterization of extreme ultraviolet laser ablation mass spectrometry for actinide trace analysis and nanoscale isotopic imaging," *Journal of Analytical Atomic Spectrometry*, 2017.

[86] C. S. Menoni, I. Kuznetsov, T. Green, W. Chao, E. R. Bernstein, D. C. Crick, and J. J. Rocca, "Soft X-Ray Laser Ablation Mass Spectrometry for Chemical Composition Imaging in Three Dimensions (3D) at the Nanoscale," in *Springer Proceedings in Physics*, 2018.

[87] A. Kolomenski, A. Kolomenskii, J. Noel, S. Peng, and H. Schuessler, "Propagation length of surface plasmons in a metal film with roughness," *Applied Optics, Vol. 48, Issue 30, pp. 5683-5691*, vol. 48, pp. 5683–5691, oct 2009.

[88] B. L. Henke, E. M. Gullikson, and J. C. Davis, "X-ray interactions: photoabsorption, scattering, transmission and reflection e= 50-30,000 ev, z= 1-92," *Atomic data and nuclear data tables*, vol. 54, no. 2, 1993.

[89] K. R. Coombes, S. Tsavachidis, J. S. Morris, K. A. Baggerly, M. C. Hung, and H. M. Kuerer, "Improved peak detection and quantification of mass spectrometry data acquired from surface-enhanced laser desorption and ionization by denoising spectra with the undecimated discrete wavelet transform," *PROTEOMICS*, vol. 5, pp. 4107–4117, nov 2005.

[90] P. H. Eilers, "A perfect smoother," 2003.

[91] D. S. Whittaker, E. Wagenaars, and G. J. Tallents, "Temperatures following x-ray free-electron-laser heating of thin low- and medium- Z solid targets," *Physics of Plasmas*, 2011.

[92] I. Hutchinson, *Principles of Plasma Diagnostics*. Cambridge University Press, 2005.